Galactic Magnetic Fields and Cosmic Ray Anisotropies

Tesis Doctoral

Joaquín Castellano Simón

Departamento de Física Teórica y del Cosmos
Facultad de Ciencias
Universidad de Granada

Mayo 2015

Documento maquetado con TeXiS v.1.0+.

Galactic Magnetic Fields
and Cosmic Ray Anisotropies

Memoria presentada por
Joaquín Castellano Simón
para optar al título de
Doctor por la Universidad de Granada

Dirigida por los profesores
Manuel Masip Mellado
y
Eduardo Battaner López

Departamento de Física Teórica y del Cosmos
Facultad de Ciencias
Universidad de Granada

Mayo 2015

El doctorando Joaquín Castellano Simón y los directores de la tesis D. Manuel Masip Mellado y D. Eduardo Battaner López garantizamos, al firmar esta tesis doctoral, que el trabajo ha sido realizado por el doctorando bajo la dirección de los directores de la tesis y que, hasta donde nuestro conocimiento alcanza, en la realización del trabajo, se han respetado los derechos de otros autores a ser citados cuando se han utilizado sus resultados o publicaciones.

Granada, 22 de Abril de 2015.

Director/es de la Tesis

Fdo.: D.Manuel Masip Mellado

Fdo.: D. Eduardo Battaner López

Doctorando

Fdo. Joaquín Castellano Simón

Agradecimientos

La labor de escribir una tesis no es únicamente el resultado del trabajo personal de un estudiante, sino el fruto de la colaboración de muchas personas. En primer lugar la de los directores de la misma; Manuel y Eduardo, a quienes agradezco la oportunidad que me han brindado de poder compartir el apasionante mundo de la investigación y que se arriesgaron a comenzar la andadura de la tesis conmigo sabiendo que no iba a disponer de una dedicación exclusiva a la misma. A lo largo de estos años he compartido con ellos no solo conversaciones de ciencia sino de temas muy diversos, históricos y culturales especialmente, de los que he disfrutado enormemente y que me han permitido ver sus excelentes cualidades humanas, añadidas a las científicas que son sobradamente conocidas.

También quiero agradecer a mis compañeros de trabajo o de "mi colegio", que me han animado a continuar con la tesis cada día: Lidia, Poli, Raquel, Eli, Ricardo, Nuria, Elisa... junto con todos los demás que harían que la lista fuera demasiado larga para este pequeño texto. Quiero agradecer también a mis compañeros de la carrera: Juan Pablo, Luis, David, Aurora... que siempre han estado dispuestos a ayudarme y apoyarme especialmente con los programas de simulación. Por último a mi familia, que ha sido un gran pilar de apoyo, pues ha sabido entender los ratos dedicados a este proyecto que ha compartido como propio. Gracias.

Introduction

Since their discovery more than hundred years ago, cosmic rays have been a very interesting *puzzle* for particle physicists and astrophysicists. The addition of new pieces to this puzzle has often lead to important developments, like the discovery of antimatter or the muon. The field has experienced a sustained progress, and nowadays one may talk about a *standard model* of cosmic rays that is able to fit a remarkable amount of data. We can explain, for example, the ratio $R_{CR} \approx 0.25$ of light (Li, Be, B) to medium (C, N, O) nuclei observed in cosmic rays (in the solar system this ratio is $R_{SS} \approx 10^{-5}$) using a simple diffusive model of propagation through the interstellar medium. We can also understand their $\propto E^{-2.7}$ spectrum and the total energy density $\rho_{CR} \approx 1.5 \times 10^{-12}$ erg/cm^3 in the galaxy if cosmic rays are accelerated stochastically by the shock front in supernova remnants.

Despite this progress, some basic questions about the origin and the nature of the highest energy cosmic rays (up to 10^{11} GeV at Auger and possibly higher at JEM-EUSO) still remain. The collisions of these cosmic rays imply center of mass energies higher than the ones achieved at the LHC. Therefore, although particle colliders may have reached the highest energy available with the current technology, there is the possibility that ultrahigh energy cosmic rays and neutrinos reveal the existence of particles or interactions beyond those of the standard model. There is still a long way to go in astroparticle physics, but the solution to the observational puzzles that it faces may bring unexpected developments again.

With this in mind, the basic objective in this thesis has been to understand the origin of an $O(10^{-3})$ anisotropy observed in the cosmic ray flux at TeV–PeV energies (1 TeV $= 10^{12}$ eV, 1 PeV $= 10^{3}$ TeV). Cosmic rays that reach the Earth are almost completely isotropic, a fact that justifies a diffusive model of propagation. However, several cosmic ray observatories (Argo, Milagro, TIBET, IceCube, IceTop) have produced a high accuracy map of the sky that reveals anisotropies. There is an $O(10^{-3})$ deficit that peaks at 10 TeV and then evolves with the energy, together with other irregularities at smaller angular scales.

After a review of cosmic ray physics in Chapter 1, Chapter 2 describes in some detail the magnetic fields in our galaxy, as they play a major role to explain both their isotropy and (most likely) also the small anisotropy that we want to understand. In Chapter 3 we describe the *balistic* trajectories of cosmic rays in the presence of a regular magnetic field, since in our opinion the small-scale anisotropies are clearly a non-diffusive effect. We propose that a magnetic configuration that we name as *cosmic magnetic lens* could be the key ingredient that explains them.

In Chapter 4 we study the appearence of a global cosmic ray anisotropy. We try a new approach based on Boltzmann equation, which can be considered the *parent* of the usual diffusion equation that describes the propagation of cosmic rays. Whereas the second equation provides the number $n(E,\vec{x},t)$ of particles at $\vec{x}$ with energy E per unit volume and energy, the distribution function $f(\vec{p},\vec{x},t)$

in Boltzmann equation keeps also track of the momenta. To derive the diffusion equation one integrates the momenta, losing information (non-diffusive effects) that may be relevant to explain the cosmic ray anisotropies. Therefore, we explore what are the simplest solutions of Boltzmann equation consistent with cosmic ray anisotropies in the presence of a magnetic field with both regular and turbulent components.

Finally in Chapter 5 we study how our framework fits the data on the anisotropy in the different cosmic ray experiments. We argue that it provides an acceptable qualitative description of the anisotropies and a *prediction* that can be tested in future experiments. In particular, the observatory HAWC (in the northern hemisphere) could confirm that the large-scale cosmic ray anisotropy is modulated and changes sign above 100 TeV (energies that so far have only been accesible at the southern ICECUBE/ICETOP observatory).

The results described in this thesis have been published in 3 articles that are included in an appendix:

E. Battaner, J. Castellano and M. Masip,
Magnetic fields and cosmic ray anisotropies at TeV energies, Astrophysical Journal **799** (2015) 157;
Cosmic Magnetic Lenses, Astronomy and Astrophysics **527** (2011) 5;
Galactic magnetic fields and the large-scale anisotropy at MILAGRO, Astrophysical Journal Letters **703** (2009) L90.

Introducción

Desde su descubrimiento hace más de cien años, los rayos cósmicos han constituido un interesesante puzzle para los físicos de partículas y astrofísicos. La aparición de nuevas piezas de este puzzle ha llevado en muchas ocaciones a importantes avances, como el descubrimiento de la antimateria o del muón. El campo ha experimentado un gran progreso y hoy día se puede hablar de un modelo estándar de rayos cósmicos que es capaz de explicar una gran cantidad de datos.

Podemos, por ejemplo, explicar la ratio $R_{CR} = 0.25$ entre elementos ligeros (Li, Be, B) y elementos medianos (C, N, O) observado en los rayos cósmicos usando un modelo simple de propagación difusiva a través del medio interestelar. También somos capaces de entender el espectro (proporcional a la energía elevada a un exponente -2.7) y la densidad de energía de los mismos (1.5×10^{-5} erg/cm^3) si los rayos cósmicos son acelerados estocástimante por frentes de ondas expelidos por supernovas.

A pesar de este progreso, algunas cuestiones básicas acerca del origen y la naturaleza de los rayos cósmicos de más alta energía continuan abiertas. Las colisiones de estos rayos cósmicos implican una energía centro de masas más alta que la alcanzada en el LHC. Por tanto, aunque los aceleradores de partículas puedan haber alcanzado su máxima energía con la tecnología actual, existe la posibilidad de que el estudio de los rayos cósmicos y neutrinos de muy alta energía pueda revelar la existencia de partículas o interacciones más allá del modelo estándar. Hay todavía un largo camino por recorrer en física de astropartículas y la solución de algunos aspectos observacionales puede traer desarrollos inesperados una vez más.

Con esto presente, el principal objetivo de esta tesis ha sido entender el origen de una anisotropía de orden 0.1% observada en el flujo de los rayos cósmicos a energías en la franja del TeV-PeV. Los rayos cósmicos que alcanzan la Tierra lo hacen de manera casi isótropa, un hecho que justifica la ultilización de modelos difusivos de propagación. No obstante, algunos observatorios (ARGO, Milagro, TIBET, IceCube, IceTop) han producido mapas del cielo de gran precisión que revelan dicha anisotropía. Se trata de un déficit en direcciones cercanas al polo norte galáctico que alcanza un pico de intensidad a 10 TeV y que va cambiando con la energía. También se han observado irregularidades a escalas angulares menores.

Después de una revisión de la física de rayos cósmicos, en el capítulo 2 describimos someramente los campos magnéticos presentes en nuestra galaxia, ya que juegan un importante papel para explicar tanto la isotropía a gran escala así como las irregularidades de pequeña y mediana escala que queremos entender. En el capítulo 3, describimos las trayectorias balísticas de los rayos cósmicos en presencia de campos magnéticos regulares, puesto que, en nuestra opinión, las anistropías de pequeña y mediana escala son claramente un efecto no difusivo. Proponemos también que ciertas configuraciones del campo magnético que hemos denominado 'cosmic magnetic lenses' son un ingrediente clave para poder explicarlas.

En el capítulo 4 estudiamos la aparición de una anisotropía global en el flujo de rayos cósmicos. Exploramos un enfoque basado en la ecuación de Boltzmann, que puede ser considerada como la *madre* de la ecuación de difusión usual. Mientras que la segunda aporta información acerca del número de partículas $n(E, x, t)$ en una posición x

con energía E y por unidad de volumen, la función de distribución $f(p, x, t)$ presente en la ecuación de Boltzmann guarda información acerca de los momentos. Para obtener la ecuación de difusión se integran los momentos, perdiendose información (efectos no difusivos) que pueden ser relevantes para explicar las anistropías en el flujo de rayos cósmicos. Por tanto, buscamos las soluciones más sencillas de la ecuación de Boltzmann consistentes con la anisotropía en presencia de un campo magnético que incluye una componente regular y otra turbulenta.

Finalmente en el capítulo 5 analizamos cómo este modelo puede acomodar los datos disponibles y obtenemos una descripción cualitativa aceptable de las anistropías y una predicción que puede ser puesta a prueba en futuros experimentos. En particular, HAWC (un observatorio en el hemisferio norte) puede confirmar que la anistropía de gran escala está modulada y su signo cambia a energías por encima de los 100 TeV (hasta ahora sólo accesibles para los observatorios situados en el hemisferio sur.

Nuestros resultados han quedado recogidos en tres artículos publicados en revistas internacionales incluidos en el Apéndice:

Eduardo Battaner, Joaquín Castellano y Manuel Masip,
Magnetic fields and cosmic ray anisotropies at TeV energies, Astrophysical Journal **799** (2015) 157;
Cosmic Magnetic Lenses, Astronomy and Astrophysics **527** (2011) 5;
Galactic magnetic fields and the large-scale anisotropy at MILAGRO, Astrophysical Journal Letters **703** (2009) L90.

Contents

List of Figures

Chapter 1

Cosmic rays

In this Chapter we describe the basics of cosmic ray (CR) physics. CRs are charged particles that reach the Earth from outer space with energies between 1 and 10^{11} GeV. Due to the magnetic fields present in the interstellar and the intergalactic media, their arrival direction does not point back to their source. Therefore, only neutral particles (gamma rays or neutrinos) can in principle be used to indentify sources. Any form of cosmic radiation, however, may be used to learn about the astrophysical sources, about the medium where these particles have propagated in their way to the Earth, or about the fundamental laws of physics. In particular, they play nowadays an important role in dark matter or axion searches, and even as a probe for new interactions at very high energies. These particles are becoming an important tool that helps both astronomers and particle physicists to explore the Universe. Their efforts are now cordinated in a rapidly evolving field: astroparticle physics.

1.1 Introduction

The history of CRs started with the exploration of charged gases in closed vessels at the beginning of 20th century. Two Canadian groups (McLennan, 1903; Rutherford, 1903) noticed in 1903 that the leakage of electric charge from an electroscope within an air-tight chamber could be reduced by as much as 30% by enclosing it within a thick metal shield. They deduced that the loss of charge was due to some highly penetrating ray (of opposite charge) that was able to enter the chamber. This radiation was attributed to radioactive materials on the ground or the air.

The most penetrating radiation known at that time were the γ rays, with a well-known attenuation coefficient in air. When γ radiation goes through matter its intensity decreases exponentially. Therefore, such exponential dependence should be correlated with the ionization in the air. Within the following years, however, it was found that the amount of ionized matter does not decrease with the altitude as expected. The first report on that was made by Dutch physicist Theodor Wulf (Wulf, 1909), who measured in a lime-pit near Valkenburg and then at the top of the Eiffel Tower (the highest construction in the world at the time). Latter on Gockel took similar measurements higher above the ground in a balloon.

Victor Hess, working on radioactivity at the Physical Institute in Vienna, had speculated that the source of ionization may be in the sky rather than in the Earth's crust. In 1911-1913 he took ten balloon flights (five of them during the night, as the Sun could play a role) with pressure and thermal stable instruments. In his seventh flight he filled the balloon with hydrogen instead of coalgas and was able to ascend up to an altitude over 5 km (without an air mask!). The balloon started its flight on August 7th, 1912 from Usti nad Labem (Aussig) with himself and a crew of an aviator and a meteorologist, and it followed

Figure 1.1: Path of Hess's flight in the balloon "Bohmen" on August 7th, 1912.

the path shown in Fig. 1.1. Hess found that although the electroscope's rate of discharge decreased initially, above 610 m it increased, being four times larger at 4880 m than at sea level. He concluded that a highly penetrating radiation was entering the atmosphere from above (Hess, 1912), and that this radiation was still able to produce the ionization observed at much lower altitudes. After the flights made during the night and during an almost total eclipse, he also concluded that the Sun could not itself be the main source of the radiation.

Although his results were confirmed by W. Kolhrster, at that time Hess's hypothesis did not receive general acceptance, as other possibilities (like the lifting of radioactive sources from the ground into upper parts of the atmosphere) were still considered. Finally, in 1925 Millikan performed experiments submerging electroscopes in a lake at different depths, and he found that a depth in water equivalent to a given difference in atmospheric altitude gives the same readings (Millikan, 1926). This proved that the radiation must come from above and he named it "cosmic rays".

For many years there was the discussion whether CRs were neutral γ rays or charged particles. In particular, Millikan supported the idea that this radiation consists of high energy γ rays together with some secondary electrons from Compton scattering (i.e., electrons accelerated by collisions of the photons with air atoms). In 1929 the invention of the Geiger-Müller detector enabled the observation of individual CRs. Bothe and Kolhster built a *coincidence counter* by using two counters, one placed above the other (Bothe and Kolhorster, 1929). They found that simultaneous discharges of the two detectors occurred very frequently, even when a strong absorber (a gold tablet) was placed between them. The experiment strongly indicated that these particles were charged but very penetrating in matter, so they had to be very energetic. If charged particles constitute a majority of CRs, they will be deflected by the geomagnetic field and the flux will be strongest at the poles. In 1932 Compton presented a series of observations which showed a variation of the CR flux with the latitude (see Fig. 1.2).

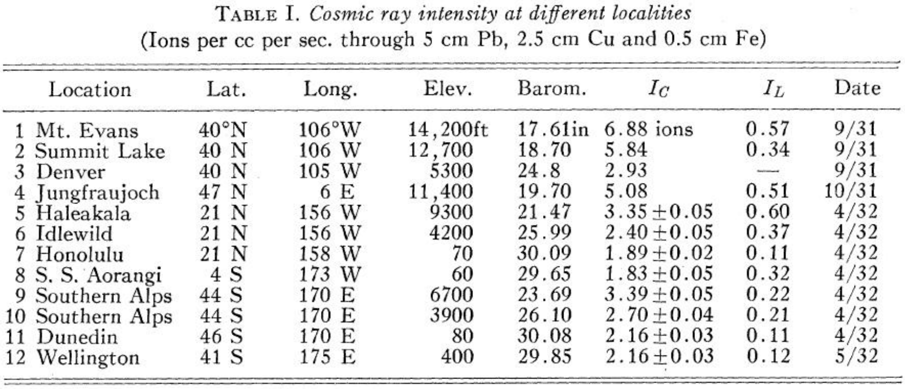

TABLE I. *Cosmic ray intensity at different localities*
(Ions per cc per sec. through 5 cm Pb, 2.5 cm Cu and 0.5 cm Fe)

Location	Lat.	Long.	Elev.	Barom.	I_C	I_L	Date
1 Mt. Evans	40°N	106°W	14,200ft	17.61in	6.88 ions	0.57	9/31
2 Summit Lake	40 N	106 W	12,700	18.70	5.84	0.34	9/31
3 Denver	40 N	105 W	5300	24.8	2.93	—	9/31
4 Jungfraujoch	47 N	6 E	11,400	19.70	5.08	0.51	10/31
5 Haleakala	21 N	156 W	9300	21.47	3.35 ± 0.05	0.60	4/32
6 Idlewild	21 N	156 W	4200	25.99	2.40 ± 0.05	0.37	4/32
7 Honolulu	21 N	158 W	70	30.09	1.89 ± 0.02	0.11	4/32
8 S. S. Aorangi	4 S	173 W	60	29.65	1.83 ± 0.05	0.32	4/32
9 Southern Alps	44 S	170 E	6700	23.69	3.39 ± 0.05	0.22	4/32
10 Southern Alps	44 S	170 E	3900	26.10	2.70 ± 0.04	0.21	4/32
11 Dunedin	46 S	170 E	80	30.08	2.16 ± 0.03	0.11	4/32
12 Wellington	41 S	175 E	400	29.85	2.16 ± 0.03	0.12	5/32

Figure 1.2: Latitude dependence of the cosmic ray intensity. Local radiation sources were shielded by copper and lead shells (Compton, 1932)

In 1934 Rossi reported the observation of near-simultaneous discharges in two Geiger-Muller counters widely separated in the horizontal plane during a measurement of the east-west effect. Three years later Pierre Auger and Maze, unaware of Rossi's earlier report, detected the same phenomenon and investigated it in more detail (Auger and Maze, 1938). Their experiments in the Alps revealed the existence of coincident CR events on very large scales (at more than 200 m of distance), meaning that they were actually associated with a single but *extensive* event. They presumed that this can happen when an extremely energetic particle interacts in the upper atmosphere with an air nucleus. Subsequent collisions of the created particles will produce a cascade, with a fraction of them hitting the ground. From electromagnetic cascade theory, Auger and colleagues estimated the energy of an incoming particle able to do that at more than 10^6 GeV, since the particle had to create about one million particles of 10^8 eV, plus a factor of ten for energy losses crossing the atmosphere (Auger, 1939).

A wide variety of experimental investigations demonstrated that the primary CRs striking the Earth's atmosphere are mostly charged particles. There were also some indirect confirmations, such as an explanation of the night aurorae phenomena observed in the polar zones (Stomer, 1930). The secondary radiation observed at ground level is composed primarily of a soft component of electrons and photons and a harder component of highly penetrating particles, muons, discovered by C.D. Anderson and his student S.H. Neddermeyer in 1936 (Anderson, 1936). Hess and Anderson shared the Nobel prize in physics in 1936 for the discovery of the cosmic radiation and the positron, respectively.

After these studies a common consensus about the nature of the CRs emerged. It was clear that they were relativistic atomic nuclei from outer space entering the Earth's atmosphere and generating cascades of secondary particles, known as air showers. The content in air showers proved to be very interesting for particle physicists, since they contained short-lived particles not easily found in the laboratory. It is very remarkable, in particular, that the investigation of CRs led to the discovery of antimatter. The first antiparticle, the positron, had been postulated by Paul Dirac in 1928, and it was discovered in 1932 by Anderson when cosmic radiation passing through a cloud chamber surrounded by a magnet collided with a lead plate creating an e^+e^- pair (Anderson, 1932). CR observations also stimulated widespread interest among astrophysicists, as they provided explanations for several phenomena observed in radioastronomy, like the emission of synchrotron radiation by astronomical objects. Fermi was able to estimate the galactic magnetic field strength from the isotropy of CRs just after World War II.

1.2 Composition

The energy spectrum of CRs extends from 1 GeV to energies above 10^{11} GeV (see Fig. 1.5). Below 100 GeV the flux of particles is sufficiently high so that detectors in satellite or balloon experiments, covering a typical area below 10 m^2, can see it. It is found that CRs may be any atomic nuclei, including the heavy ones. These nuclei are produced in collapsing stars, since primordial (Big Bang) nucleosynthesis may provide only the lightest ones (He, Li, B, Be). We observe (see Fig. 1.3) that the majority of CRs are protons (79%), helium (14%) and then all the nuclei of common elements (Longair, 2011). We also see, however, that the relative abundance of some species has some important differences with the abundance observed in the Solar System. In particular, there is an excess of the light nuclei Li, Be and B ($Z = 3, 4, 5$) relative to C, N and O ($Z = 6, 7, 8$). In stars light nuclei are consummed very efficiently in thermonuclear reactions that produce the heavier ones. Therefore, after the collapse of the star (when material for fusion is no longer available) one expects that their abundance is very low. The ratio of light to medium nuclei produced in stars should be similar to the ratio observed in the Solar System, $R_{SS} \approx 10^{-5}$, whereas in CRs we see $R_{CR} \approx 0.25$.

This difference is thought as the result of the fragmentation (or *spallation*) of the heavier nuclei during propagation, *i.e.,* the light nuclei are produced in collisions with the interstellar matter:

$$\mathcal{M} + p \to \mathcal{L} + X \,, \tag{1.1}$$

where $\mathcal{M}$ and $\mathcal{L}$ denote the medium and light nuclei, respectively. The average cross section for these collisions is $\sigma_{\mathcal{M}\mathcal{L}} \approx 78$ mb, and the total

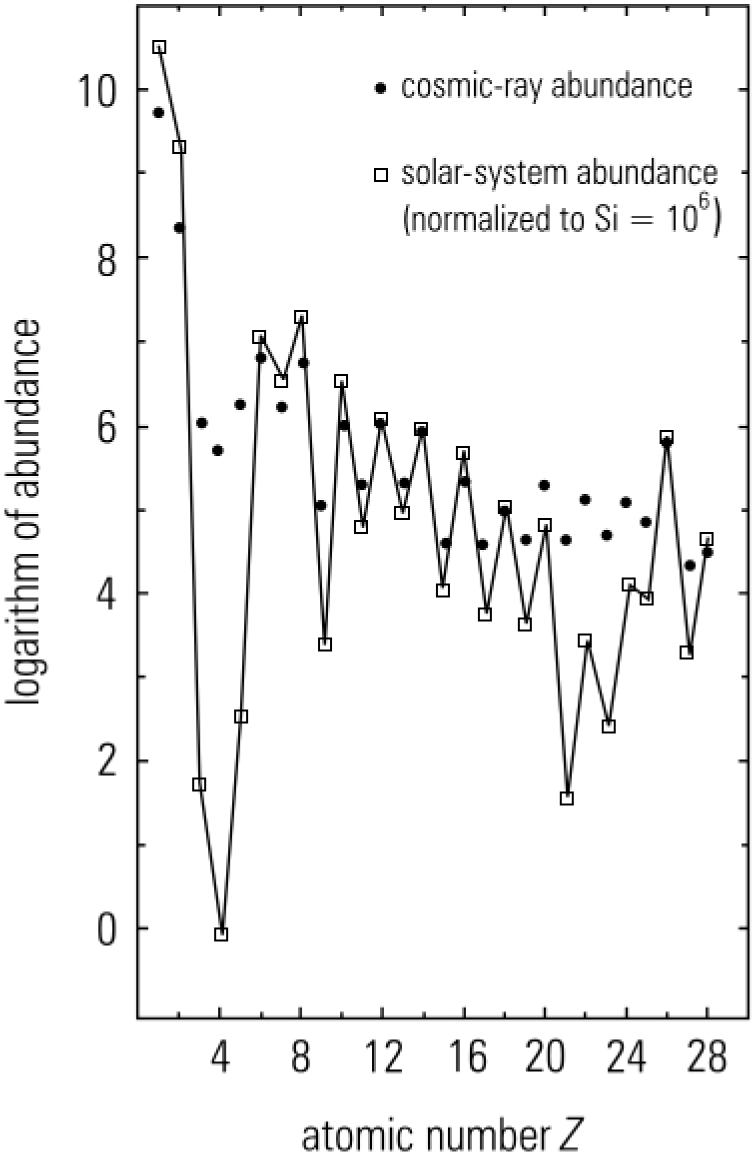

Figure 1.3: Nuclear abundance in CRs relative to the abundance observed in the Solar System (Michel et al., 1997)

$\mathcal{M}p$ cross section is $\sigma_{\mathcal{M}} \approx 280$ mb (Gaisser, 1990). This means that each collision of an $\mathcal{M}$ nucleus with an IS hydrogen atom will produce around $P_{\mathcal{M}\mathcal{L}} = 0.26$ light nuclei.

From the relative abundance that we observe we can deduce the average column density or *depth* X of matter that these nuclei cross before reaching us. X, given in g/cm^2 (or cm of water equivalent), is defined as

$$X = \int_{\ell_0}^{\ell_1} \mathrm{d}\ell \, \rho \, . \tag{1.2}$$

In our galactic disk, for an average (constant) density of 1 hydrogen atom per cm^3 the depth of a trajectory of length L is just $X = L \cdot \rho_{IS}$. The transport equation for the number density of both types of nuclei is then

$$\frac{dn_{\mathcal{M}}}{dX} = -\frac{n_{\mathcal{M}}}{\lambda^{\rm int}_{\mathcal{M}}}\, , \qquad \frac{dn_{\mathcal{L}}}{dX} = -\frac{n_{\mathcal{L}}}{\lambda^{\rm int}_{\mathcal{L}}} + P_{\mathcal{L}\mathcal{M}} \frac{n_{\mathcal{M}}}{\lambda^{\rm int}_{\mathcal{M}}}\, , \tag{1.3}$$

where the mean free path (or *interaction length*) $\lambda_i^{\rm int}$ is expressed in g/cm^2:

$$\lambda_i^{\rm int} = \frac{m_p}{\rho_{IS}\sigma_i} \times \rho_{IS} = \frac{m_p}{\sigma_i}\, . \tag{1.4}$$

For $\sigma_{\mathcal{M}} \approx 280$ mb and $\sigma_{\mathcal{L}} \approx 200$ mb we obtain $\lambda^{\rm int}_{\mathcal{M}} \approx 6.0$ g/cm^2 and $\lambda^{\rm int}_{\mathcal{L}} \approx 8.4$ g/cm^2. At the source $n_{\mathcal{M}}(0) = n_0$ and $n_{\mathcal{L}}(0) = 0$, which implies

$$n_{\mathcal{M}} = n_0 \, e^{-\frac{x}{\lambda^{\rm int}_{\mathcal{M}}}} \tag{1.5}$$

$$n_{\mathcal{L}} = n_0 \, P_{\mathcal{L}\mathcal{M}} \frac{\lambda^{\rm int}_{\mathcal{L}}}{\lambda^{\rm int}_{\mathcal{L}} - \lambda^{\rm int}_{\mathcal{M}}} \left(e^{-\frac{x}{\lambda^{\rm int}_{\mathcal{L}}}} - e^{-\frac{x}{\lambda^{\rm int}_{\mathcal{M}}}} \right) \tag{1.6}$$

In Fig.~1.4 we plot the ratio R_{CR} of light to medium atoms as a function of the depth. We obtain that $R_{CR} \approx 0.25$ at $X \approx 5$ g/cm^2. Dividing by ρ_{IS} we find that CRs have been travelling an average distance of 3×10^{24} cm $\approx$ 1 Mpc during a time $\tau_{\text{esc}} \approx 10^7$ years from their sources. This is much larger than the size of our galactic disk, 200-300 pc thick and with a radius of about 15 kpc. One concludes that CRs are *trapped* by the magnetic fields present in our galaxy, and that their trajectory must be similar to the random walk associated to a diffusion equation. This *hypothesis* is also supported by the almost perfect isotropy (at the one per mille level) that we observe in the CR flux.

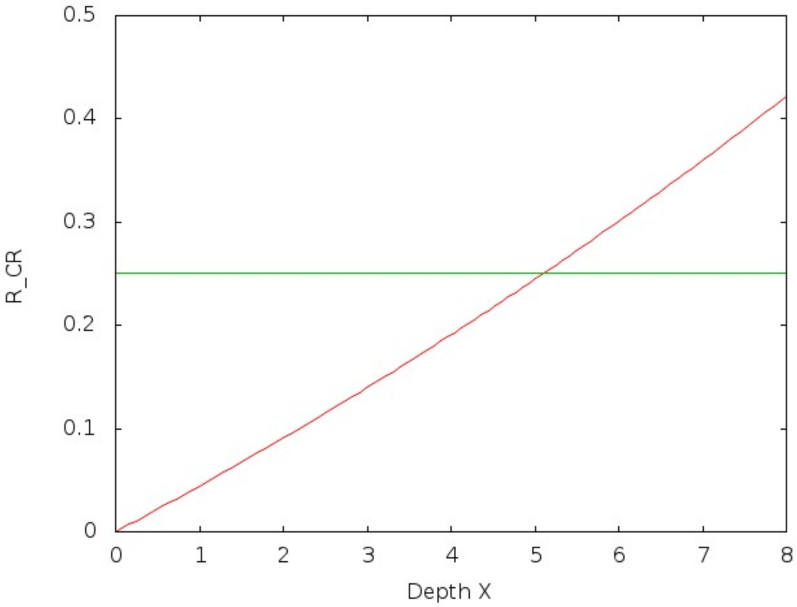

Figure 1.4: Ratio of light to medium nuclei in the CR flux as a function of the depth X in (g/cm^2) from the source.

The typical time that CRs spend in the galaxy before they *leak* out can be estimated as well using the relative abundance of radiactive isotopes observed in satellite experiments. In particular, the collisions of C, N an O with interstellar hydrogen produce both ^{10}Be and ^{7}Be in a proportion of $n_{10}/n_7 \approx 0.25$. The first one is radiactive, it decays into $^{10}\mathrm{B} + e\,\bar{\nu}$ with a lifetime $\tau_{10} \approx 2.2 \times 10^6$ yr, whereas the ^{7}Be is stable. Their ratio evolves then as:

$$\frac{n_{10}}{n_7}\, e^{-t/\tau_{10}} \,.$$

We observe $n_{10}/n_7 \approx 0.045$, implying a characteristic time of order $t \approx 4 \times 10^6$ yr. A more precise estimate by the satellite CRIS (Yanasak et al., 2001) using several isotopes concludes that $\tau_{\text{esc}} = 1.5 \times 10^7$ yr.

If magnetic fields are the main factor trapping TeV CRs, one expects that $\lambda_{\text{esc}} \approx c\, \rho_{IS}\, \tau_{\text{esc}}$ will depend on their *rigidity* R. R expresses the resistance of the particle to be deflected by a magnetic field:

$$R \equiv B\, r_L = \frac{p}{Ze} \approx \frac{E}{Ze\, c}\,, \tag{1.7}$$

where p is the momentum of the CR, Ze its charge, and the Larmor radius is $r_L = p/(Ze\, B)$. A fit of all the data provides a typical escape length:

$$\lambda_{\text{esc}} \approx (11.8\ \mathrm{g/cm^2}) \left(\frac{5\ \mathrm{GV/c}}{R} \right)^{0.6} \tag{1.8}$$

This implies that more energetic nuclei of smaller atomic number *escape* more efficiently from the galaxy. The energy dependence, in particular, is

$$\tau_{\text{esc}}(E) \approx \tau_{\text{esc}}(E_0) \, \left(\frac{E}{E_0} \right)^{0.6} \tag{1.9}$$

Let us also mention that CRs are mostly defined by particles, not antiparticles. Protons, antiprotons, electrons and positrons are observed at $E \approx 100$ GeV with a relative frequency $(p, \bar{p}, e^-, e^+) \approx (1, 10^{-4}, 10^{-2}, 10^{-4})$ (Adriani et al., 2010). Recently a small excess

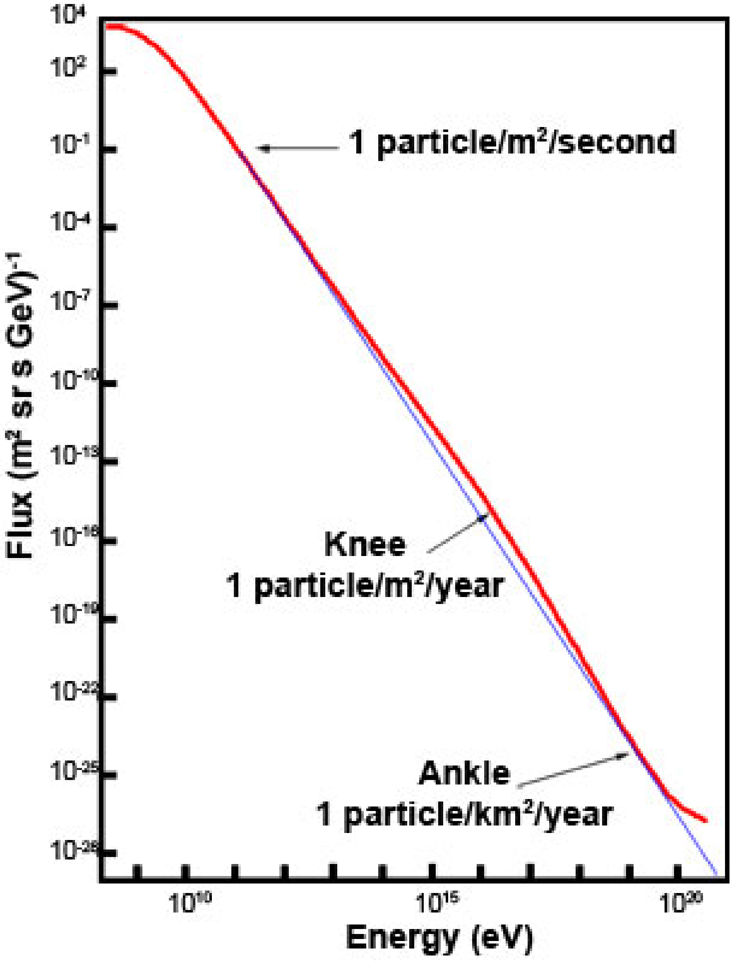

Figure 1.5: Spectrum of CRs from the combined data of different air shower measurements. It exhibits a 'knee' and an 'ankle' that deviate from the standard exponential decline (blue line) (Hillas, 2006).

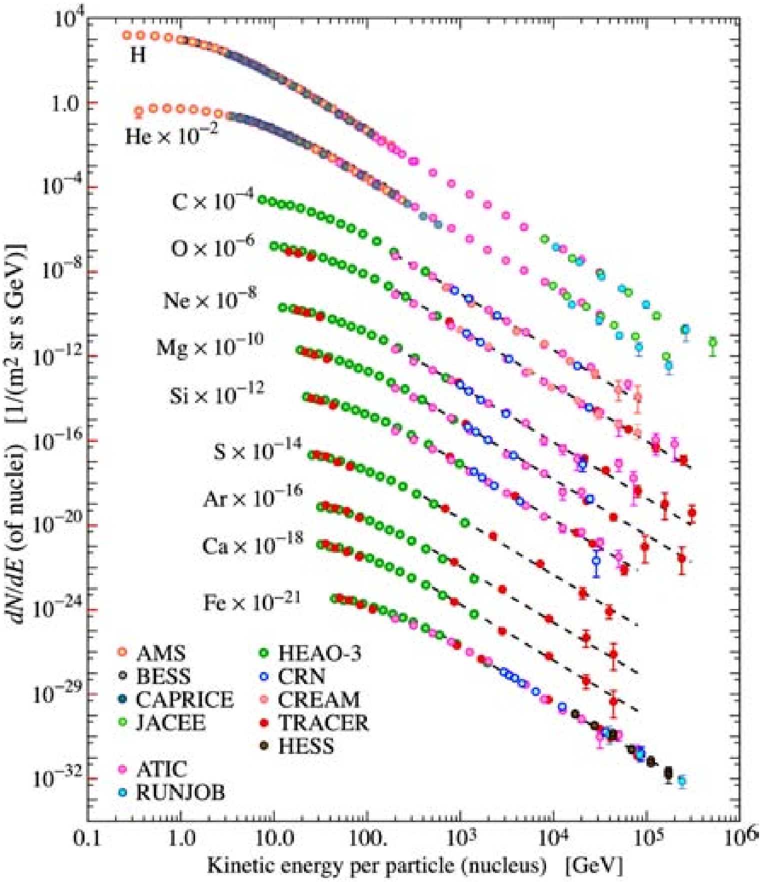

Figure 1.6: Spectra of the major components of the CRs for energies up to 10^6 GeV. The individual graphs are scaled by the factor noted in the plot (Nakamura, 2010).

(not derived from spallation nor astrophysical objects like quasars) of antimatter has been detected by several satellite experiments: AMS, Pamela and Fermi (Coutu, 2013). In Fig. 1.7 we show the positron excess. The origin of these positrons could be astrophysical (pulsars), but it has been speculated that it could be a sign of anihilation of dark matter. For a review of dark matter, see (Munoz, 2004).

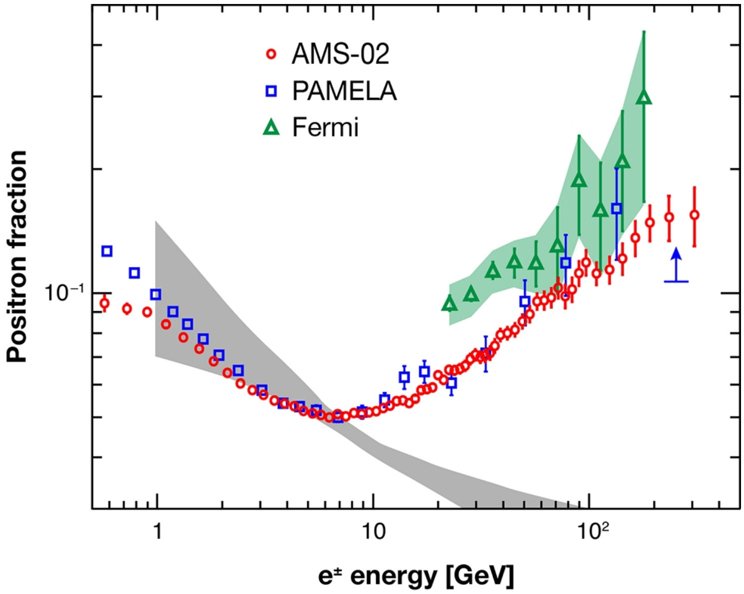

Figure 1.7: Positron fraction in high-energy CRs (Aguilar et al., 2013).

There are also two neutral components in the flux of cosmic particles: neutrinos and gamma rays. Although in this thesis we will not discuss these *messengers*, we would like to mention that they may provide a picture of the sky that could be quite *different* from the usual one (obtained with light at different frequencies). Gamma ray astronomy is nowadays a very active field that is providing very interesting results, with the discovery of gamma ray in a number of new astrophysical objects (pulsars, active galactic nuclei, star flares, etc). Solar neutrino experiments have been essential to establish that these particles have a mass. Moreover, the recent observation by IceCube of a non-atmospheric flux at 100-1000 TeV energies opens the possibility of neutrino astronomy.

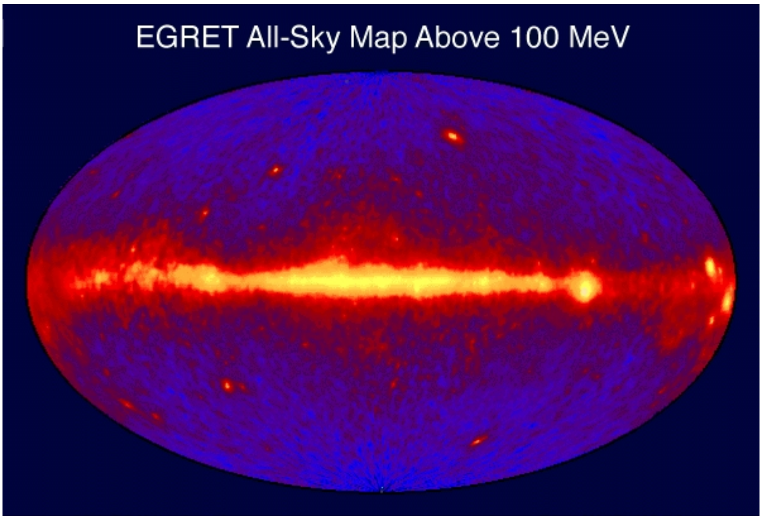

Figure 1.8: Image of the entire sky in gamma rays of energy above 100 MeV as seen by EGRET. Bright spots within the galactic plane are pulsars while those above and below the plane are thought to be quasars (Sreekumar et al., 1998).

1.3 Sources and Spectrum

At kinetic energies below 1 GeV the CR spectrum varies strongly with the phase of the solar cycle. In particular, it is observed that the flux

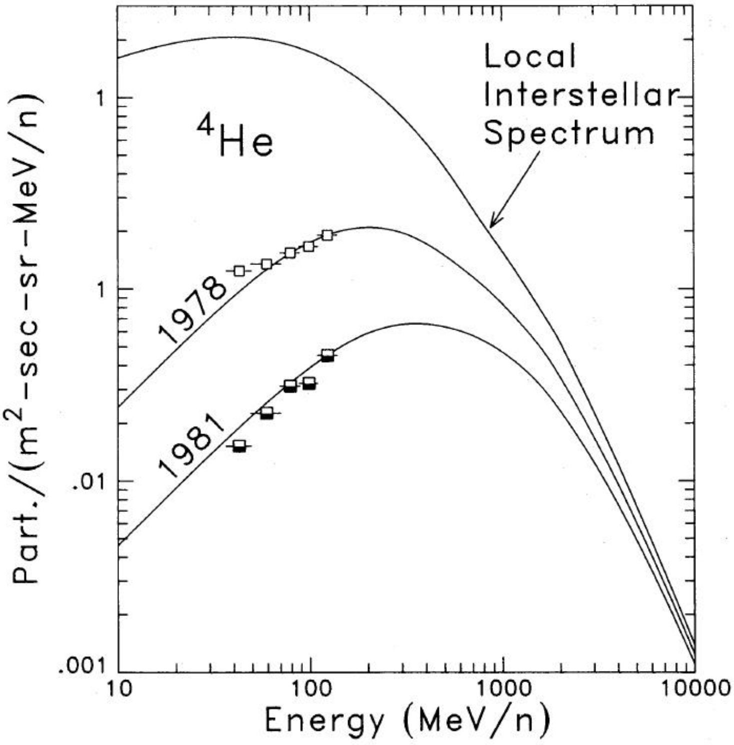

Figure 1.9: Calculated local interstellar ^{4}He spectrum and spectra in 1978 and 1981 (periods of minimum and maximum solar activity) (Kroeger, 1986).

decreases during the periods of high solar activity. This solar modulation is due to the outflowing solar wind, which deflects a fraction of the CR flux and prevents it from reaching the Earth (see Fig. 1.9). Up to 10 GeV, however, the composition of the CR flux coincides with the solar one, which implies that these particles are predominantly produced by the Sun.

At higher energies the CR spectrum is nearly featureless, it can be described in terms of a simple power-law of type $E^{-\alpha}$. This indicates that CRs originate outside the Solar System. At very high energies the overall spectrum shows two distinct features: a steepening of the spectral index from $\alpha = 2.7$ to $\alpha = 3$ at 3×10^6 GeV, and a flattening above 10^9 GeV (Adriani et al., 2011). These features, known as the knee and the ankle in analogy with the shape of a human leg, describe the flux up to energies $E \approx 10^{10.5}$ GeV. There the presence of a GZK suppression is still not fully established (Takeda et al., 1998).

The reason for these changes in the spectral index is under debate, but it is thought that up to the knee the flux would be dominated by particles accelerated by supernova remnants (see below) inside our own galaxy. Between the knee and the ankle the dominant component in the CR flux would also be of galactic origin, but not supernova remnants. Above the ankle magnetic fields are not efficient to trap CRs, and their origin should be predominantly extragalactic.

The energy of a CR can be used to estimate the size and and the magnetic field B in the region where it has been accelerated. The basic idea, proposed in (Hillas, 2005), is that when the Larmor radius of a charged particle, $r_L = \frac{E}{QB}$, is larger than the region of coherence of B, the particle will leave the source. This imposes a limit on the maximum energy that a cosmic accelerator of size R can provide:

$$E_{max} = QBR\,. \tag{1.10}$$

This general geometrical argument known as the Hillas criterion is useful for selecting potential acceleration sites. Fig. 1.9 shows the minimum B and size of a source able to accelerate protons up to 10^{12} GeV and iron up to 10^{11} GeV. A realistic description of particle acceleration must also take into account the energy lost during the process. In particular, notice that the energy that a particle can achieve also reaches a maximum if the rate of energy lost becomes equal to the rate of energy gained.

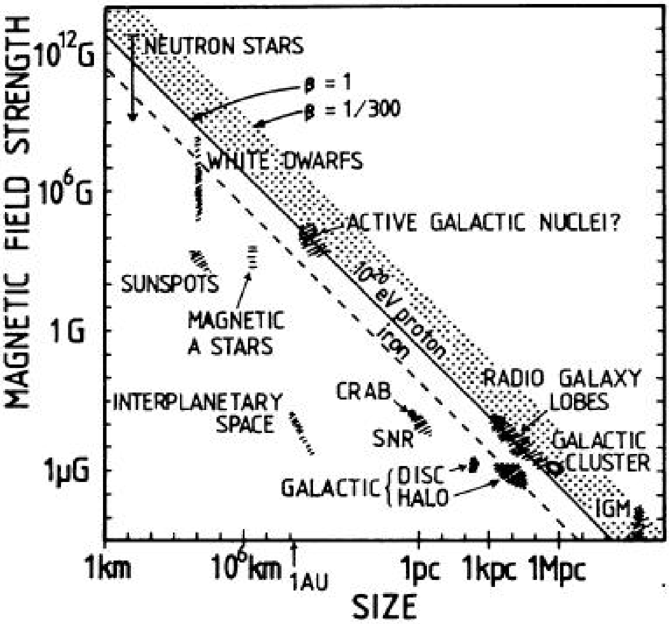

Figure 1.10: The size and magnetic field strength of different candidates for CR acceleration. The (dotted) solid line limits candidates that could accelerate protons (iron) up to 10^{11} GeV (Hillas, 2005).

An analogous argument can be applied to the question of whether

CRs originate inside our galaxy or have an extragalactic origin. The magnetic field in our galaxy is in the order of several μG (Stanev, 1997; Zatsepin and Kuzmin, 1966). For energies higher than $\approx 10^9$ GeV the r_L of protons exceeds the thickness of the galactic disc. If they were galactic their arrival direction would be in the plane, introducing an excess that has not been observed. Therefore, CRs of energy above 10^9 GeV would be predominantly extragalactic, whereas at lower energies the dominant component in the CR flux could have been accelerated at galactic supernova remnants (Fermi, 1949; Ptuskin et al., 2010). An important reason why we think that remanants provide the key astrophysical acceleration process is the following estimate.

Our galactic disk has a volume $V \approx 10^{67}$ cm^3. We observe a CR energy density of $\rho_{CR} \approx 0.5$ eV/cm^3 (Stanev, 2010); let us suppose that this coincides with the average density in the whole disk. Since CRs are trapped an average time of $\tau_{\text{esc}} \approx 10^7$ y, the power required to replace the CRs that leak out is $V\rho/\tau_{\text{esc}} \approx 3 \times 10^{40}$ erg/s. In our galaxy there are around 3 supernova explosions per century, and each remnant contains a mass of $10M_\odot$ with a speed of 5×10^8 cm/s. Since this gives a total kinetic energy of $3{\times}10^{51}$ erg per year, a 0.1% efficiency would be enough to keep the CR energy density at the observed value.

Let us briefly review the standard scenarios for CR acceleration. The idea is that the acceleration is a stochastic process with a basic cycle where the CR (in average) will gain a small fraction of energy. By repeating this process many times extremely large energies can be reached. Let us assume that the average fraction of energy gained per cycle does not depend on the energy,

$$\frac{\Delta E}{E} = \alpha. \tag{1.11}$$

Let us also assume that in each cycle there is an energy independent probability $P_{\text{esc}} = \epsilon$ that the particle escapes and does not enter the next cycle. Under the assumption than α is small, after k acceleration cycles the number of remaining particles is

$$N = N_0(1-\epsilon)^k. \tag{1.12}$$

These particles will end up with an energy above

$$E = E_0(1+\alpha)^k. \tag{1.13}$$

From these expressions it follows that N and E are related by

$$N = N_0 \left(\frac{E}{E_0}\right)^{\frac{\ln(1-\epsilon)}{\ln(1+\alpha)}} . \tag{1.14}$$

If we derive we obtain that this framework, known as the Fermi mechanism, can explain a power-law for the flux of particles:

$$\frac{dN}{dE} \propto \left(\frac{E}{E_0}\right)^{\frac{\ln(1-\epsilon)}{\ln(1+\alpha)}-1} . \tag{1.15}$$

To ilustrate how the kinetic energy of a magnetized plasma can be transferred to individual CRs we will first consider the *original* (2nd order) Fermi scenario. Suppose that a relativistic particle ($E_1 \gg mc^2$) enters a gas cloud moving with velocity $v \ll c$ in direction opposite to the particle. In the frame of the cloud the particle has an energy

$$E_1' = \gamma(E_1 + vp_1) \approx \gamma E_1(1+\beta)\,, \tag{1.16}$$

since $p_1 \approx E_1/c$. Inside the cloud the particle will interact elastically several times with the turbulent magnetic field and will change its direction, *i.e.*, its energy will be $E_2' = E_1'$ but its momentum will take a random direction. Let us first assume that the particle exits the cloud just opposity to the direction of entry. In that case when we go back to the lab frame its energy is

$$E_2 = \gamma(E_2' + vp_2') \approx \gamma E_2'(1+\beta) \approx \gamma^2(1+\beta)^2 E_1 = \frac{1+\beta}{1-\beta}E_1\,. \tag{1.17}$$

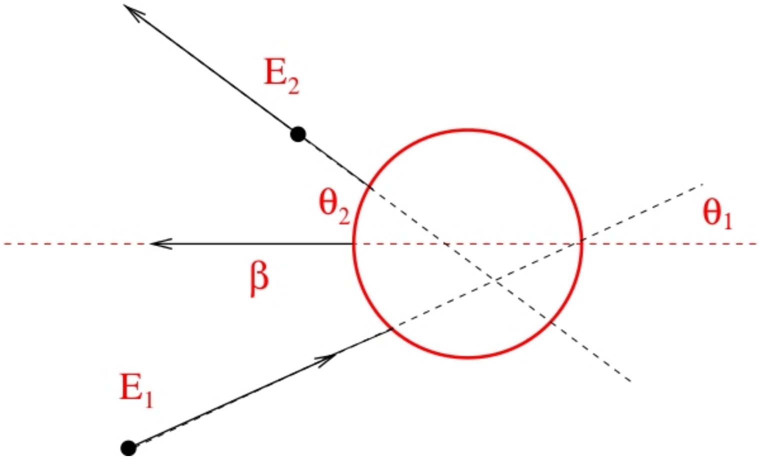

Figure 1.11: Acceleration cycle of a CR by a gas cloud.

We see that the particle has increased its energy by a factor of $(1+\beta)/(1-\beta)$. Notice, however, that if the direction of exit would have coincided with the one of entry (not its opposite) then the particle would have not gained energy, and that if the particle were initially moving in the same direction as the cloud (not opposite) it could have lost energy in the process. The generic case with an angle θ_1 of entry and an angle θ_2 of exit is depicted in Fig. 1.11. The energy of the particle when it exits the cloud is

$$\frac{E_2 - E_1}{E_1} = \frac{\Delta E}{E_1} = \frac{\beta\ \cos\theta_1 + \beta\ \cos\theta_2' + \beta^2\,(1+\cos\theta_1\cos\theta_2')}{1-\beta^2}\ . \tag{1.18}$$

Since $\cos\theta_2'$ may take any value between -1 and +1 with the same probability ($\langle\cos\theta_2'\rangle = 0$) we obtain that the average gain of energy is

$$\langle\frac{\Delta E}{E_1}\rangle = \frac{\beta\ \cos\theta_1 + \beta^2}{1-\beta^2} \tag{1.19}$$

The average value of $\cos\theta_1$, however, is not that simple: if the clouds are isotropically distributed, the particle will find more of them in opposite than in the same directions (just like in the highway you cross with more cars coming from the opposite lane). It is easy to see that the number of clouds is proportional to $(1 + \beta\, cos\theta_1)$. Therefore

$$\langle\cos\theta_1\rangle = \frac{\int_{-1}^{1} d(\cos\theta_1)(1+\beta\cos\theta_1)\cos\theta_1}{\int_{-1}^{1} d(\cos\theta_1)(1+\beta\cos\theta_1)} = \frac{\beta}{3} \tag{1.20}$$

and

$$\langle\frac{\Delta E}{E_1}\rangle \approx \frac{4}{3}\beta^2\,. \tag{1.21}$$

Although in principle this mechanism could work, it is not very efficient: the gain is proportional to $\beta^2 \approx 10^{-6}$. Shock fronts in supernova remnants, however, provide a much more effective scenario (1st order Fermi mechanism). The supernova explosion creates a shockwave travelling at a constant hypersonic velocity ($v_s \approx 0.01c$) during a long time (1000 years). The pass of the front disturbs the gas *downstream*, which will pick up some velocity v, in particular, for a monoatomic gas one estimates that $v \approx (3/4)v_S$ (see Fig. 1.12).

An acceleration cycle will consist of a relativistic CR with energy E_1 crossing the front from upstream to downstream, then interacting with the random magnetic fields there, and finally going back upstream. The crucial difference with the acceleration by plasma clouds is that in the entry region the CR always finds $\cos\theta_1 > 0$ (otherwise it will not cross the front), whereas to return upstream it needs $\cos\theta'_2 > 0$. As a result, in this cycle the CR always gains energy, which is provided by the plasma behind the front. It is easy to see that the frequency of upstream CRs crossing the shock front is proportional to $\cos\theta_1$ with $0 \le \cos\theta_1 \le 1$, and also that the frequency of those crossing in the oposite direction goes approximately like $\cos\theta'_2$ (for positive

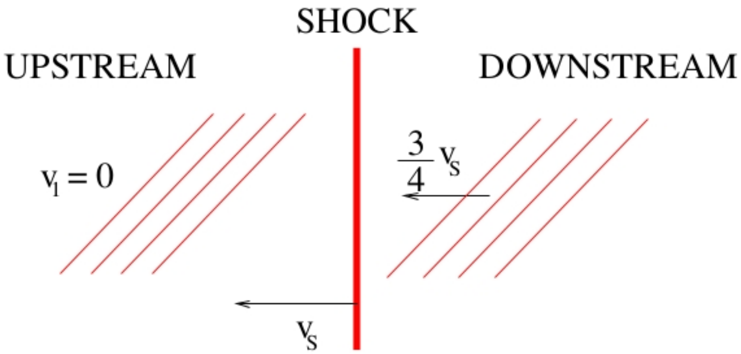

Figure 1.12: Representacion of a CR crossing a shockwave during the 1st order Fermi acceleration mechanism.

values of this cosine). As a result

$$\langle \cos\theta_1 \rangle = \langle \cos\theta_2' \rangle = \frac{\int_0^1 d(\cos\theta_2') \cos\theta_2' \cdot \cos\theta_2'}{\int_0^1 d(\cos\theta_2')} = \frac{2}{3} \tag{1.22}$$

For the average energy gain one obtains

$$\langle \frac{\Delta E}{E_1} \rangle = \frac{\frac{4}{3}\beta + \beta^2 \left(1 + \frac{4}{9}\right)}{1 - \beta^2} \approx \frac{4}{3}\,\beta =\approx \frac{v_S}{c}\,. \tag{1.23}$$

We can also estimate the probability that a CR escapes, *i.e.*, after crossing the front does not go back upstream. Suppose that the CR number density is n_{CR}. If the front were static then the number of CRs upstream and downstream would be constant. This implies that if a CR crosses in one direction another one must cross in the opposite direction, and sooner or later all CRs will complete the cycle. The movement of the front, however, changes the balance. In the rest frame of the downstream gas the shock front advances upstream at $\approx (1/4)v_S$. In this frame the number of CRs that cross upstream to downstram per unit time and area is proportional to $\rho_{CR} \cdot c \cdot 1/2 \cdot 1/2$, with the first 1/2 factor indicating that only those moving towards the front will cross it and the second one giving the average value of $\cos\theta_1'$, whereas the number of CRs gained by the downstream region will go like $\rho_{CR} \cdot (1/4) v_S$. Therefore, the probability that one CR escapes is

$$P_{\text{esc}} = \frac{\rho_{CR}\,(1/4) v_S}{\rho_{CR}\, c\,(1/2)\,(1/2)} \approx \frac{v_S}{c}\,. \tag{1.24}$$

In this framework we obtain

$$\langle \frac{\Delta E}{E_1} \rangle \equiv \alpha \approx \frac{v_S}{c}\,, \qquad P_{\text{esc}} \equiv \beta \approx \frac{v_S}{c}\,. \tag{1.25}$$

The spectral index that this implies is in the CR flux would be

$$\frac{\ln(1-\beta)}{\ln(1+\alpha)} - 1 \approx -\frac{\beta}{\alpha} - 1 \approx -2 \tag{1.26}$$

We then have a universal power law for the spectrum with a spectral index that is independent of the shock velocity: no matter how fast or slow, it gives the same spectrum. If we add that more energetic CRs escape more efficiently by a factor of $(E/E_0)^{0.6}$ (see Eq. 1.9) we obtain

$$\frac{dN}{dE} \propto \left(\frac{E}{E_0}\right)^{-2-0.6}\,, \tag{1.27}$$

which is very close to the observed –2.7 value.

This process, however, will eventually become ineffective due to several reasons. First, as the energy increases the CR will increase its Larmor radius and the supernova remnant will be unable to confine it. Second, at large energies protons may interact with the thermal photons produced at the (very hot) shock front and will produce pions:

$$p\gamma \to \triangle^+ \to p\,\pi^0\,,\; n\,\pi^+ \tag{1.28}$$

In addition, electrons will emit an amount of synchrotron radiation similar to the energy that they gain per cycle. This radiation is of course a good way to search for acceleration sites. A galactic supernova remnant is shown in Fig. 1.13

Figure 1.13: The crab nebula supernova remnant (Slane et al., 2000).

At energies above 10^6–10^8 GeV active galactic nuclei (AGNs) are believed to be the dominant source of CRs. AGNs are the core regions of galaxies, and they feature a much higher than usual luminosity. A supermassive black hole in the center of a galaxy can build accretion disks of hot, ionized plasma, generating very strong magnetic fields. These fields could accelerate CRs to the highest energies observed in the CR spectrum. Additionally, some AGNs feature jets of highly relativistic magnetized matter that could as well accelerate CRs (Rieger et al., 2007) up to energies around 10^9 GeV. Also there is an special acceleration pattern during galaxy-galaxy collisions (Lisenfeld and Voelk, 2010) by shockwaves which results in a higher synchroton emision by electrons and nuclei.

Chapter 2

Galactic magnetic fields

Magnetic fields are ubiquitous in the universe: they are present in planets, stars, galaxies, clusters of galaxies and in the inter-cluster regions. The possibility to find cosmological magnetic fields is currently investigated by several experiments (Strassmeier et al., 2009). In particular, PLANCK has established an upper limit of about 5 μG for a comoving magnetic field at the time of recombination (PLANCK, 2014). The effects of cosmic magnetic fields are diverse. They align the spinning micron-sized dust particles in the interstellar medium, they accelerate and deflect cosmic rays, and they reduce the angular momentum during the gravitational collapse of matter into stars. Magnetic fields could also provide the force that generates galactic warps (Ruiz-Granados et al., 2012) and even play a non-negligible role in the flattening of the rotation curves of galaxies (Battaner et al., 1992). There are many proccesses in which magentic fields play a non-negligible role. In the near future experiments like SKA and LOFAR will provide more detailed information about cosmic magnetic fields. QUIJOTE in Tenerife is a project which at present is providing excellent new data (Rubiño-Martin et al., 2012). As we will see in latter chapters, galactic magnetic fields could also be the origin of the anisotropy detected by several CR observatories at TeV energies.

In the Milky Way, typical field strengths are of order μG, but in filaments in the galactic center they could be up to three orders of magnitude larger. While the galactic magnetic field exhibits a regular large-scale structure, random fields at smaller scales are comparable in strength. The average energy density of the galactic magnetic field is $\rho_B = B^2/(8\pi) \approx 1$ eV/cm^3, which is similar to the energy density ρ_{CR} in CRs and also to the kinetic energy density due to the turbulent motion of particles in the galaxy. This indicates that galactic magnetic fields have a non-negligible effect on processes occurring throughout the interstellar medium, such as star formation, energy transport or CR propagation.

The study of the galactic magnetism started with the discovery of the polarization of starlight by Hiltner (Hiltner, 1949). The phenomenon was presumed to be caused by magnetic fields permeating the interstellar space, and it was given a plausible explanation by Davis and Greenstein (Davis and Greenstein, 1951) in terms of magnetically aligned dust grains. After the discovery of synchrotron radiation (Schwinger, 1949) and the development of radio astronomy in the early 1950s, several non-thermal radio emitting sources were argued to consist of energetic electrons spiraling in magnetic fields (Alfvén and Herlofson, 1950).

These were indirect observations of interstellar magnetic fields. Bolton and Wild (Bolton and Wild, 1957) suggested that they could be studied directly by the Zeeman effect (transitions between atomic energy levels in presence of a magnetic field). Due to technical challenges, the discovery of the Zeeman splitting in interstellar gas of neutral hydrogen did not take place until a decade later (Davies and Wilson, 1968). Wielebinsky discovered the polarized synchroton radiation in 1962. A bit later, the first measurements of the galactic magnetic field using Faraday rotation of the polarized radio emission from pulsars were made by (Lyne and Smith, 1968). Faraday rotation applied to polarized extragalactic radio sources led Davies (Lyne and Rickett, 1968) to conclude that a large-scale, regular magnetic field permeated the Milky Way. In this chapter we describe in some detail the most common techniques to measure the galactic magnetic field and then discuss its large-scale structure and its irregularities.

2.1 Detection techniques

2.1.1 Faraday rotation

Faraday discovered that when a polarized light beam crosses an intense magnetic field $\vec{B}$ the polarization vectors changes. A circularly polarized electromagnetic wave incident on a free electron in the interstellar medium induces a circular motion of the electron (Harwit, 2006; Rybicki and Lightman, 1986), that will be either clockwise or counter-clockwise. The movement will, in turn, create a magnetic field that will add or substract to the component $B_{\|}$ of $\vec{B}$ along the direction of propagation, causing a phase difference between the left- and right-handed polarized beams. This effect can be understood as a different refractive index seen by the two circularly polarized modes. Since the linearly polarized light is a superposition of both circular polarizations, the net effect will be a shift in the polarization angle:

$$\Delta\theta \approx \frac{e^3\lambda_2}{2\pi m^2 c^4}\int_0^2 nB_{\|}ds \equiv RM\,\lambda^2, \tag{2.1}$$

where n is the number density of electrons at each point along the path and

$$RM = 8\cdot 10^5 \int_0^L \left(\frac{n}{\mathrm{cm}^{-3}}\right)\left(\frac{B_{\|}}{\mathrm{T}}\right)\left(\frac{dL}{\mathrm{pc}}\right) \tag{2.2}$$

is the so called rotation measure.

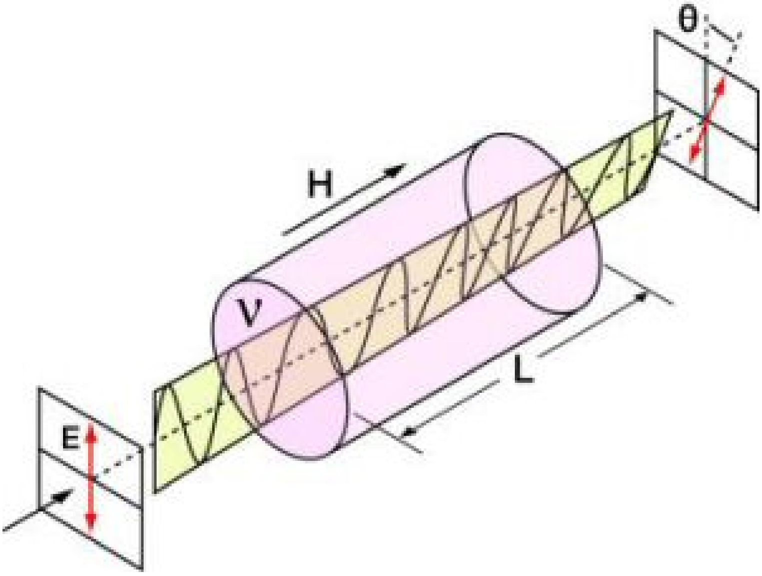

Figure 2.1: Scheme of Faraday rotation mechanism, where E denotes the electric field and H the magnetic field.

In the case of radio pulsars, the dispersion caused by the IS electrons results in a time delay between pulses received at different wavelengths, a phenomenon that is called dispersion measure. This is quantified in terms of the electron column density. A measurement of both the dispersion measure and the rotation measure gives therefore the weighted mean of the magnetic field along the line of sight. The same information can be obtained from objects other than pulsars, but it requieres an estimate of the propagation path length and the typical electron densities. In particular, Faraday rotation measurements of polarized radio signals from extragalactic radio sources occulted by the solar corona have been used to estimate both the electron density distribution and the direction and strength of the magnetic field in the coronal plasma (Mancuso and Spangler, 2000).

2.1.2 Synchrotron emission

Relativistic electrons spiralling along magnetic field lines emit synchrotron radiation. For a power law distribution of relativistic electrons, commonly called CR electrons, the electron density n_{cre} is characterized by a spectral index s,

$$n_{cre}(E)E \propto n_{cre,0}E^{-s}E\,. \tag{2.3}$$

The synchrotron emissivity is then

$$j_v \propto n_{cre,0}B^{\frac{1+s}{2}}\nu^{\frac{1-s}{2}}\,. \tag{2.4}$$

For a regular magnetic field and the above relativistic electron distribution, the emitted synchrotron radiation has a large degree of linear polarization, around 75% for a spectral index $s = 3$. Observationally, the percentage of polarization is typically much lower than this due to depolarizing effects such as Faraday depolarization by turbulent magnetic fields through line-of-sight.

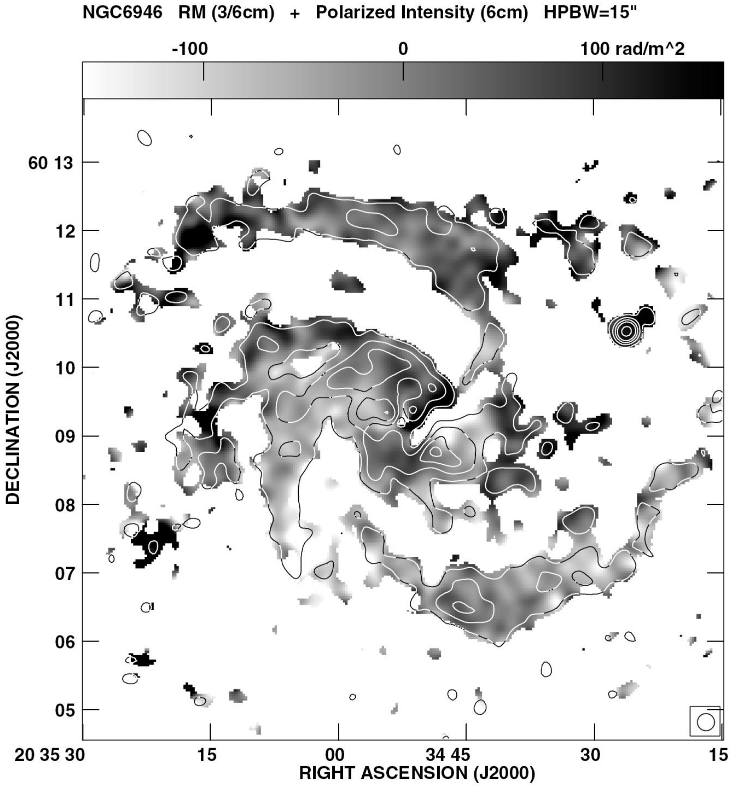

Figure 2.2: Observed RM distribution across the this equation over the total path length spiral galaxy NGC 6946 (Beck, 2007).

A widely used (and debated, see (Beck and Krause, 2005)) assumption about the interstellar medium in the Milky Way and other galaxies is the energy equipartition between magnetic fields and CRs, *i.e.*, the equality between the magnetic and CR energy densities, $\rho_B \approx \rho_{CR}$. It indicates that both components are coupled and able to exchange energy. This useful assumption enables the calculation of magnetic field strengths in other galaxies, interstellar clouds, or any other astrophysical object based on the observable synchrotron (radio) emission.

2.1.3 Starlight polarization

It is observed that optical light from different stars in the same vicinity has similar polarization. Davis and Greenstein (1951) concluded that the IS medium, and not the stars themselves, is the cause of this effect. They argued that the polarization is caused by the alignment of spinning, non-spherical grains through the mechanism of paramagnetic relaxation. The long axis of the grains align perpendicular to the ambient magnetic field, light that is polarized in the direction of the grain's long axis is preferentially absorbed, and it results in a net polarization of the unabsorbed light parallel to the magnetic field. However, since the discovery of the Davis-Greenstein effect, other processes that affect the alignment of interstellar grains have also been described (Draine, 2003).

There are drawbacks in the use of starlight polarization to study the large scale magnetic field. First, since individual stars must be observed, only the nearby (3 kpc) part of the Galaxy can be probed. Second, it is a self-obscuring effect based on the extinction of light, and about 3% polarization corresponds to one visual magnitude of extinction. For these reasons starlight polarization is best used as a probe of small scale magnetic structures, such as interstellar clouds, and not for the large scale galatic magnetic field.

Currently, about 104 measurements of starlight polarization exist. This number is growing quickly through the use of automated surveys (Clemens and Bressan, 2009) and is approaching 10^6 within a year.

2.1.4 Zeeman effect

An electron orbiting a nucleus with angular momentum $\vec{L}$ acquires a magnetic moment $\vec{\mu}$

$$\vec{\mu} = -\frac{e}{2m_e}\vec{L} = -\mu_B\frac{\vec{L}}{\hbar} \tag{2.5}$$

where the Bohr magneton is $\mu_B = 5.788 \times 10^{-11}$ MeV T^{-1}. The interaction energy between a magnetic field and a magnetic dipole moment is then $\Delta E = -\vec{\mu}\cdot\vec{B}$. The normal Zeeman effect is due to the $\vec{\mu}$ caused by the electron's orbital angular momentum. If we let the direction of $\vec{B}$ define the Z-axis, the z component of the angular momentum takes the values $L_z = m_l\hbar$ with $m_l = 0, \pm1, \pm2, ..., \pm l$. Measuring this splitting of atomic levels in stars requires minimum values $B \sim 1$ G, but it has been measured with fields greater than 3×10^4 G in some A stars. For the Sun, sunspots of several kG are common. In the interstellar medium one typically measures Zeeman splitting in OH and water masers, or the hidrogen 21 cm line for neutral clouds and molecular bands. In the case of the hydrogen, three different transitions of the hyperfine splitting of the ground state are possible, with $\Delta m_l = 0, \pm1$. The unshifted frequency, $\nu_0 = 1.42$ GHz, corresponds the case $\Delta m_l = 0$, and the frequencies

$$\nu_\pm = \nu_0 \pm \frac{eB}{4\pi m_e c} \tag{2.6}$$

correspond to $\Delta m_l = \mp1$. This splitting in frequency is tiny compared to the Doppler broadening of the lines. Per km/s of random motion of the gas, the broadening is $\Delta\nu = \nu_0 v/c \approx 5$ Hz. While it is impossible to actually measure the splitting of the 21 cm line directly, partial information on the magnetic field can be recovered due to the transitions having different polarization properties.

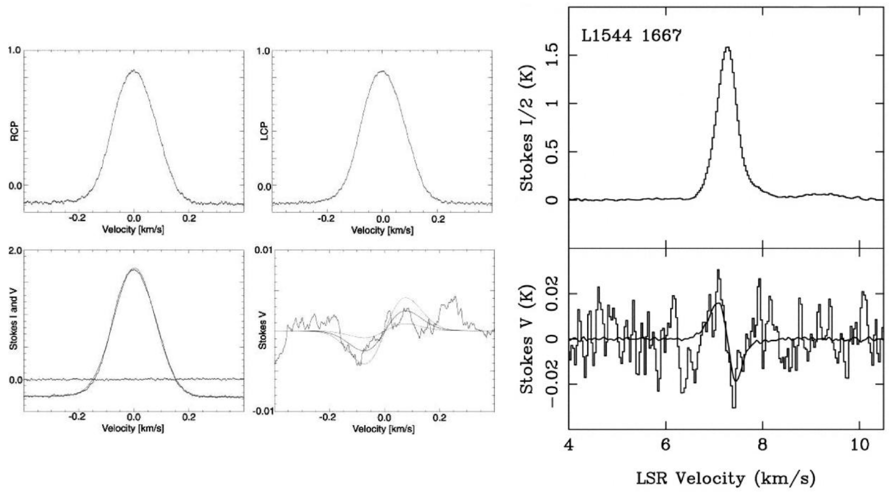

Figure 2.3: Examples of measurements of the Zeeman effect in interstellar clouds (Crutcher and Thomas, 2000).

2.2 Magnetohydrodinamic turbulence

A crucial aspect that explains the diffusive behaviour of CR propagation is the turbulent component of the galactic magnetic field. Hydrodynamic turbulence is a long studied but still incompletely addressed fundamental process, and yet it is just a first step towards the more complex mangetohydrodinamic (MHD) turbulence. MHD turbulence, or turbulence of conducting fluids, exists in different physical systems: liquid-metal experiments, fusion devices, the Earth's interior and virtually all astrophysical plasmas from stars to galaxies and galaxy clusters. Many observed properties of astrophysical bodies cannot be explained without recourse to some model of turbulence and turbulent transport in the constituent plasma.

MHD turbulence is an area of very active current research motivated by the recent rapid and simultaneous progress in astrophysical observations (especially of the solar photosphere, interstellar and intracluster medium), high-resolution numerical simulations, and liquid-metal laboratory experiments. In this section we would like to give an overview of the concepts underlying the MHD turbulence without going into the computational details.

Momentum conservation in a fluid implies Navier-Stokes equation, that provides the evolution of an element of fluid:

$$\frac{\partial \vec{u}}{\partial t} + \vec{u} \cdot \nabla \vec{u} = -\frac{1}{\rho} \nabla p + \nu \nabla^2 \vec{u} + \vec{f}. \tag{2.7}$$

Here $\vec{u}$ is the velocity field, in general a quantity that fluctuates in time t and space $\vec{x}$, ∇ is the gradient, ρ and p are the density and the pressure of the medium, respectively, ν is the kinematic viscosity (molecular viscosity/density), and $\vec{f}$ is the external force, i.e. excluding short-scale forces during particle-particle interactions. Turbulent flows are characterized by high Reynolds numbers:

$$R_e \equiv \frac{UL}{\nu}, \tag{2.8}$$

where U is the typical flow velocity (basically the root mean square of the velocity field), and L is a typical large scale of the (astro)-physical system. Regardless of how the flow becomes turbulent, once it does, the macroscopic random motions (namely, the non-linear convective term $u{\cdot}\nabla u$) dominate over the molecular viscosity (the dissipative term $\nu\nabla^2 u$). The specific energy injection mechanisms into the turbulent fluid are various: in astrophysics, they can be either background gradients, like the Kepler velocity shear in accretion discs, the temperature gradient ∇T in stellar convective zones, which enables the conversion of gravitational energy into kinetic energy of the fluid motion, or direct sources of energy such as supernovae in the IS medium or active galactic nuclei in galaxy clusters. However, even a small value of the viscosity could be responsible for the energy decay, which evolves from the largest to the smallest scales through a cascade described in terms of eddies, reflecting the vortical nature of the turbulence.

The breakthrough of a proper mathematical description of the nature of the turbulence came with the seminal paper in 1941 by Kolmogorov (usually known as K41), who applied simple dimensional arguments to get a heuristic theory on the origin of the turbulence spectrum (Kolmogorov, 1941). We can look at the basic picture of energy transfer process as follows. At the large-scale L a force is applied to the fluid, injecting energy into the flow. The fluid motion at this scale L becomes unstable and transfer energy to neighbouring smaller scales, without directly dissipating energy into heat: the largest eddies produce others that, in turn, subdivide, and so on. The process repeats itself until one reaches a dissipation scale, or the Kolmogorov scale l_ν , where the energy is finally dispersed into heat by the action of the molecular viscosity.

The phenomenology of the energy containing eddies gives a reasonable picture of global energy decay and makes clear how the energy reservoir at the large scales controls the process. The Kolmogorov's assumption was that the energy transfer and interacting scales are local, while the large-scale dynamics depend on the specific astrophysical context. The cornerstone of all theories of turbulence is the universality of the non-linear dynamics at small scales $\ll L$. Once steady state conditions are reached, *the energy dussipation rate* ϵ is transfered from any eddy to eddies at lower scales, until the smaller eddies are reached for which the scale Reynolds number is no longer larger than unit and viscosity transforms this energy into heat.

In addition to the universality of the non-linear processes at all scales belonging to the inertial range, hydrodynamic turbulence theory assumes

- homogeneity
- scale invariance
- isotropy
- locality of interactions

Under these assumptions, it is easy to derive the well-known 5/3 Kolmogorov spectral index for the distribution of kinetic energy $W(k)$ at the different scales:

$$W(k) = C_k \epsilon^{2/3} k^{-5/3}. \tag{2.9}$$

Here, C_k is the Kolmogorov constant, k is the wave number associated to the inertial range scales ($l \propto 1/k$) and ϵ is the energy transfer rate between the different eddies. The spectrum is proposed from purely dimensional considerations.

2.3 Spectrum of turbulent magnetic fields in our galaxy

The spectrum of the random component of the magnetic field in the interstellar medium of the Milky Way can be investigated with theory, observations and simulations. However the results obtained with all these tools do not coincide, what in practice means that we are far from establishing and understanding them. It is usually assumed that the spectrum of turbulences follows a power-law,

$$W(k) \propto k^{-\alpha}\,, \tag{2.10}$$

but the uncertainties in α (at different values of k) are very large. The largest scale corresponds to the size of the galaxy itself, 15 kpc, and the lowest scale (where viscosity transforms into heat the energy transferred in the turbulent cascade) is about 10^{-2}pc. The main injection of energy to the turbulent flow is coming from supernova remnants driven winds, at scales around 100 pc.

As explained before, theoretical arguments favour a Kolmogorov spectrum with $\alpha = 5/3$. It is expected to be roughly valid at intermediate scales between 1 pc and 1 Kpc. Observational analyses can be found in (Han et al., 2004) and (Han, 2009). Between the largest scale and 0.5 kpc it is found that $\alpha = 0.37$ To reach these larger scales, being the SNR the energy input scale, you need an inverse cascade transferring energy toward larger scales. However, the coefficient obtained in simulations at these larger scales (Brandenburg and Rekowski, 2001) is clearly incompatible with the 0.37 value. Probably, effects other than SN winds and inverse cascade are at work. For instance, shear associated to spiral arms and bars are mechanisms beyond the scope of standard analysis and the many implicit assumptions required by simulations.

2.4 Regular and turbulent magnetic fields

The magnetic field in the diffuse IS medium includes a large-scale regular component plus a turbulent component at smaller scales. A standard estimate for the strength of the local (galactic) magnetic field is 6±2 μG (Beck, 2001). The ratio between the random and the regular field strengths is estimated from starlight and synchrotron data to be 0.6 to 1.0, but it is expected to vary throughout the galaxy: the total field in the optical arms is the strongest, and it is mainly turbulent; in the inter-arm regions the regular field may dominate, possibly forming magnetic arms that extend beyond the optical arms. Within 200 pc of the galactic center (Ferriere, 2009), we can estimate $B \approx 10$ μG and a poloidal compound in the diffuse medium, and $B \approx 1m$G in filaments and dense clouds.

We can then separate the local magnetic field

$$\vec{B} = \vec{B_R} + \vec{B_T}, \tag{2.11}$$

where $\vec{B_R}$ and $\vec{B_T}$ are the regular and the turbulent components, respectively. As described above, $\vec{B_R}$ a spiral shape reminiscent of the matter distribution in the disk. The component of $\vec{B_R}$ orthogonal to the disk (pitch angle) is difficult to measure (Vallée, 2004) and is spatially varying. Locally, it is estimated 10°, where 0° corresponds to a completely azimuthal field. The Sun is located between the Perseus and the Sagittarius spiral arms. The local galactic magnetic field points clockwise to the Perseus arm (located outside the solar circle), and counter-clockwise in the Sagittarius arm (Beck and Wielebinsky, 2005). The nature and the number of large scale field reversals are still open questions (see Fig. 2.3). In addition, new measures using WMAP polarization data of the field in the disk and halo of our galaxy favor an axisymmetric magnetic field (see Fig.2.5).

The most recent models for the regular magnetic field in our galaxy have been presented by (Oppermann et al., 2014) using Faraday rotation of extragalactic sources, (Ruiz-Granados et al., 2010) from WMAP data using CMB measurements. It is expected a similar estimate from Planck data. The current understanding of the galactic magnetic field can then be summarised as follows.

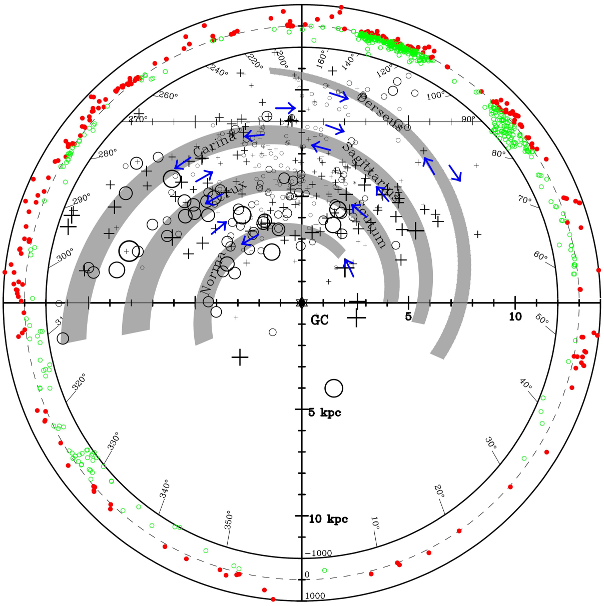

Figure 2.4: Rotation measures obtained from pulsars with known distances, superimposed onto a sketch of the Milky-Way spiral arms (Han et al., 2006).

- Magnetic fields are present everywhere in the Milky Way.
- There is a large-scale magnetic field, directed clockwise.
- A field reversal is evident in the Sagittarius spiral arm.
- In our vicinity we have a regular component $B_R \approx 5\,\mu$G and a turbulent component $B_T \leq 5\,\mu$G.
- The field strength drops as a function of galacto-centric distance, from $B_R \approx 10\,\mu$G at $R = 4$ kpc to $B_R \approx 4\,\mu$G at $R \geq 15$ kpc.

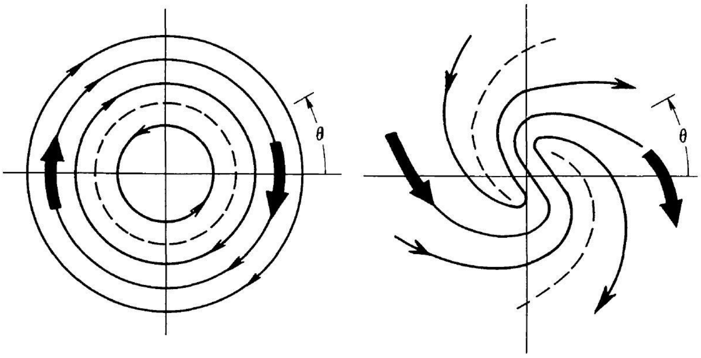

Figure 2.5: Examples of axisymmetric and bisymmetric magnetic field structures.

2.5 Magnetic field in the heliosphere

At small scale, magnetic fields in the interplanetaary region take a completely different configuration dominated by the stellar wind field.

In particular, the solar wind field is dominant in the so called heliosphere. The solar wind carries out the frozen-in Sun field. Because of the motion of the Sun with respect to the IS medium, the heliosphere becomes highly elongated developping a sharp wave front, the heliopause. Clearly, the close field around the Earth affects the trajectories of CR so they must be considered for interpreting CR arrival fluxes.

The solar corona is a highly conducting plasma. With increasing height, an increasing temperature results into a pressure-driven solar wind outflow (Parker, 1958), that produces a magnetic wind. Thus, the solar wind drags the coronal magnetic field out into the Solar System forming the heliospheric magnetic field, historically referred to as the interplanetary magnetic field. The structure and dynamics of the heliospheric magnetic field are key to understand and forecast the space weather, as it directly couples the Sun with planetary magnetospheres and channels the flow of solar and cosmic particles. The heliospheric magnetic field is providing strong constraints on theories of solar wind formation and solar dynamo.

Information about the heliospheric magnetic field can be obtained through a variety of indirect means, but the bulk of our understanding comes from spacecraft-borne magnetometers, making in situ observations. The first observations were made by the MARINER in the early 1960s. Subsequent spacecrafts have provided a complete record of the near-Earth heliospheric magnetic field, that can be found in the OMNI dataset (Papitashvili et al., 2000).

The solar magnetic field evolves on a range of time scales, from seconds to centuries. At the shortest time scales, waves and turbulence result in a fine-scale structure. The solar wind, and hence the heliospheric magnetic field, exhibits recurrence at the 25.4 day solar rotation period. There is also the 11-year solar cycle between periods of maximum and minimal activity. Nevertheless, much of the structure of the heliospheric magnetic field can be understood by the steady-state approximation. The intensity of this heliospheric field at 1 AU varies from 2 to 4 μG in correlation with the solar cycle (Balogh and Erdõs, 2013).

The large scale structure and dynamics of the heliospheric magnetic field is governed by the solar wind flow, which in turn has its origin in the magnetic structure of the corona. The simplest steady-state picture is observed under solar minimum conditions when the coronal magnetic field is closest to dipolar, typically with the magnetic dipole axis tilted by a few degrees to the solar rotation axis. The corona is observed to be organised into a belt of dense bright streamers around the magnetic equator with darker polar coronal holes in the high latitude regions. At this time a fast solar wind (with speeds $\approx 750\,\mathrm{km/s}$) fills most of the heliosphere, flowing outwards from the Sun from the regions of open magnetic field lines originating in the polar coronal holes. However, a belt of slower solar wind (with typical speeds of $300 - 400\,\mathrm{km/s}$) of about 20° latitudinal width originates from the streamer belt region corresponding to the magnetic equator. The magnetic field boundary separating oppositely directed magnetic field lines originating from the northern and southern polar coronal holes is carried out by this slower solar wind to form the heliospheric current sheet or Parker sheet, a large scale magnetic boundary which extends throughout the heliosphere.

Close to the Sun, in a spatial region approximately bounding the solar corona, the magnetic field dominates the plasma flow and undergoes significant non-radial (or super-radial) expansion with height. At the source surface, typically taken to be a few solar radii, the magnetic pressure-driven expansion of the solar wind dominates and both the field and flow both become purely radial. In the heliosphere, rotation of the heliospheric magnetic field (Hmagnetic field) footpoints within a radial solar wind flow generates an azimuthal component

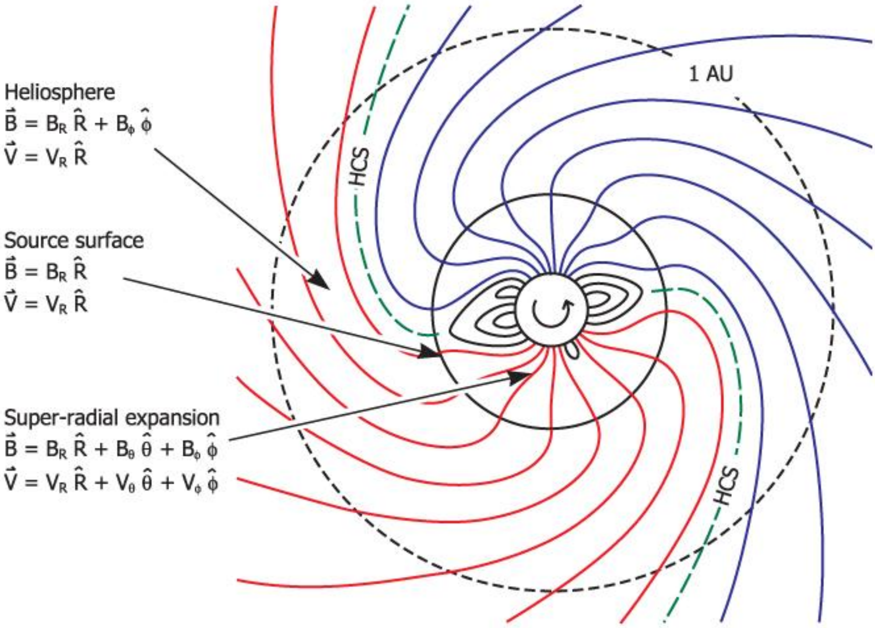

Figure 2.6: A sketch of the steady-state solar magnetic field in the ecliptic plane.

of the Hmagnetic field, leading to a spiral geometry. Regions of opposite HMF polarity, shown as red and blue lines, are separated by the heliospheric current sheet (HCS), shown as the green dashed line (Altschuler and Newkirk Jr, 1969).

The underlying geometry of the heliospheric magnetic field can be understood by considering a completely steady state idealised solar wind with an exactly radial outflow of constant speed, independent of radial and latitudinal position. The footpoints of the magnetic field lines are assumed to be fixed in the photosphere and, hence, to rotate with the Sun. The magnetic field is assumed to be frozen in to solar wind plasma, but to exert no force on it. Under such conditions, the heliospheric magnetic field becomes twisted into an Archimedean spiral in the solar equatorial plane, as predicted by (Parker, 1958) and shown schematically in figure 2.6.

2.5.1 Outer Heliosphere

With the Voyager 1 spacecraft having recently passed the heliopause (Gurnett et al., 2013) and Voyager 2 close behind, our understanding of the outer heliosphere is evolving rapidly (for a detailed discussion, see (Zank, 1999), (Frisch et al., 2009), (Balogh and Jokipii, 2009). A commonly accepted value of the local IS magnetic field is 3 μG (Pogorelov et al., 2008).

The global structure of the heliosphere and its interaction with the local IS medium can be largely understood through magnetohydrodynamic simulations (Zank, 1999). A sketch of the expected plasma and magnetic field boundaries is shown in figure 2.7. The motion of the Sun and heliosphere relative to the IS medium is 23 km s^{-1} (Linsky, 1998). Given the uncertainty in the local IS magnetic field strength and orientation, there is still some debate about whether this motion is super Alfvenic and, thus, results in a standing bow shock within the local

IS medium. Recent observations from the IBEX mission (McComas et al., 2009), however, argue that the orientation of the IS magnetic field is such that the interaction is submagnetosonic (McComas et al., 2012). Much like the interaction of the Earth's magnetosphere with the solar wind, the heliopause is expected to be compressed on the IS medium up-stream side and extended on the down-stream side. The super Alfvenic solar wind outflow produces a standing termination shock inside the heliopause, which compresses, slows and deflects the solar wind flow.

The Voyager 1 spacecraft crossed the termination shock in December 2004 at 94 AU (Stone et al., 2005), while Voyager 2 made its entry into the heliosheath in August 2007 at 84 AU (Stone et al., 2008). The inclination in the magnetic field of the local IS medium relative to that of the heliosphere may lead to further asymmetries near the heliopause (McComas et al., 2011). Voyager 1 recently encountered a region of flow stagnation, where the solar wind speed reached zero (Krimigis et al., 2011), before measuring an electron density enhancement consistent with the interstellar medium in April 2013 (Gurnett et al., 2013).

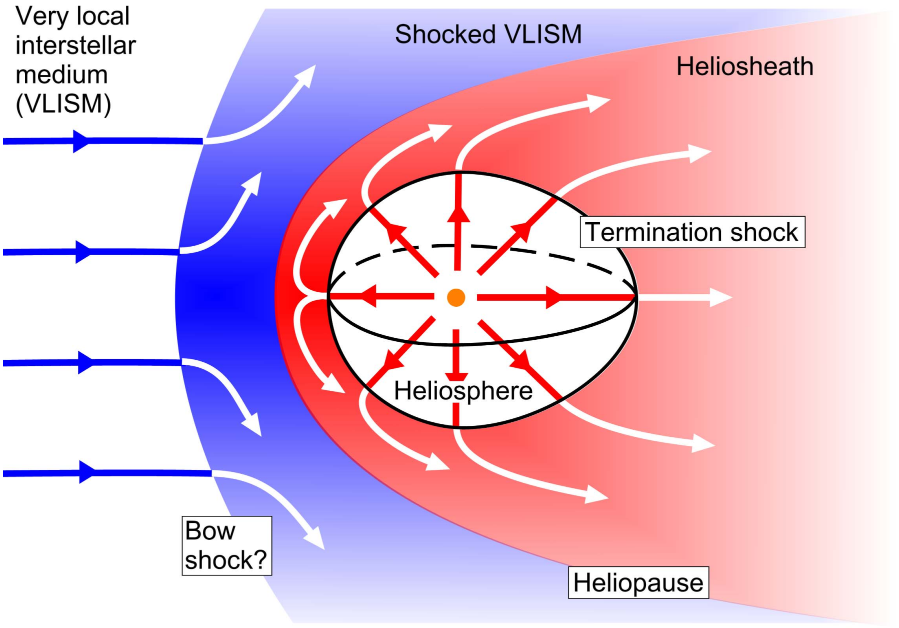

Figure 2.7: Global structure of the heliosphere. The solar wind flows radially away from the Sun. As the flow is supersonic, a termination shock forms inside the heliopause, to slow and deflect the solar wind inside the heliosheath. Outside the heliopause, the local IS medium is deflected around the heliosphere. Depending on the strength and orientation of the magnetic field within the IS medium, this interaction may or may not involve a standing bow shock.

Chapter 3

Cosmic magnetic lenses

In this chapter we study in detail the trajectories of a CR in the presence of a regular magnetic field. We find this approximate situation when CRs propagate both in the IS medium (where there is a dominant field of order 3 μG with a coherence of 0.1–10 pc) and inside the heliosphere (where CRs find the Parker field). We will also discuss an interesting field configuration that we have named as cosmic magnetic lens (CML). The trajectories considered in this chapter will be disturbed by magnetic turbulences, but some effects should *survive* at distances where the diffuse regime has not been fully stablished (see discusion of Liouville's theorem in Chapter 4). In particular, the results in this chapter will be necessary to understand the appearance of small and medium-scale anisotropies, to estimate the relevance of the heliospheric field, and to evaluate the effect of the *shadow of the Sun* in the large-scale anisotropy.

3.1 Image of a point-like source

Let us start discussing the trajectory of a particle in the presence of a stationary magnetic field. The Newton-Lorentz equation reads (we use cgs units)

$$\frac{d}{dt}\vec{p} = q\left(\vec{E} + \frac{\vec{v}}{c} \times \vec{B}\right) , \tag{3.1}$$

where q is the electric charge and $\vec{v}$ the velocity of the CR. We will assume that, because of the high conductivity in cosmic plasmas, there are no large-scale electric fields:

$$\vec{E} = 0 \tag{3.2}$$

We will initially consider the case of a homogeneous regular field $\vec{B}_0$, and will choose our Cartesian coordinates such that the Z-axis is parallel to that background field:

$$\vec{B} = B_0 \vec{e}_z + \delta\vec{B} \, . \tag{3.3}$$

Notice that in absence of an electric field the energy of the particle will be constant,

$$\frac{dE^2}{dt} = \frac{d}{dt}\left(c^2\,\vec{p}\cdot\vec{p}\right) = 2c^2\,\vec{p}\cdot\frac{d\vec{p}}{dt} = 2c^2 q\,\vec{p}\cdot\left(\frac{\vec{v}}{c} \times \vec{B}\right) = 0\, . \tag{3.4}$$

The equations of motion are then

$$\dot{v}_x = \Omega v_y + \Omega\left(v_y\frac{\delta B_z}{B_0} - v_y\frac{\delta B_y}{B_0}\right) \tag{3.5}$$

$$\dot{v}_y = -\Omega v_x + \Omega\left(v_z\frac{\delta B_x}{B_0} - v_x\frac{\delta B_z}{B_0}\right) \tag{3.6}$$

$$\dot{v}_z = \Omega\left(v_x\frac{\delta B_y}{B_0} - v_y\frac{\delta B_x}{B_0}\right) \tag{3.7}$$

where $p_i = m\gamma v_i$, $\gamma = 1/\sqrt{1 - v^2/c^2}$ and

$$\omega \equiv \frac{qB_0}{m\gamma c} = \frac{qB_0 c}{E}\,. \tag{3.8}$$

In this chapter we will discuss the case where the turbulent perturbations ($\delta B_i = 0$) can be neglected. The equations are then

$$\begin{aligned} \dot{v}_x &= \omega v_y \\ \dot{v}_y &= -\omega v_x \\ \dot{v}_z &= 0\,, \end{aligned} \tag{3.9}$$

with solution

$$\begin{aligned} v_x &= v_\perp \cos(\phi_0 - \omega t) \\ v_y &= v_\perp \sin(\phi_0 - \omega t) \\ v_z &= v_\parallel = \text{constant}\,, \end{aligned} \tag{3.10}$$

where $v_\parallel$ and $v_\perp$ are the components of $\vec{v}$ parallel and perpendicular to $\vec{B}_0$, respectively, and the parameter ϕ_0 denotes the initial gyrophase. We find

$$\begin{aligned} x(t) &= x_0 - \frac{v_\perp}{\omega}\sin(\phi_0) + \frac{v_\perp}{\omega}\sin(\phi_0 - \omega t), \\ y(t) &= y_0 + \frac{v_\perp}{\omega}\cos(\phi_0) - \frac{v_\perp}{\omega}\cos(\phi_0 - \omega t), \\ z(t) &= z_0 + v_\parallel t\,. \end{aligned} \tag{3.11}$$

This is an helix with the center of rotation in the XY plane at

$$\begin{aligned} x_m &= x_0 - \frac{v_\perp}{\Omega}\sin\phi_0, \\ y_m &= y_0 + \frac{v_\perp}{\Omega}\cos\phi_0, \end{aligned} \tag{3.12}$$

and radius (gyroradius)

$$r_g = \frac{v_\perp}{\Omega} \tag{3.13}$$

The parameter Ω can be identified with the gyrofrequency of the trajectory. It is convenient to introduce the angle ϕ_P of the velocity along $\vec{B}_0$. Its cosine defines the so called *pitch* $\mu = \cos\phi_P$, which is conserved for un unperturbed constant field. The gyroradius and the two components of the velocity are then

$$\begin{aligned} r &= r_L\sqrt{1-\mu^2} && (3.14)\\ v_\perp &= v\sqrt{1-\mu^2} && (3.15)\\ v_\parallel &= v\mu\,, && (3.16) \end{aligned}$$

where the Larmor radius is $r_L = \frac{v}{\Omega}$.

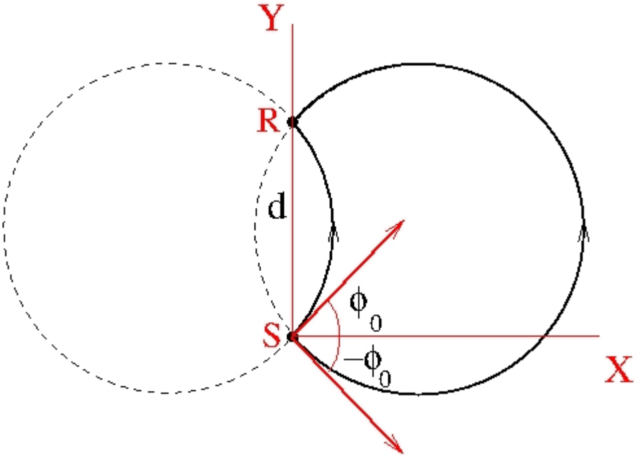

Figure 3.1: Trajectories between $S = (0,0,0)$ and $R = (0, d_\perp, 0)$ for $\vec{B}_{IS} = (0,0,B_{IS})$.

It is instructive to study the image of a point-like CR source in the presence of such a constant field. Let us take a particle of energy $E \gg mc^2$ and $v \approx c$ leaving the source $S = (0,0,0)$ at $t = 0$. The gyroradius is $r(\mu) = c\sqrt{1-\mu^2}/\Omega$, and the particle will follow the trajectory

$$\begin{array}{rcl} x & = & -r(\mu)\ \sin\phi_0 + r(\mu)\ \sin(\phi_0 + \omega\, t) \\ y & = & r(\mu)\ \cos\phi_0 - r(\mu)\ \cos(\phi_0 + \omega\, t) \\ z & = & c\,\mu\, t\,, \end{array} \tag{3.17}$$

where $\mu = v_\parallel/c$ and ϕ_0 is the initial angle of $v_\perp$ with the X axis.

The trajectory may connect the source S with an observer R only if the transverse distance is smaller than the gyroradius, $d_\perp \leq c/\omega = r_L$. We can always rotate the axes so that R is at $(0, d_\perp, d_\parallel)$ and use the variables (μ, ϕ_0, t) to solve $(x, y, z) = (0, d_\perp, d_\parallel)$. It turns out that there is an infinite number of such trajectories, each one characterized by an integer *winding* number $n \geq n_{\rm min}$, with

$$n_{\rm min} = \text{Integer}\left[\frac{d_\parallel}{\pi\sqrt{4r_L^2 - d_\perp^2}}\right]\,, \tag{3.18}$$

and a (positive or negative) ϕ_0 with $|\phi_0| \leq \pi/2$. To see this let us first consider the case with S and R in the XY plane, *i.e.*, $d_\parallel = 0$ (see figure 3.1). In this case there are two *families* of trajectories connecting S and R, both with $\mu = 0$ but with opposite initial phase: $\phi_0^- = -\phi_0^+$. These trajectories will reach R after an arbitrary number n of turns around the left or the right circles in Fig. 3.1. Notice that higher values of n correspond to longer trajectories, which will provide fainter images of S (the flux reaching R scales like $1/L^2$).

Taking R out the the XY plane ($d_\parallel > 0$) the trajectories will require a non-zero value of μ to reach R. In this case their total length will be $L = d_\parallel/\mu$. Therefore, trajectories with larger values of

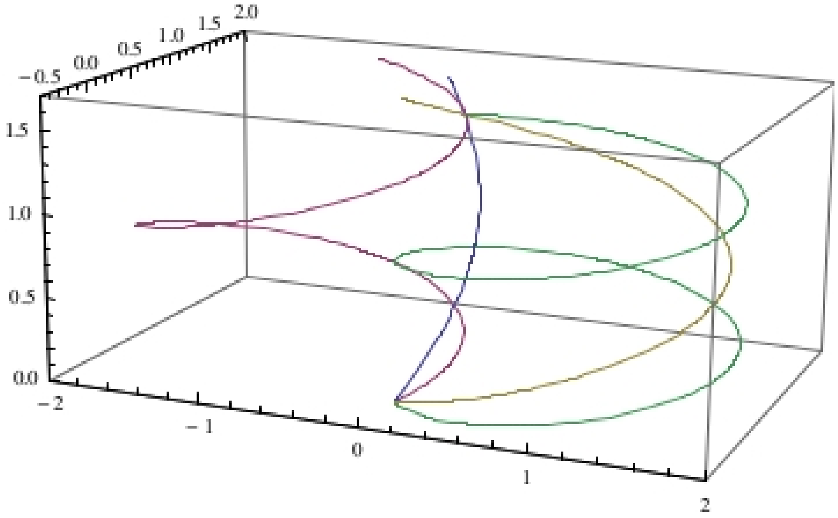

Figure 3.2: Three possible CRs paths connecting two points in a regular magnetic field.

μ will be brighter, although this parameter is bounded by the condition $r_L\sqrt{1-\mu^2} \geq d_\perp/2$.

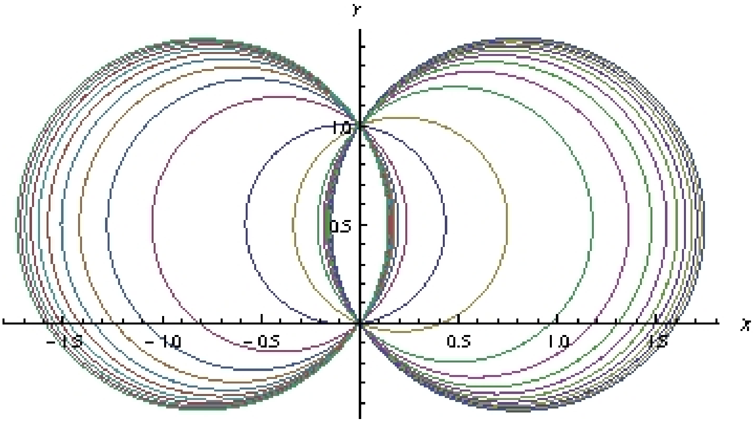

Figure 3.3: Proyection of the twenty shortest trajectories between $S = (0,0,0)$ and $R = (0,1,35)$ for $\vec{B}_{IS} = (0,0,B_{IS})$ and $r_L = 1$

In Figs. 3.3 and 3.4 we plot several trajectories connecting S and R for a large ($d_\| = 35r_L$) longitudinal distance. In the limit of very large $d_\|$ the trajectories reach R defining a semi-conus of directions of angle $\theta = \arccos d_\perp/(2r_L)$, with $-\pi/2 < \varphi < \pi/2$ and the limiting directions ($\varphi = \pm\pi/2$) defining the plane orthogonal to $\vec{B}_{IS}$. It is easy to see that the trajectories with direction $\varphi = 0$ and maximum μ are shorter but less dense than the ones in the extremes. As a consequence, the brightness (number of trajectories per unit length times their flux) along the semicircle scales like

$$\mathcal{B} = \mathcal{B}_0 \cos\left(\varphi + \pi/2\right) . \tag{3.19}$$

Notice also that each trajectory reaching R corresponds to a CR that left the source S at a different time, so the image at R would be the whole semicircle only for a constant and isotropic source.

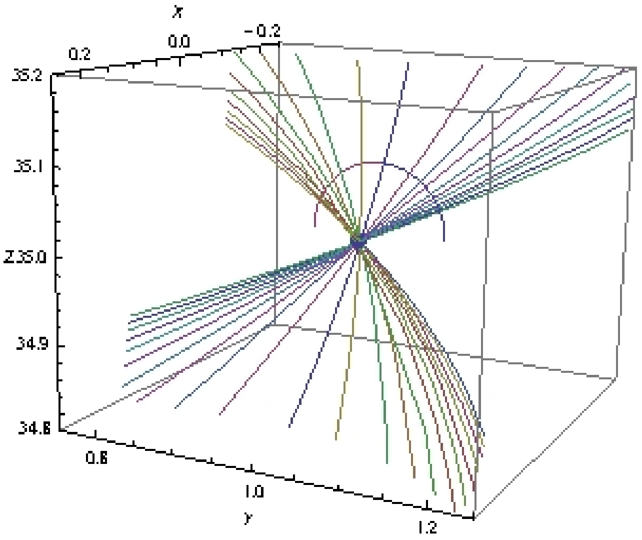

Figure 3.4: Twenty shortest trajectories between $S = (0,0,0)$ and $R = (0,1,35)$ for $\vec{B}_{IS} = (0,0,B_{IS})$ and $r_L = 1$. In the limit $d_\parallel \gg d_\perp$ the source is *seen* at R as a semi-conus of angle $\theta = \arccos d_\perp/(2r_L)$ with its axis along X and the limiting directions ($\varphi = \pm\pi/2$) defining the XY plane.

We conclude that pointlike sources may be *seen* as lines due to the presence of a magnetic field. In Chapter 5 we describe short and medium scale anistropies that present this generic features.

3.2 The shadow of the Sun

As discussed in Chapter 2, the Sun has a regular magnetic field that goes from $B \approx 100m\text{G}$ at $r = 2R_\odot$ to $B \approx 50\mu\text{G}$ at $r = 1$ AU. Its shape is known as Parker spiral (Parker, 1958). More precisely, the mean heliospheric magnetic field is given by

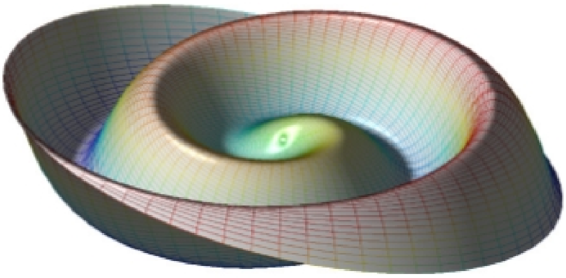

Figure 3.5: Wavy heliospheric magnetic current (Parker sheet) based on equation 3.20 displayed out to a radius of 10 AU.

$$\vec{B} = \frac{A}{r^2}\left(\vec{e_r} - v\frac{(r-rs)\omega_\odot}{V}\sin\theta\,\vec{e}_\phi\right)\left[1-2H(\theta-\theta_{cs})\right], \qquad (3.20)$$

where $\vec{e_r}, \vec{e_\phi}$ are unitary vectors in the radial and azimtuhal directions, respectively, $A = \pm B_{0_r} r_0^2$ is a constant whose sign depends on the 11 year solar cycle, $\Omega_\odot$ is the sideral solar rotation rate corresponding to a period of 25.4 days and H indicates the Heaviside step function. The polar angle of the current, θ_{cs}, is determined by the equation

$$tan\left(\frac{\pi}{2}-\theta_{cs}\right) = \tan\alpha\,\sin\left[\phi+\frac{\Omega_\odot(r-r_s}{V}-\Omega_\odot(t-t_0)\right] = \tan\alpha\,\sin\phi_0 \tag{3.21}$$

with α the tilt angle and $\phi_0 = \phi + (r-r_s)\Omega_\odot/V - \Omega_\odot(t-t_0)$. The shape of the heliospheric current sheet changes with time and position. To estimate the effect of the magnetic field we will *freeze* it and take a snapshot of at t_0 (see figure 3.5).

Using this model for the magnetic field we have simulated numerically CR trajectories for energies between 100 GeV and 100 TeV. In particular, we have found those that connect the Sun with the Earth. Trajectories that were aiming to the observer at the Earth but have been absorbed by the Sun determine the *shadow of the Sun.*

We obtain that at energies below 500 GeV there is no visible CR shadow: no CR trajectory external to the Sun can connect its surface ($r \approx R_\odot$) and the Earth: these trajectories experience a *mirror* effect at distances larger than 1.5 $R_\odot$ (see Fig.3.6). At energies around 1 TeV there appears a shadow that initially is separated $\approx 5^\circ$ from the real position of the Sun, and that at 10 TeV overlaps with it (see figure 3.7).

As the Earth moves relative to the Sun this shadow will span a region of the sky that, in galactic coordinates, extends along r.a. $(0^\circ - 360^\circ$ and declinations $-23.5^\circ\, to\, 23.5^\circ$. This gives a total solid angle of $\Delta\Omega \approx 1.04\,\pi$ sr. The angular size of the Sun is

$$\Delta\Omega_\odot = \frac{\pi R_\odot^2}{R_{ES}^2} \approx 7.0\times10^{-5}\ \mathrm{sr}\,. \tag{3.22}$$

Therefore, if we *dilute* the shadow over the region in the sky where it

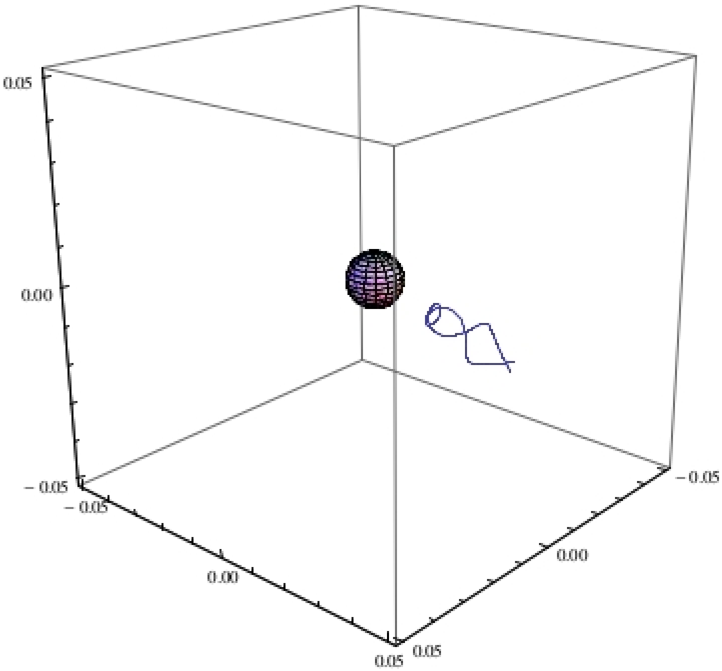

Figure 3.6: CR (1 TeV) trajectory near the Sun (sphere of 1.5 $R_{\odot}$) with the heliospheric field producing a mirror effect.

can be found we obtain a deficit of order

$$\delta_S = \frac{\Delta\Omega_\odot}{\Delta\Omega} \approx 2.1 \cdot 10^{-5} \,. \tag{3.23}$$

The deficit that we will discuss in Chapter 5 is one order of magnitude higher at TeV energies and has a different location in the sky, so its origin should also be different.

In addition, our analysis above justifies a non heliospheric origin for any anistropies in the CR flux at energies higher than 1 TeV-scales. Above these energies the trajectories coming from the edge of the heliosphere, at ≈ 75 AU from the Sun, will experience a deflection of just a few degrees. The TeV CR anisotropies must be originated outside the Solar System.

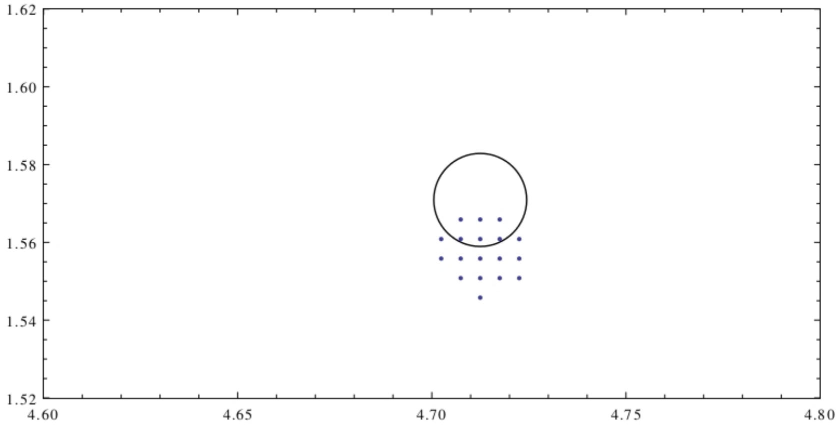

Figure 3.7: Shadow of the sun displaced by the Parker field for a CR energy of 10 TeV.

3.3 Cosmic magnetic lenses

We would like to discuss in some detail a third magnetic field configuration that may play a role in the generation of anisotropies and we called (Battaner et al., 2010) cosmic magnetic lens (CML). The term magnetic lensing had already been used in the literature to describe, generically, the curved path of CRs through a magnetized medium. In (Harari et al., 2002) is studied the effect of galactic fields, showing that they may produce magnification, angular clustering and caustics. In (Dolag and Bartelmann, 1997) is considered lensing by the tangled field of the Virgo cluster, assuming that the galaxy M87 was the single source of ultrahigh energy cosmic rays. In (Shaviv et al., 1999) is studied the lensing near ultramagnetized neutron stars. Our point of view, however, will be different. The CML will be defined by a basic magnetic-field configuration with axial symmetry that could appear in astrophysical objects at any scale: from clusters of galaxies to planetary systems. The effect of the CML on galactic CR of energy $E < 10^9\,GeV$ will not be significantly altered by turbulent fields if its magnetic field in the lens is substantially stronger than the average background field and of its distance to the Earth shorter than the one required to fully stablish a diffusive regime. Since the CML is a definite object, we can separate source, magnetic lens and observer. Although it is not a lens in the geometrical optics sense (the CML does not have a focus), its effects are generic and easy to parametrize, analogous to the ones derived from a gravitational lens (with no focus neither).

3.3.1 Basic magnetic lens

The basic configuration that we will consider is an azimuthal mean field $\vec{B}$ in a disk of radius R and thickness D. The field lines are then circles of radius $\rho \leq R$ around the disk axis. As a first approximation we will take a constant intensity B, neglecting any dependence on ρ (notice, however, that a more realistic B should vanish smoothly at $\rho = 0$ and be continuous at $\rho = R$). Our assumption will simplify the analysis while providing all the main effects of a magnetic lens. The disk of most spiral galaxies has a large toroidal component of this type (Sofue et al., 1986), so they are obvious candidates. The configuration describing the CML would be natural wherever there is ionized gas in a region with turbulence, differential rotation and axial symmetry, since in such environment the magnetic field tends to be amplified by the dynamo effect (Parker, 1971). We will then assume that it may appear at any scale R with an arbitrary value of B.

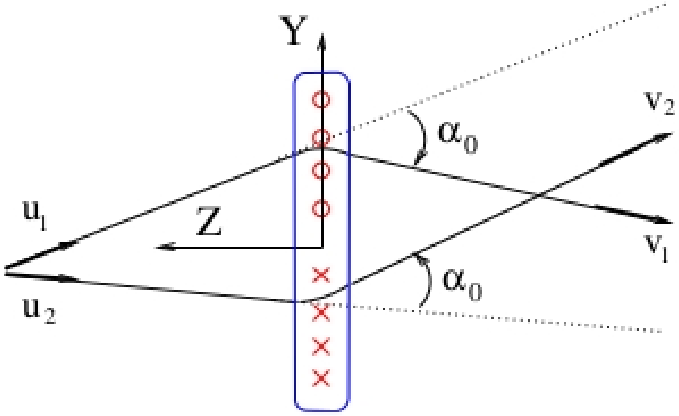

Figure 3.8: Trajectories in x = 0 plane. $\vec{B} \propto (1, 0, 0)$ at $y > 0$ and $\vec{B} \propto (-1, 0, 0)$ at $y < 0$.

Let us parametrize the magnetic field and its effect on a charged CR. If the lens lies in the XY plane with the center at the origin (see Fig. 3.8) B is[1]

$$\vec{B} = \begin{cases} \dfrac{B}{\rho}\,(y, -x, 0) & \text{if } \rho < R \text{ and } |z| < \dfrac{D}{2}\ ; \\ \\ 0 & \text{otherwise}\ , \end{cases} \tag{3.24}$$

whith $\rho \sim \sqrt{x^2 + y^2}$. To understand its effect, we will first consider a particle moving in the YZ ($x = 0$) plane with direction u (the case depicted in Fig. 3.8). When it enters the lens the cosmic ray finds an orthogonal magnetic field that curves its trajectory. The particle then rotates clockwise[2] around the axis $\vec{u}_B = \vec{B}/B$, describing a circle of gyroradius $r_g = E/(qB)$. The segment of the trajectory inside the lens has a length $l \sim D$, so the total rotation angle α_0 when it departs is

$$\alpha_0 \approx \frac{qBD}{E}. \tag{3.25}$$

The direction of the particle after crossing the lens is given by the rotated velocity $\vec{v} = R_B(\alpha_0)\vec{u}$. The angle α_0 will be the only parameter required to describe the effect of this basic lens. An important point is that $\vec{B}$ and the Lorentz force change sign if the trajectory crosses the lens through the region $y < 0$. In that case the deflection is equal in modulus but opposite to the one experience by particles crossing through $y > 0$ (see figure 3.8). Therefore, the effect of this lens is

---

[1] A continuous field configuration could be modelled just by adding a factor of $(1 - exp[(\rho/\rho_0)^{n_0}]) \times \exp[(\rho/R)^{n_R}] \times exp[(2z/D)^{n_D}]$. When the integers n_0 , n_R and n_D are chosen very large and ρ_0 very small we recover our disk with a null B at $\rho = 0$.

[2] We define a positive deviation α_0 if the rotation from $\vec{u}$ to $\vec{v}$ around the axis u_B is clockwise.

convergent, all trajectories are deflected the same angle α_0 towards the axis of the lens.

The effect on a generic trajectory within a plane not necessarily orthogonal to the lens is a bit more involved. It is convenient to separate

$$\vec{u} = \vec{u}_{||} + \vec{u}_{\perp} \tag{3.26}$$

$$\vec{v} = \vec{v}_{||} + \vec{v}_{\perp} \tag{3.27}$$

where $\vec{u}_{||} = (\vec{u} \cdot \vec{u}_B)\ \vec{u}_B$ and ${}_{u_\perp} = \vec{\vec{u}} - \vec{u}_{||}$ are parallel and orthogonal to the magnetic field, respectively (and analogously for $\vec{v}$). In this case the magnetic field will rotate the initial direction $\vec{u}$ an angle of $\alpha_0 = u_\perp \alpha_0$ around the axis $vecu_B : \vec{v} = R_B(u_\perp \alpha)\vec{u}$. This means that the parallel components of the initial and the final directions coincide,

$$u_{||} = \vec{u} \cdot \vec{u}_B = v_{||} \ , \tag{3.28}$$

whereas the orthogonal component $\vec{u}_\perp$, of modulus $u_\perp = \sqrt{1 - (\vec{u} \cdot \vec{u}_B)^2}$, rotates into

$$\vec{v}_\perp = \cos(u_\perp \alpha_0)\ \vec{u}_\perp - \sin(u_\perp \alpha_0)\ \vec{u}_B \times \vec{u}_\perp \ . \tag{3.29}$$

The focus depends on energy of the CR, therefore the CML has a alrge chromatic aberration, except for a particular $\vec{B}$ radial distribution inside the lens. The deviation α_0 caused by a given CML is proportional to the inverse energy of the cosmic ray. If E is small and $\alpha_0 > \pi/2$, then the lens acts randomly on charged particles, diffusing them in all directions. On the other hand, if E is large the deviation becomes small and is smeared out as the particle propagates to the Earth. Only a region of the CR spectrum can "see" the CML.

One could define a focal distance f by the relation

$$\alpha_0 = \frac{r}{f} \ , \tag{3.30}$$

where r denotes the distance from the center where the particle has impacted (see Fig. 3.9). However, we can then see that this focal distance is energy dependent (chromatic aberration) and also r dependent (spherical aberration). The possible dependence $B = B(r)$ would add this second type of aberration.

A final aspect that we would like to emphasize is that the same CML could act as a convergent or divergent depending on the charge of the incident CR. Moreover, the same change in the lens behaviour is observed when the same particle is crossing from one or the opposite side of the lens (see Fig. 3.9).

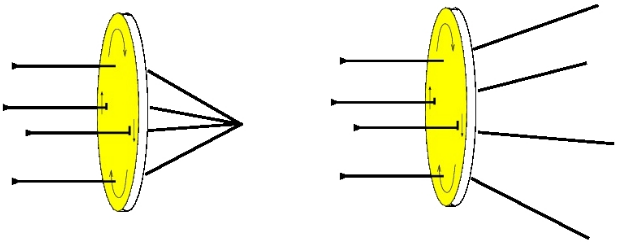

Figure 3.9: Convergent and divergent CMLs.

3.3.2 Point-like source trought a magnetic lens

Let us now study the image of a localized monochromatic source produced by the CML. We will consider a thin lens ($R \gg D$) located on the plane $z = 0$ (see Fig. 3.10). As described before, its effect on a CR can be parametrized in terms of the angle α_0 given in equation 3.41. The rotation axis is

$$\vec{u}_B = \frac{1}{\sqrt{x^2 + y^2}}(y, -x, 0), \tag{3.31}$$

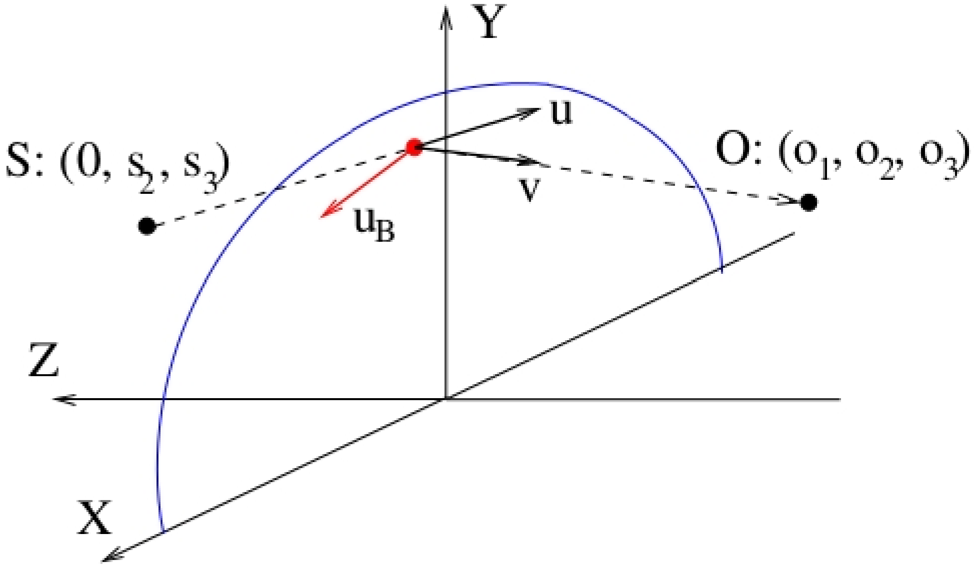

Figure 3.10: Trajectory from the source to the observer.

and the coordinates of source and observer are $S = (s_1, s_2, s_3)$ and $O = (o_1, o_2, o_3)$, respectively. We will use the axial symmetry of the lens to set $s_1 = 0$. The trajectory will intersect the CML at $(x, y, 0)$. There the initial direction $\vec{u}$ of the CR will change to $\vec{v}$, with

$$\vec{u} = \frac{(x, y - s_2, -s_3)}{\sqrt{x^2 + (y - s_2^2 + s_3^2}} \; \vec{v} = \frac{(o_1 - x, o_2 - y, o_3)}{\sqrt{(o_1 - x)^2 + (o_2 - y)^2 + o_3^2}}. \tag{3.32}$$

Therefore, given a source S, an observer O and a lens producing a deviation α_0 , we can determine the coordinates $(x, y, 0)$ where the rotation $R_B(u_\perp \alpha)$ described in the previous section exactly transforms $\vec{u}$ into $\vec{v}$. The first condition on x and y, given in Eq. (3.29), is that B does not change the longitudinal component of the velocity,

$$\vec{u} \cdot \vec{u}_B = \vec{v} \cdot \vec{u}_B. \tag{3.33}$$

The second one, derived from Eq. (3.30), defines the rotation of $\vec{u}_\perp$ produced by the magnetic field. It can be written ($u_\perp = |\sin\vec{u}\cdot\vec{B}|$):

$$\frac{\vec{v}_\perp\cdot\vec{u}_\perp}{u_\perp^2} = \cos(u_\perp\alpha_0)\ \frac{\vec{v}_\perp\cdot(\vec{u}_\perp\times\vec{u}_B)}{u_\perp^2} = \sin(u_\perp\alpha_0) \tag{3.34}$$

The second equation above is necessary to fully specify the rotation. Notice that $\alpha = u_\perp\alpha_0$ has a definite sign: positive for a convergent CML and negative for a divergent one. In addition, the solution must verify that $x^2+y^2<R^2$.

We find that for $R\to\infty$ and a convergent lens there is always at least one solution, whereas for a divergent one there is a region around the axis that may be hidden by the CML (this region disappears if B goes smoothly to zero at the center of the lens). To illustrate the different possibilities in Fig. 3.11 we have placed the observer in the axis at a distance L from the lens, $O=(0,0,L)$, and have parametrized the position of the source (at a distance d from the lens) as $S=(0,d\sin\beta,d\cos\beta)$. In this case $u_\parallel = 0 = v_\parallel$ and $u_{perp}=1$. If the lens is convergent ($\alpha_0>0$) and $|\beta|>\alpha_0$, then the image of the source is just a single point. For a source at $\mid\beta\mid<\alpha_0$ we obtain two solutions, which correspond to trajectories from above or below the center of the lens. For a source in the axis ($\beta=0$) the solution is a ring (analogous to Einstein's ring) of radius

$$r = \frac{d+L}{2\tan\alpha_0}\left(\sqrt{1+\frac{4dL\tan^2\alpha_0}{(d+L)^2}}-1\right). \tag{3.35}$$

If the observer is located out of the axis but still in the $x=0$ plane the possibilities are similar, but the ring becomes a cross similar to the one obtained through gravitational lensing. Finally, if we take the observer out of the $x=0$ plane there appears always a single solution.

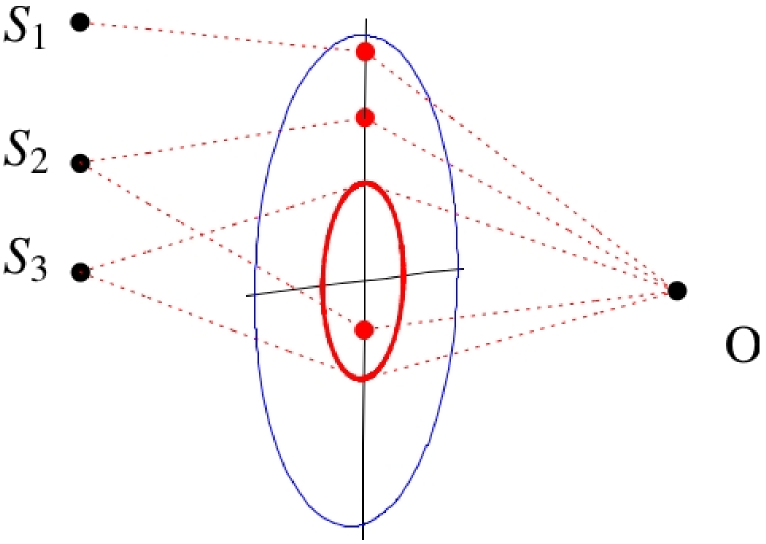

Figure 3.11: Trajectories with $\beta > \alpha$ (S_1), $\beta < \alpha$ (S_2) and $\beta = 0$ (S_3) for an observer at the axis.

3.3.3 Fluxes from distant sources

Let us finally explore how the presence of a CML changes the flux F of charged particles from a localized source S. It is instructive to consider the case where S is a homogeneous disk of radius R_S placed at a distance d from the lens and the observer O is at a large distance L,

$$R_S < d\,, \quad R \ll L\,, \tag{3.36}$$

as shown in figure 3.12. In addition, we will assume that the magnetic field defining the lens goes smoothly to zero near the axis, and that the source is monochromatic.

If there were no lens, O would see S under a solid angle

$$\triangle\Omega_0 \approx \pi \frac{R_s^2}{L^2}\,. \tag{3.37}$$

If all the points on S are equally bright and the emission is isotropic, the differential flux $dF/d\Omega$ from all the directions inside the cone $\triangle\Omega_0$ will be approximately constant, implying a total flux (number of particles per unit area)

$$F_0 = \int_{\triangle\Omega_0} d\Omega \frac{dF}{s\Omega} \approx \pi\, \frac{R_S^2}{L^2}\, \frac{dF}{d\Omega}\,. \tag{3.38}$$

The lens in front of S will deflect an approximate angle α all trajectories crossing far from the axis. In Fig. 3.12 we have pictured[3] the limiting directions reaching the observer, that define a solid angle

$$\triangle\Omega_+ \approx \pi \frac{(R_s + d\tan\alpha)^2}{L^2} \tag{3.39}$$

---

[3] A pointlike source in the axis is transformed by the lens into a ring, as explained before. As the source grows, the ring becomes thicker and eventually closes to a circle, which is the case considered in Fig. 3.12

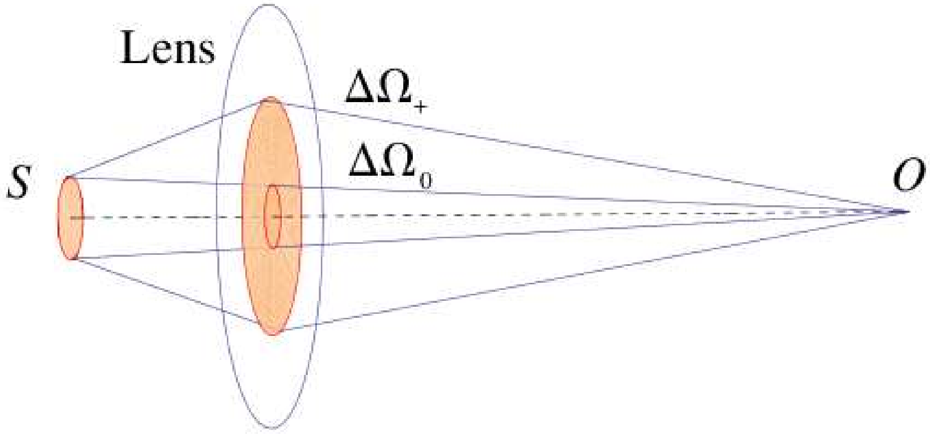

Figure 3.12: Cone of trajectories from S to O with and without a CML for a homogeneous and monochromatic source.

O sees now CRs from directions inside the larger cone $\triangle\Omega_+$ or, in other words, sees the radius R_S of the source amplified to $R_S + d\, tan\alpha$.

We can then use Liouville's theorem[4] to deduce how the flux observed by O is affected by the presence of the lens. This theorem, first applied to CR moving inside a magnetic field by Lemaître and Vallarta (Lemaitre and Vallarta, 1933), implies that an observer following a trajectory will always observe the same differential flux (or intensity, particles per unit area and solid angle) along the direction defined by that trajectory. For example, in the case with no lens, an observer in the axis at a distance $L' \gg L$ will still observe the same differential flux $dF/d\Omega$. However, the cone of directions that he sees will be smaller, $\triangle\Omega'_+ \approx \pi R_S/L'^2$, and the total flux from that source will scale like $F' \approx FL^2/L'^2$. The effect of the lens is then just to change the cone of directions reaching O from S, without changing the differential flux. This implies an integrated flux

$$F_+ \approx F_0 \frac{\triangle\Omega_+}{\triangle\Omega_0} \approx F_0 \left(1 + \frac{d^2 \tan^2 \alpha}{R_S^2}\right) \tag{3.40}$$

An important point is that the solid angle intervals $\triangle\Omega_{0,+}$ will in general be much smaller than the angular resolution at O. As a consequence, an observer trying to measure a differential flux will always include the whole cone $\triangle\Omega_{0,+}$ within the same solid angle bin: only the integrated fluxes $F_{0,+}$ (averaged over the angular resolution) are observable.

Now let us suppose that there are many similar sources at approximately the same distance from the observer and covering a certain range of directions. CR emitted from each source will reach O within a very tiny cone $\triangle\Omega_0$, and will be observed integrated over that cone and averaged over the angular resolution. If one of the sources has in front a CML, its cone $\triangle\Omega_+$ at O and thus its contribution to one of

---

[4] Liouville's theorem applied to CR flux will be discussed in chapter 4.

the direction bins will be larger, what would translate into a low-scale anisotropy[5] within the range of directions covered by the sources (see figure 3.13, left).

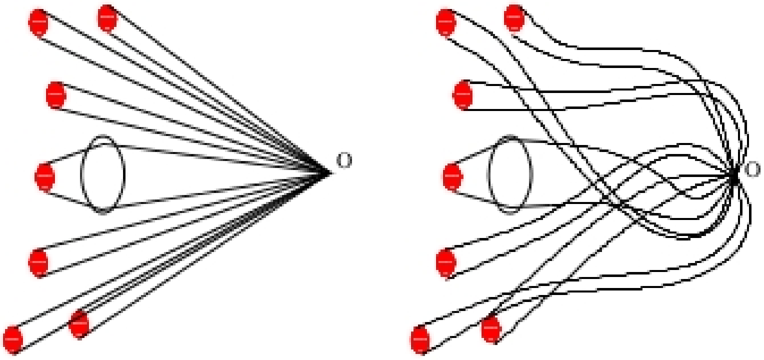

Figure 3.13: Trajectories from S to O without (left) and with (right) irregular magnetic fields along the trajectory.

In principle, this effect would not be erased by irregular magnetic fields from the source to the observer, that deflect the trajectories and tend to isotropize the fluxes (in Fig. 3.13, right). The contribution from the source behind the CML (reaching now O from a different direction) will still tend to be larger. The effect of the lens is to increase the size R_S of the source to $R_S + d \tan\alpha$; random magnetic fields will

---

[5] The direction of the source would be measured with a gaussian distribution that could take it to adjacent bins.

change the direction of arrival and the effective distance between S and O (i.e., the direction and the size of the cone from each source), but not the initial deflection produced by the lens nor (by Liouville's theorem) the differential flux within each tiny cone. Therefore, the cone from the source behind the lens tends to be larger, and when integrated and averaged over the resolution bin may still introduce a low-scale anisotropy.

The effect, however, tends to vanish if the cones are so small that the probability to observe two particles from the same cone of directions is smaller than the probability to observe particles from two disconnected cones with origin in the same source (i.e., in the deep diffuse regime disscused in next chapter where trajectories become random walks).

Finally, note that the effect of a divergent CML would be just the opposite. The presence of a lens could then introduce an excess for positive charged particles and a deffect for the negative ones (or a matter-antimatter asymmetry if both species were equally emitted by S).

3.3.4 Summary and outlook: Astrophysical objects with coherent magnetic fields

We have explored the effect on CRs of a very simple magnetic configuration: a constant azimuthal field in a thin disk that we identify as a CML. Such object acts on charged particles like a gravitational lens on photons, with some very interesting differences. Gravitational lenses are always convergent, whereas if a magnetic lens is convergent for protons and positrons, it changes to divergent for antiprotons and electrons. In addition, the deflection that the CML produces depends on the particle energy, so the lense is only visible in a very definite region (around one decade of energy) of the spectrum.

We can make an estimate of the size and magnetic intensity that would be requiered for a given CR energy. For a deviation $\alpha_0 = 0.1$, we obtain the relation

$$E = (2.3 \cdot 10^5 \text{ GeV}) \, \frac{e}{Q} \, \frac{10 \text{ mG}}{B} \, \frac{0.01 \text{ pc}}{D} \, . \tag{3.41}$$

To directly observe a lens it seems obviously hard because the medium will produce continuous deviations: just for magnetic fields in the CML much higher than the background one and near ballistic trajectories (subdiffusive distances), one may hope to detect an effect. Generically, however, the configuration defining the CML is natural and tends to be established by the dynamo effect. At the largest sizes and energies (around 10^9 GeV), the field in spiral galaxies $\vec{B}$ can be pure azimuthal (the one we have assumed), axisymmetric spiral or bisymmetric spiral, with or without reversals (Wielebinski and Beck, 2005), but in all cases the azimuthal component dominates. Our galaxy (Han, 2009), (Ruiz-Granados et al., 2008); it includes in the disk a spiral magnetic field of $B \approx 4\,\mu G$. This would actually requires that any analysis of magnetic lensing by other galaxies must subtract the effect produced by our own magnetic field. At smaller scales, CMLs could also be present in galactic halo, as there are observations of polarized synchrotron emission suggesting the presence of regular fields (Dettmar and Soida, 2006). Analogous indications (Bonafede et al., 2009) can be found for larger structures, like clusters and their halos. At smaller scales inside our galaxy the antisymmetric tori placed 1.5 kpc away in both hemispheres discovered by (Han et al., 1999) would also produce magnetic lensing on ultrahigh energy CR.

At even lower scales (20–800 pc) molecular clouds and HII regions (Delgado et al., 1997) are also potential candidates. Molecular clouds have strong regular fields in the range of $0.1 - 3$ mG (Crutcher, 2012). Moreover, many reversals in the field direction observed in our galaxy

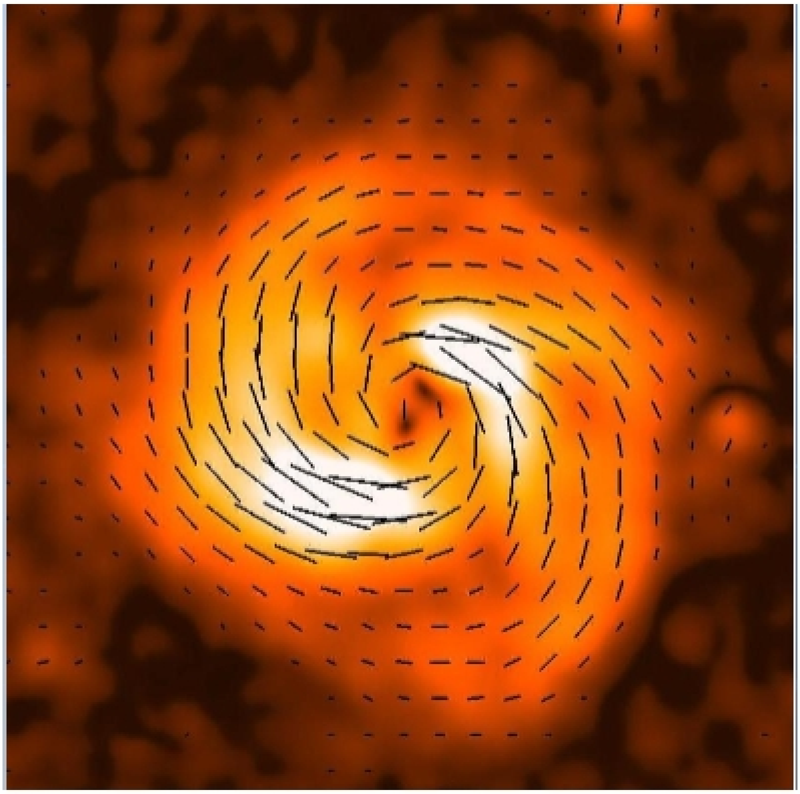

Figure 3.14: Polarized synchrotron intensity (contours) and magnetic field orientation of the galaxy M51. Courtesy of R. Wielebinski.

seem to coincide with HII regions (Mitra et al., 2003), which would indicate that the field follows the rotation velocity in that region. There are also observations of Faraday screens covering angles of a few minutes of unknown origin (Wielebinski and Mitra, 2003). Finally, nearby protostellar disks may provide a magnetic analogous of the gravitational microlenses, as they define small objects of $\approx 10^3$ AU diameter with azimuthal magnetic fields (Stepinski, 1995) of order tens of mG (Gonçalves et al., 2008). Therefore, we find justified to presume that CMLs may appear at any scales R with different values of B.

We would like to notice as well that the disk-like shape proposed here is the simplest realization of CML, but that other magnetic configurations can provide similar effects on CR trajectories. This is the case, for example, for the filament-like structures observed at (different) large scales (see Fig. 3.16). The field is ordered in a line and a CR entering non parallalel to it would experience deviations qualitatively similar to the ones discussed here.

Although from the previous analysis it is apparent that a nearby source could introduce small and medium scale anisotropies in the CR flux, we do not expect any sources of TeV CRs at distances below 1 pc (which would anyway introduce too large anisotropies). In chapter 5, however, we discuss another more plausible mechanism (also based on CMLs) for the generation of this type of anisotropies. The identification of real observational CML will be very improved when the SKA was fully avalaible.

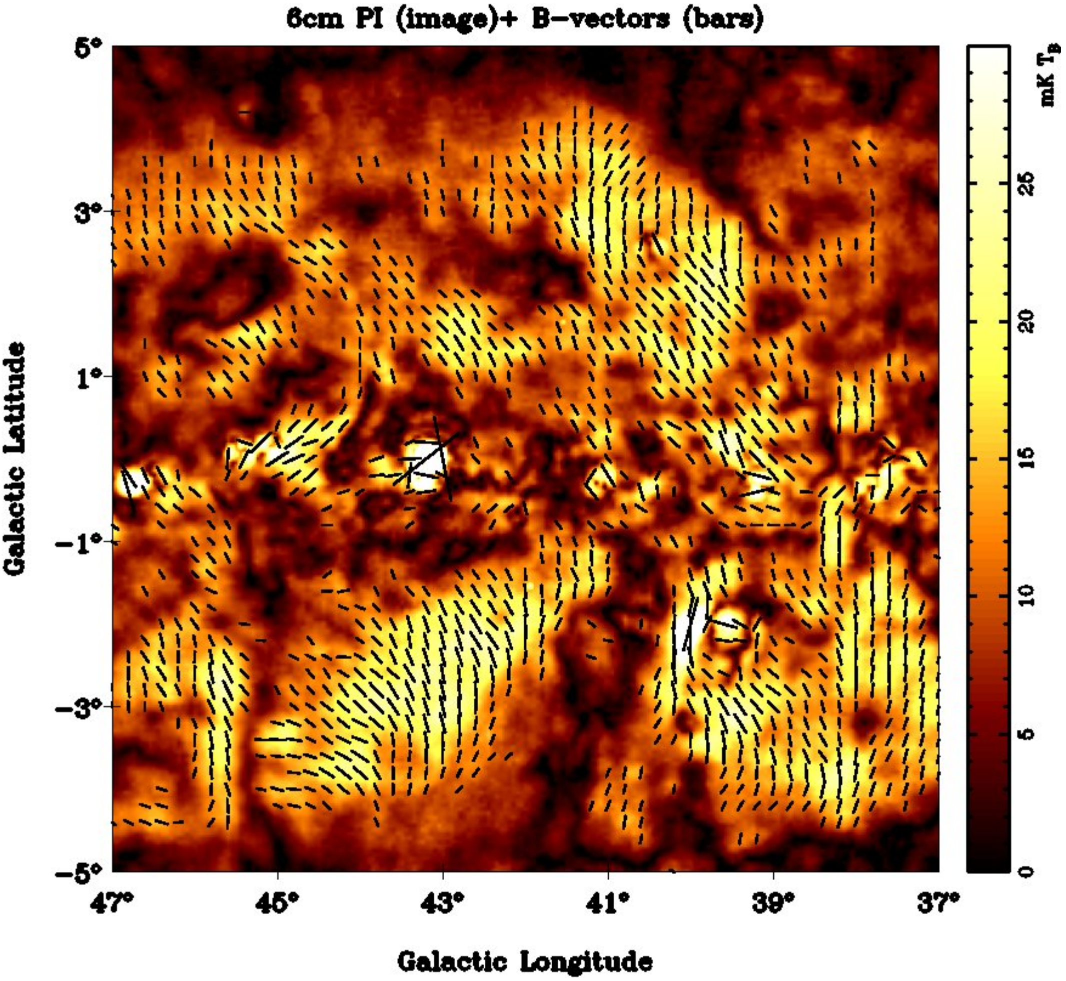

Figure 3.15: Polarized synchrotron intensity (contours) and magnetic field orientation in a zone of the galactic plane. Courtesy from R. Wielebinsky, 2013.

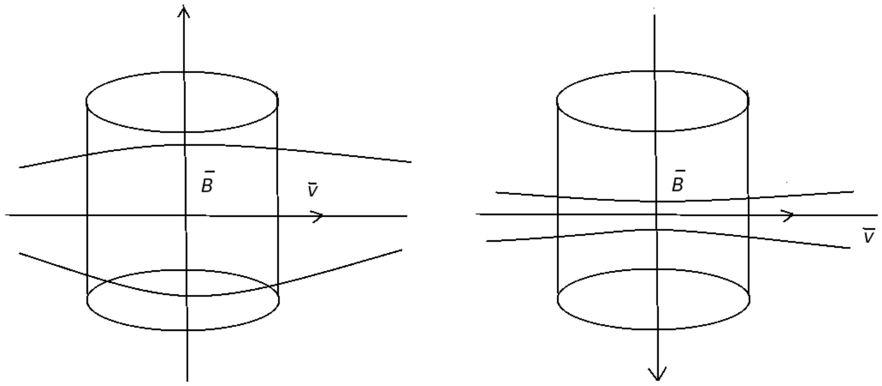

Figure 3.16: Schematic view of filament-like field acting as a CML.

Chapter 4

Cosmic ray transport and Boltzmann formalism

In this chapter we will attempt a novel approach to study the appearence of anisotropies in the CR flux. CR transport is usually described using the diffusion equation for the number density of particles $n(E, \vec{x}, t)$. Anisotropies are then associated to spatial variations of $n(E, \vec{x}, t)$, in particular, since particles diffuse from the higher to the lower density regions, one expects a dipole anisotropy along the gradient of this function. Here, however, we will be interested in the distribution function $f(\vec{x}, \vec{p}, t)$ determined by Boltzmann equation. $f(\vec{x}, \vec{p}, t)$ expresses the number density of particles at $\vec{x}$ with momentum $\vec{p}$, so CR anisotropies can be deduced just by reading its dependence on $\vec{p}$. Although Boltzmann equation implies the diffusion equation once momenta have been integrated, it may also describe effects that are not diffusive without any lose of information. Using simplifying assumptions, we will investigate the consistency of Boltzmann equation to study CR observed anisotropies in the presence of magnetic fields.

4.1 Distribution function, diffusion equation, and Liouville theorem

The distribution function in 6-D phase space is defined

$$\mathrm{d}N = f(\vec{x}, \vec{p}; t)\, \mathrm{d}\tau_x \mathrm{d}\tau_p \tag{4.1}$$

where $\mathrm{d}N$ is the number of particles at time t in the volume element $\mathrm{d}\tau_x \mathrm{d}\tau_p$. $f = \mathrm{d}N/\mathrm{d}\tau_x \mathrm{d}\tau_p$ is then the number density of particles in this 6-D space. The number density of particles at $\vec{x}$, $n(\vec{x}; t)$, is related to the distribution function by

$$n(\vec{x}) = \int f(\vec{x}, \vec{p})\, d\tau_p \tag{4.2}$$

The diffusion equation can be used for the macroscopic description of a fluid flow. The motion of any small volume element of the fluid will be the superposition of individual atomic motions, which may be quite random. This is the case, for example, for thermal motions and also for the trajectories of CRs in the presence of turbulent magnetic fields. The difusion equation will satisfy continuity in ordinary physical space. Consider a small closed surface fixed at $\vec{x} = (x, y, z)$. If particles are streaming through the region with a mean velocity $\vec{v}(\vec{x})$, some of them will enter or exit the volume V enclosed by the surface. The total number of particles within the volume is

$$N = \int_V n\, d\tau_x \tag{4.3}$$

The net flux of particles passing outward through the surface element $d\vec{S}$ at any given position is the scalar product $n\vec{v}_b \cdot d\vec{S}$. Integration of this quantity over the entire surface yields the total rate at which particles cross the surface in the outward direction and, in absence of sinks and sources, the negative rate of change in the number N of particles within the volume:

$$\frac{\partial N}{\partial t} = -\oint_S n\,\vec{v_b}\cdot d\vec{S} \tag{4.4}$$

This continuity equation can be written in differential form using of Gauss's theorem:

$$\int_V \frac{\partial n(\vec{x})}{\partial t} d\tau_x = -\int_V \nabla\cdot(n(\vec{x})\,\vec{v})d\tau_x\,, \tag{4.5}$$

which implies

$$\frac{\partial n(\vec{x})}{\partial t} = -\nabla\cdot[n(\vec{x})\,\vec{v}]\,. \tag{4.6}$$

Since we assume that the number of particles is conserved, the particle density at any point in space can increase only if there is a net flux entering the differential region, i.e., if the divergence is negative. This can occur, for example, as a high-density bubble of particles flows into a region of space.

The distribution function $f(\vec{x},\vec{p};t)$ will obey a similar continuity equation, but in 6-D instead of just 3-D. Notice that the spatial coordinates verify $d\vec{x}/dt = \vec{v}$, which has defined the flux through $d\vec{S}$. Analogously, if there is a net force $\vec{F}$ acting on the particles the momentum will verify $d\vec{p}/dt = \vec{F}$, which will define the flux through a closed surface in momentum space. In terms of the 6-D divergence the continuity equation reads

$$\frac{\partial f}{\partial t} = -\nabla_x\cdot(f\,\vec{v}) - \nabla_p\cdot(f\,\vec{F})\,. \tag{4.7}$$

Expanding the equation above and assuming $\nabla_p\cdot\vec{F} = 0$ we obtain the simplest version of Boltzmann equation, with no sources, collisions nor energy loss:

$$\frac{\partial f}{\partial t} = -\vec{v}\cdot\nabla f - \vec{F}\cdot\nabla_p f\,, \tag{4.8}$$

where we have dropped the subscript in the spatial gradient. It is easy to see that when we measure the CR differential flux $F(E, \vec{u}; t)$ (number of particles crossing the unit area from a given direction $\vec{u}(\theta, \phi)$ per unit solid angle, energy and time) we can directly *read* the distribution function:

$$f(\vec{r}_{Earth}, -\frac{E}{c}\vec{u}; t) = \frac{c^2}{E^2}\, F(E, \vec{u}; t)\,, \tag{4.9}$$

where we have used the relativistic limit with $E = cp$. In next section we will use this equation to study the appearance of non-diffusive effects in the CR flux.

Liouville theorem is a particular expression that can be derived from Boltzmann equation. We can write it as

$$\frac{\partial f}{\partial t} + \sum_i \frac{\partial f}{\partial x_i}\frac{dx_i}{dt} + \sum_i \frac{\partial f}{\partial p_i}\frac{dp_i}{dt} = 0\,. \tag{4.10}$$

One can recognize the left side of the equation as the total derivative df/dt, which would be a measure of the density of representative points in phase space as one follows a trajectory through phase space. This derivative equal zero tells us the Liouville theorem: the phase-space density is conserved as one follows the flow or

$$\frac{df}{dt} = 0\,. \tag{4.11}$$

The conditions for the validity of this statement are that the forces are p-divergent free, $\nabla_p \vec{F} = 0$, and differentiable (e.g. no collisions), as it happens for magnetic forces. Up to collision or radiation processes, these conditions are met by galactic CRs spiraling around the interstellar magnetic field lines or by solar particles streaming into the Earth's magnetic field.

For completeness, we will briefly discuss the (isotropic) diffusion equation including all possible terms (Blasi and Amato, 2012):

$$\frac{\partial n_i}{\partial t} = \nabla\cdot(\kappa_i \nabla n_i) + Q_i - \frac{\partial}{\partial E}(b_i n_i) - \nabla\cdot(\vec{u}\, n_i) - \frac{n_i}{\pi_i} + \sum_{j>i} \frac{P_{ij}}{\pi_j} n_j\,. \quad (4.12)$$

The first term expresses the diffusion, where the coefficient κ_i for particle species i connects the particle current density to the density gradient. The second term, $Q_i(E, \vec{v}; t)$, describes the sources: particles produced at $(E, \vec{v}; t)$ per unit volume, energy and time. It is easy to see that, for a single particle initially at the origin, $Q_i = \delta^3(\vec{x})\delta(t)\delta(E - E_0)$, if the rest of terms are negligible then the solution to the diffusion equation is just the Gaussian

$$n_i(E, \vec{v}, t) = \frac{e^{-\frac{r^2}{4t\kappa_i}}}{8(\pi\kappa_i t)^{3/2}} \delta(E - E_0). \quad (4.13)$$

After a time t the average position $\langle r \rangle$ where one can find the particle is

$$\langle r \rangle = \sqrt{2\kappa_i\, t}. \quad (4.14)$$

In contrast to a *ballistic* regime with $\langle r \rangle \propto t$, in this *Markovian* diffusive regime the distance to the source grows like $\sqrt{t}$. This same result is obtained for a particle that follows a random walk of length $\lambda_i = 3\kappa_i / c$.

The third term, with $b_i(E) = \frac{\partial E_i}{\partial x_i}$, denotes energy loss (by ionization, synchrotron radiation etc.) or energy gain of the species i. The fourth term describes the plasma convection transport, and the fifth one represents the particle loss by colissions with the interstellar medium. The last term gives the production of the species i when a nucleus of higher mass number collides with interstellar baryonic matter.

Diffusion in the presence of magnetic fields is commonly treated in the framework of the quasilinear theory theory (Giacalone and Jokipii, 1999). The field is separated into its average (or *regular*) value plus the random fluctuations,

$$\vec{B} = \vec{B}_r + \delta\vec{B}\,, \tag{4.15}$$

where $\langle\vec{B}\rangle = \vec{B}_r$ and $\langle\delta\vec{B}\rangle = 0$, and it is assumed that the turbulence is small ($\delta\vec{B}0 < \vec{B}_r$). One can then expect an anisotropic propagation with two diffusion coefficients: one describing transport in the direction of $\vec{B}_r$, $\kappa_\parallel$, and another one for the propagation perpendicular to the this field component, $\kappa_\perp$.

The actual spectrum of turbulences $\delta\vec{B}$ in the interstellar medium is currently a matter of debate. It is unclear whether a unique power law (Kolmogorov-like) describes the power spectrum of the magnetic inhomogeneities from ~ 100 pc down to $\sim 10^{-6}$ pc. Since the interaction of a CR with a magnetic turbulence is of resonant nature (i.e., it scatters with inhomogeneities that have a coherence length similar to its Larmor radius, or a wave number $k \approx 1/r_L$), these scales correspond to protons of energy between 1 and 10^8 GeV. The quasilinear regime implies a relation between the two diffusion coefficients:

$$\frac{\kappa_\perp}{\kappa_\parallel} = \frac{1}{1 + (\lambda_\parallel/r_L)^2} \tag{4.16}$$

where $\lambda_\parallel$ (the mean free path in the regular field direction) is much larger than r_L at TeV scales (Casse et al., 2001). As the energy grows, however, the turbulence level becomes order 1 ($\delta B/B_r \approx 1$). In such conditions there is no preferred direction of propagation, and the parallel and perpendicular diffusion coefficients should become similar.

4.2 Dipole anisotropy introduced by the sources

In the quasilinear framework CR propagation is the addition of two main effects. The regular magnetic field *traps* the CR, implying a trajectory close to an helix along $\vec{B}_r \equiv \vec{B}_{IS}$ of radius $r_L\sqrt{1-\mu^2}$ and velocity

$$v_\parallel = c\mu \,, \quad v_\perp = c\sqrt{1-\mu^2}\,, \tag{4.17}$$

where μ is the cosine of the so called pitch angle and

$$r_L = \left(\frac{E}{1\ \mathrm{TeV}}\right)\left(\frac{1\ \mu\mathrm{G}}{B_{IS}}\right)\left(\frac{e}{Q}\right) 1.1\times 10^{-3}\ \mathrm{pc}\,. \tag{4.18}$$

At the same time, the CR will scatter with the magnetic irregularities of wave number $k \approx 1/r_L$. This will introduce random changes in $v_\parallel$ after a mean free path $\lambda_\parallel$ (see Fig. 4.1). Such change will also imply a variation in the field line trapping the CR, *i.e.*, $\lambda_\perp \approx r_L$.

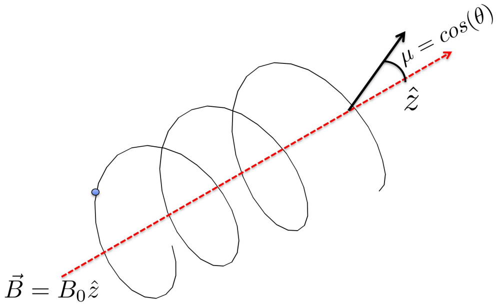

Figure 4.1: Pitch angle μ definition in a regular magnetic field aligned with z axis.

Let us start by considering the simplest flux in a diffusive regime: a CR gas from a pointlike source S that propagates through a turbulent but isotropic medium. Such medium would correspond to the absence of regular interstellar magnetic field $\vec{B}_{IS}$ (or to the presence of a field weaker than the fluctuations $\delta\vec{B}$ of wave number $k \approx 1/r_L$), and it implies the same diffusion coefficient κ in all directions. The trajectories will define in this case a three-dimensional random walk of step $\lambda = 3\kappa/c$. The mean displacement D from the source that a particle reaches after a (large) time t is then

$$D = \sqrt{2\kappa t}\,. \tag{4.19}$$

The expression above implies that the radial mean velocity of the gas (the *CR wind*) will decrease like $1/\sqrt{t}$ with the distance D from S:

$$v_{\text{gas}} \approx \sqrt{\frac{2\kappa}{t + 2\kappa/c^2}} = c\left(\frac{c^2D^2}{4\kappa^2} + 1\right)^{-1/2}\,. \tag{4.20}$$

The relative difference between the flux going away or towards the source (the forward-backward asymmetry A^{FB}) can then be estimated as the ratio

$$A^{FB} \approx \frac{v_{\text{gas}}}{c} \approx \frac{2\kappa}{cD}\,. \tag{4.21}$$

This means that the point-like source will introduce an anisotropy in the CR flux proportional to $1/D$ and to λ. Basically, it is a dipole anisotropy with the excess pointing towards S:

$$F(\vec{u}) = F_0\,(1 + \vec{u}\cdot\vec{d})\,, \tag{4.22}$$

where

$$\vec{d} = \frac{A^{FB}}{2\pi}\,\vec{u}_S\,. \tag{4.23}$$

It is worth showing that if the differential flux is the addition of two dipolar anisitropies (produced by two different sources), then the total flux defines *another* dipole. Suppose that the two differential fluxes are

$$F^{(1)}(\vec{u}) = F_0^{(1)}(1+\vec{u}\cdot\vec{d}_1) \tag{4.24}$$

$$F^{(2)}(\vec{u}) = F_0^{(2)}(1+\vec{u}\cdot\vec{d}_2)\,. \tag{4.25}$$

Their addition gives

$$F(\vec{u}) = F^{(1)}(\vec{u}) + F^{(2)}(\vec{u}) = \left(F_0^{(1)} + F_0^{(2)}\right)\left(1+\vec{u}\cdot\frac{F_0^{(1)}\vec{d}_1 + F_0^{(2)}\vec{d}_2}{F_0^{(1)} + F_0^{(2)}}\right)\,. \tag{4.26}$$

In general, when there are several sources S_i the addition of the corresponding dipole anisotropies $\vec{d}_i$ results in a dipole anisotropy $\vec{d}_T$ with

$$\vec{d}_T = \frac{\sum_i F_0^{(i)}\,\vec{d}_i}{\sum_j F_0^{(j)}}\,. \tag{4.27}$$

Summarizing, for an isotropic CR propagation we may expect a dipole anisotropy: a net CR wind coming from the average CR source (Pohl and Eichler, 2013), with its intensity inversely proportional to the distance to these sources and proportional to the mean free path between collisions. In terms of the diffusion equation, the dipole is in the direction of the spatial CR density gradient (Blasi and Amato, 2012) and has an amplitude

$$d = \frac{3D_i}{c}\frac{\nabla n_i}{n_i} \tag{4.28}$$

This dipole-like feature seems to agree with the observations described in the next chapter. However for a realistic distribution of sources (supernova remnants) the anisotropy that one expects would be 13 times larger (Ptuskin et al., 2006) than the one provided by the data, and with a dipole axis along the *wrong* direction (Strong et al., 2007). Most important, ∇n and the amplitude of the anisotropy should increse at higher energies, whereas the observations indicate a weakening of the large scale CR anisotropy when one moves from TeV to PeV energies.

4.2.1 Compton-Getting effect

The original Compton-Getting effect (Compton and Getting, 1935) is caused by the motion of the Solar System around the galactic center. If CRs are at rest (*i.e.*, a null mean velocity) in the galactic frame, this will induce a CR wind that translates into a dipole with a maximum in the direction of motion. For no co-rotation of the CR plasma with the Galaxy, given our $\approx$ 220 km/s speed the magnitude of the anisotropy is calculated at $v/c \approx 0.1\%$, while at the other extreme of full co-rotation the anisotropy would be zero.

No evidence of a galactic anisotropy from the direction suggested by the Compton-Getting effect has been detected (see Chapter 5). For no co-rotation, the dipole should have a maximum at r.a. = 315°, dec. = 48° and a minimum at r.a. = 135°, dec. = 48°. Most important, this effect should be energy-independent, while the large-scale anistropy detected by several observatories changes from TeV to PeV CR energies. Therefore, the observed under study in this thesis is not dominated by the galactic Compton-Getting effect, although a small contribution cannot be ruled out (Biermann et al., 2013).

4.3 Anisotropies consistent with Boltzmann equation

We will then explore a different approach based on Boltzmann equation to describe the CR anisotropy. Our main motivation is to obtain a framework that includes the effects of the (local) magnetic fields.

Notice, however, that a turbulent magnetic field may be considered *regular* at distances smaller than its radius of coherence but random at larger scales. For example, at distances of order $R_\oplus$ the field created by the Earth can be considered regular, whereas for a particle moving through the Solar System it becomes just an irregularity, since the effect of the heliospheric magnetic field will be more important: although the Parker field is weaker, its region of coherence is larger and the total deflection that it produces in the trajectory of a charged particle will be larger. It turns out that for TeV CRs the dominant effect is produced by the local interstellar magnetic field, $\vec{B}_{IS}$. This field has a region of coherence that could be estimated between 0.1 and 10 pc, but it is expected to change randomly in neighbouring cells of similar size. At larger scales the regular field is the galactic field discussed in Chapter 2. Our approach will be able to take this into account by *averaging* Boltzmann equation over the relevant scale in each case.

Let us take a local $\vec{B}_{IS}$ coherent over distances $R_{IS} \gg r_L$, together with a turbulence $\delta B < B_{IS}$. We assume that the correlation term is non vanishing that the CRs (protons of energy between 1 and 1000 TeV) only interact with the magnetic fields, neglecting energy loss and collisions with interestellar matter. We will also assume that there are no sources in our vicinity, and that the spatial gradient of the distribution function (the effect discussed in the previous section) gives a subleading contribution. We want to investigate the possibility of a CR wind in our neighborhood with a different origin.

We first separate the local magnetic field $\vec{B}$ and the distribution function $f(\vec{r}_{\text{Earth}}, \vec{p})$ into a regular plus a turbulent component,

$$\begin{array}{rcl} f & \to & \bar{f} + \delta f \,, \\ \vec{B} & \to & \vec{B}_{IS} + \delta \vec{B} \,. \end{array} \tag{4.29}$$

Then we *average* Boltzmann equation over nearby points, with

$$\langle\, \delta\vec{B}\,\rangle = \langle\, \delta f\,\rangle = 0\ . \tag{4.30}$$

As we mentioned before, we take the simplest form of that equation: stationary and homogeneous (zero time and space derivatives) magnetic field $\vec{B}_{IS}$ and distribution function $\bar{f}$. For a fixed CR energy and an average magnetic force $_{\vec{F}}$, $\bar{f}$ must satisfy Boltzmann's equation:

$$\vec{F}\cdot\nabla_u\, \bar{f}(\vec{u}) = e\ (\vec{u}\times\vec{B})\cdot\nabla_u\, \bar{f}(\vec{u}) = 0\ , \tag{4.31}$$

where $\vec{u}=\vec{p}/p$ and $\vec{p}$ is the momentum of the CR. The equation above can also be written

$$\vec{u}\cdot\left(\vec{B}\times\nabla_u\,\bar{f}\right) = 0\ , \tag{4.32}$$

which admits the generic solution

$$\bar{f}(\vec{u}) = \bar{f}(\vec{u}\cdot\vec{u}_B)\,. \tag{4.33}$$

Any stationary and homogeneous solution must then be a function with symmetry around the axis of the magnetic field: $\vec{B}_{IS}$ will *isotropize* the flux in the directions orthogonal to its axis. In particular, these solutions may accommodate a dipole along $\vec{u}_B$,

$$\bar{f}(\vec{u}) = f_0\,\left(1-\vec{u}\cdot\vec{d}\right)\ , \tag{4.34}$$

with

$$\vec{d} = \frac{A^{FB}}{2\pi}\,\vec{u}_B\ . \tag{4.35}$$

This distribution function will define (see Eq. (4.9)) the dipolar flux in (4.22) with $\vec{u}_S \rightarrow \vec{u}_B$ and $F_0 = f_0(E/c)^2$, *i.e.*, it is $\vec{B}_{IS}$ (and not the position of the sources) what fixes the direction of the CR wind.

The (forward or backward) direction along $\vec{B}_{IS}$ and the intensity of this dipole anisotropy will depend on boundary conditions that, in

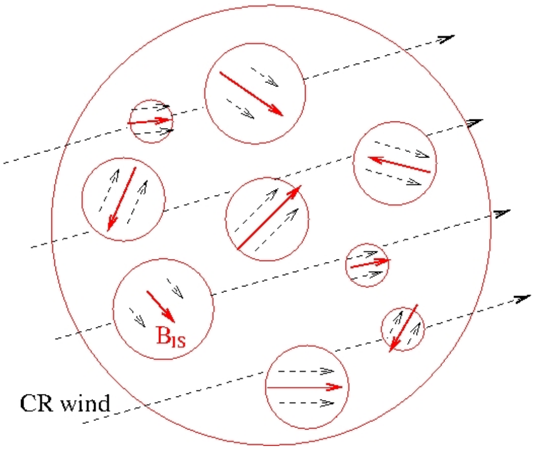

Figure 4.2: $\vec{B}_{IS}$ (within coherence cells of 0.1–10 pc) and cosmic ray wind

turn, will reflect the direction of the CR wind at larger scales. In Fig. 4.2 we plot a scheme of the wind flow within different cells that contain a regular $\vec{B}_{IS}$. This field may change randomly from one cell to another cell, and it is expected to have the average value $\vec{B}_R$ at kpc scales estimated in (Han, 2008). As argued before, the CR anisotropy in each cell will follow the $\vec{B}_{IS}$ magnetic lines, but its forward or backwards direction will depend on the projection of the global wind $\vec{d}_R$ along $\vec{B}_{IS}$. In particular, notice that $\vec{d} \approx 0$ for a $\vec{B}_{IS}$ orthogonal to $\vec{d}_R$.

An important question is then what to expect for the average CR wind. Is it $\vec{d}_R = \langle \vec{d} \rangle$ a dipole along the direction of the average magnetic field $\vec{B}_R = \langle \vec{B}_{IS} \rangle$? To unswer this question we again separate the magnetic field and the distribution function into a regular plus a fluctuating component, but now we average Boltzmann's equation over different (nearby) cells

$$\begin{array}{rcl} f & \rightarrow & f_R + \delta f\,, \\ \vec{B} & \rightarrow & \vec{B}_R + \delta \vec{B}\,. \end{array} \tag{4.36}$$

Although $\delta\vec{B}$ and δf vary randomly from one cell to another, there may be correlations between both turbulent components. We will assume

$$\begin{array}{rcl} \langle\, e\, (\vec{u} \times \delta\vec{B}) \cdot \nabla_u\, \delta f\, \rangle & = & e\, \vec{u} \cdot \langle\, \delta\vec{B} \times \nabla_u\, \delta f \rangle \\ & = & e\, \vec{u} \cdot \vec{T}\,. \end{array} \tag{4.37}$$

Boltzmann equation for the regular components is then

$$\vec{u} \cdot \left(\vec{B}_R \times \nabla_u\, f_R\right) + \vec{u} \cdot \vec{T} = 0\,. \tag{4.38}$$

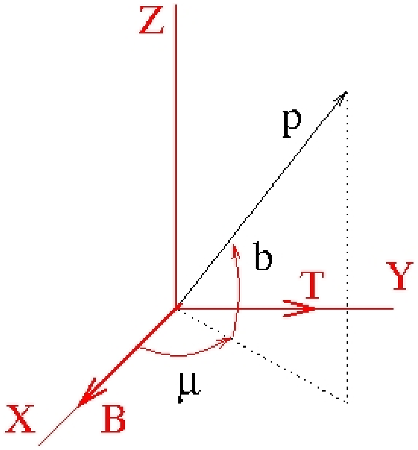

Figure 4.3: Coordinate system.

We can find consistent solutions when the correlation $\vec{T}$ is constant and orthogonal to $\vec{B}_R$. We place the axes (see Fig. 4.3) so that $\vec{B}_R$

and $\vec{T}$ go along the X and the Y axis, respectively, and we use the latitude b and the longitude μ to label the direction $\vec{u}$ of a CR. Taking $f_R(\vec{u}) = f_R(b,\mu)$ and

$$\nabla_u \, f_R = \frac{\partial f_R}{\partial b} \, \vec{u}_b + \frac{1}{\cos b} \, \frac{\partial f_R}{\partial \mu} \, \vec{u}_\mu \tag{4.39}$$

with

$$\vec{u}_b = -\sin b \, \cos\mu \, \vec{u}_\phi - \sin b \, \sin\mu \, \vec{u}_r + \cos b \, \vec{u}_z \; ; \quad \vec{u}_\mu = -\sin\mu \, \vec{u}_\phi + \cos\mu \, \vec{u}_r \; , \tag{4.40}$$

Boltzmann equation becomes

$$-\sin\mu \, \frac{\partial f_R}{\partial b} + \tan b \, \cos\mu \, \frac{\partial f_R}{\partial \mu} + \frac{T}{B_R} \, \cos b \, \sin\mu = 0 \; . \tag{4.41}$$

This equation can be solved analytically:

$$f_R(b,\mu) = f_0 \left(1 + \frac{T}{f_0 B_R} \, \sin b \right) + \tilde{f}(\cos b \, \cos\mu) \; , \tag{4.42}$$

with f_0 a constant and $\tilde{f}$ an arbitrary function of $\cos b \, \cos\mu$. We see that the first term is just a dipole orthogonal to the plane defined by $\vec{B}_R$ and $\vec{T}$, whereas the second term may include a dipole along $\vec{B}_R$:

$$f_R(b,\mu) = f_0 \left(1 + t \, \sin b + s \, \cos b \, \cos\mu \right) \; , \tag{4.43}$$

with $t = T/(f_0 B_R)$ and s a constant depending on boundary conditions. The CR flux that corresponds to this distribution function (see Eq. (4.9)) would be

$$F_R(\vec{u}) = F_0 \, \left(1 + \left(\vec{d}_t + \vec{d}_s \right) \cdot \vec{u} \right) \; , \tag{4.44}$$

where $F_0 = f_0 (E/c)^2$, $\vec{d}_t = -t \, \vec{u}_B \times \vec{u}_T$ and $\vec{d}_s = -s \, \vec{u}_B$. Eq. (4.44) expresses a key result: the global CR wind $\vec{d}_R$ does not necessarily flow along the average magnetic field $\vec{B}_R$. There may appear a second dipole anisotropy orthogonal to $\vec{B}_R$ that, added to the first dipole, could favor any direction: $\vec{d}_R = \vec{d}_t + \vec{d}_s$. Moreover, the turbulent correlation $\vec{T}$ defining this second dipole may evolve with the energy and vary its direction, which would translate into a change in the global CR wind and then in the boundary conditions that determine the dipole anistropy along $\vec{B}_{IS}$. In the next chapter we will discuss how our framework fits the data on the CR anisotropies.

Chapter 5

Interpretation of the data

At energies above 1 TeV CRs can not be observed directly in satellite experiments, as their fluxes are too weak. They are seen after they enter the atmosphere and develop extensive air showers that are observed at the ground. In this chapter we will start with a general description of air showers, then we will review very briefly the different experiments that measure the CR flux, and we will describe the data on the CR anisotropy that we would like to interpret. Finally, we will fit the observations and will discuss the possibility that future observations confirm our hypotheses.

5.1 Extensive air showers

When CRs arrive to the Earth they interact inelastically with nuclei in the atmosphere and produce secondary hadrons. In these collisions electroweak processes or strong processes of large q^2 can be neglected, since their frequency is much lower than the soft (diffractive and non-diffractive) processes described by QCD. Therefore, after one collision the typical result is a *leading hadron* carrying $\approx 20\%$ of the initial energy plus a multiplicity of pions and kaons that share the rest of the energy. Notice that any hadronic resonance produced in the collision is *included* through the spectrum of pions and kaons that results from their instant decay.

At energies above ≈ 50 GeV the secondary mesons have a long lifetime and a decay length larger than their interaction length in air, so they will collide with an air nucleus and produce more hadrons. The exception is the π^0, that prefers to decay electromagnetically (with a very short lifetime) into two photons. Once produced, photons *feed* the electromagnetic component of the shower: they convert into e^+e^- pairs that, through bremsstrahlung, give more photons of similar energy. After a few hadronic interactions most of the energy of the hadronic component is transferred to the electromagnetic part of the shower. The kaons and charged pions produced with an energy below 50 GeV, in turn, will decay giving mostly muons and neutrinos, that propagate through the atmosphere and hit the ground. A scheme of the different shower components is shown in Fig. 5.1.

Particle multiplication and ionization energy losses are competing processes. When particles reach a critical energy, ionization losses start to dominate and the shower is gradually absorbed. Let us discuss in some more detail the longitudinal development of the shower.

5.1.1 Heitler's model for an electromagnetic shower

The basic properties of the development of the cascade can be extracted from a simple model due to Heitler, describing the evolution of purely electromagnetic cascades. Each generation of the hadronic cascade converts about 30% of its energy into the electromagnetic component (photons). The rapidly growing number of electrons and positrons makes them the most numerous species in the shower, and eventually they lose about 90% of the total shower energy to ioniza-

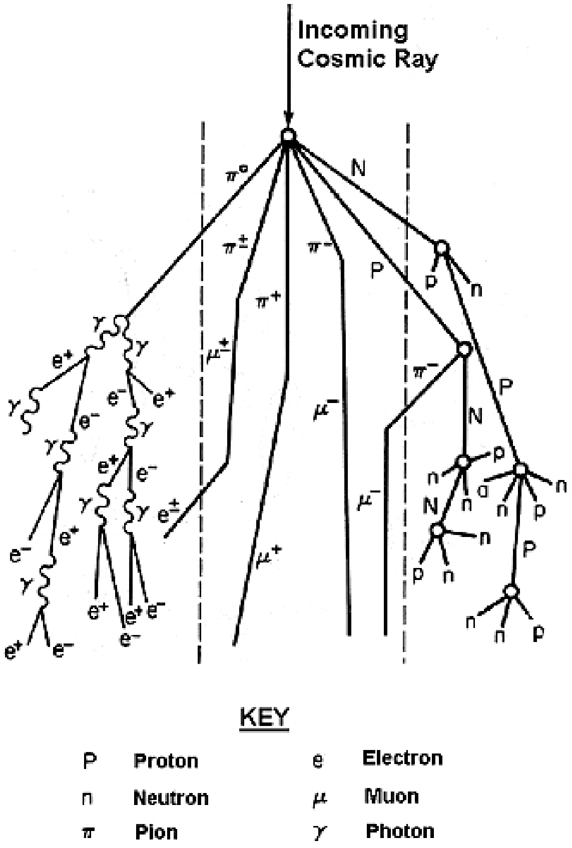

Figure 5.1: Nucleonic, pionic and electromagnetic components in CR extensive air shower.

tion. The energy deposited into the atmosphere through ionization by muons is much smaller. The remaining 10% of the total shower energy is *missing energy* deposited in the ground in the form of muons and neutrinos and also energy lost in nuclear excitations.

Heitler's model (Bhabha and Heitler, 1937) for electromagnetic cascades illustrates some basic features of the development of air showers. Each line can be interpreted as a shower particle, which after one collision transfers half of its energy to a new particle (a new branch in the model). The average distance between interactions is denoted by λ. When the cascade has passed through an atmospheric depth X along its axis, the number of particles is given by $N(X) = 2^{X/\lambda}$, and the average energy of each particle is $E(X) = E_0/N(X)$, beig E_0 the energy of the primary particle.

The splitting process continues until the particles reach a critical energy E_c, in the case of electrons and positrons, when ionization losses dominate. The shower reaches its maximum particle number at this energy. The corresponding atmospheric slant depth is called the shower maximum or X_{max}. The number of particles at X_{max} is called N_{max} and is estimated by:

$$N_{max} = N(X_{max}) = E_0/E_c\,, \tag{5.1}$$

with

$$X_{max} \propto \lambda \cdot \log(E_0/E_c) \tag{5.2}$$

This gives two basic features of high energy electromagnetic cascades: $N_{max} \propto E_0$ and $X_{max} \propto \log(E_0)$.

These relations between the energy of the primary particle and the shower profile are also valid for hadronic air showers. The effect of the chemical composition on the profile of the air shower can then be estimated assuming "superposition": a nucleus of mass number A and energy E_0 can be approximated by A independent nucleons, each one of energy E_0/A. The A nucleons are then assumed to interact independently with the atmosphere, resulting in the superposition of A sub-showers. This leads to the same N_{max} for the total shower of a nucleus or a proton of equal energy, but a higher possition of this maximum:

$$X_{max} \propto \lambda \cdot \log[(E_0/(A \cdot E_c)] \, . \tag{5.3}$$

Heavier nuclei initiate showers that develop higher up in the atmosphere compared to showers from light nuclei or nucleons.

5.1.2 Hadronic showers

The model developed by Heitler can be adapted to describe the showers initiated by hadrons. The relevant parameters are now the hadronic interaction length, λ_I, and the pion critical energy, E_c^π. λ_I is not constant, but it does not depend strongly on energy. The critical energy is the energy at which the decay length of a charged pion becomes smaller than the distance to the next interaction point, approximately $E_c^\pi = 50$ GeV (Matthews, 2005). When the energy of individual charged pions falls below E_c^π they are assumed to decay, producing muons and neutrinos. After each step of thickness $d = \lambda_I$ the hadron interacts, producing N_{ch} charged pions and $\frac{1}{2}N_{ch}$ neutral ones. The average multiplicity in πN interactions increases slowly with energy, and a constant value of $N_{ch} = 15$ is usually adopted for energies around 100 GeV. Neutral pions decay to electromagnetic particles on the spot, initiating EM showers. Charged pions interact, producing a new generation of charged and neutral pions. After n interactions the total number of charged pions is $N_{\pi^\pm} = (N_{ch})^n$. The total energy carried by these pions is $(2/3)^n E_0$, assuming that energy is shared evenly between charged and neutral pions during particle production. The energy per charged pion in the n^{th} interaction layer is then $E_\pi = E_0 \cdot (2/(3N_{ch}))^n$.

After a certain number n_c of generations, E_π falls below E_c^π, with

$$E_\pi = \frac{E_0}{(\frac{3}{2}N_{ch})^n} \ , \quad E_c^\pi = \frac{E_0}{(\frac{3}{2}N_{ch})^{n_c}} \tag{5.4}$$

The number of interactions needed to reach E_c^π is then

$$n_c = \frac{\ln(E_0/E_c^\pi)}{\ln(3N_{ch}/2)} \tag{5.5}$$

To obtain the number of muons in the shower one assumes that all charged pions decay to muons when they fall below their critical energy:

$$N_\mu = (N_{ch})^{n_c} \tag{5.6}$$

combining both sets of equations we obtain

$$\ln N_\mu = n_c \ln N_{ch} = \ln\left(\frac{E_0}{E_c^\pi}\right) \cdot \frac{\ln N_{ch}}{\ln(3N_{ch}/2)} = \beta \ln\left(\frac{E_0}{E_c^\pi}\right) \ , \tag{5.7}$$

where β depends on the multiplicity. In contrast to electrons, the number of muons does not grow linearly with energy:

$$N_\mu = \left(\frac{E_0}{E_c^\pi}\right)^\beta \ . \tag{5.8}$$

The definition of X_{max} for showers initiated by hadrons is the same: the depth at which the electrons and photons of the air shower reach their maximum number. An estimate, however, requires a more sofisticated treatment or a numerical simulation.

5.2 Detection Techniques

5.2.1 Ground arrays

Ground arrays employ scintillation counters or water Cherenkov detectors to sample the lateral density profile of charged particles from

EAS on the ground. The pattern of observed densities is used to determine the location of the shower core, and the geometry of the shower axis is derived from differences in the arrival times of particles to different detectors. The lateral distribution function is compared to model calculations, which provides an estimate of the energy of the primary CR.

Among the ground arrays that observed EAS at ultra-high energies are Volcano Ranch in New Mexico (1959), and later Haverah Park in England (1962), the Yakutsk array in Siberia, the Sydney University Giant Air-Shower Recorder (SUGAR) in Australia and the Akeno array in Japan. The Volcano Ranch array covered an area of almost 10 km^2 with plastic scintillation counters of about 3 m^2 spaced about 1 km apart. It was the first experiment to detect a CR whose energy was estimated at 10^{11} GeV.

The Haverah Park array (Thimann and Bonner Jr, 1948) consisted of water Cherenkov detectors deployed over an area of about 12 km^2 . The spectrum measured by this experiment between 3×10^{17} and 1×10^{19} eV.

The Yakutsk array made use of three different types of detectors: scintillation detectors and muon counters measured the lateral profile of charged particles and muons; an array of photo-multiplier tubes (PMTs) observed the lateral distribution of Cherenkov photons from the EAS. The array covered 10 km^2 in 1974 and was re-arranged to 18 km^2 in 1995. Yakutsk measured the "knee" at about $3 \cdot 10^6$ GeV and the "ankle" at around 10^{10} GeV.

The Akeno array (Nagano et al., 1984) covered about 20 km^2. The Akeno Giant Air Shower Array (AGASA) later extended their area to 100 km^2.

5.2.2 Air fluorescence detectors

Air fluorescence detectors observe the longitudinal development of the air shower in the atmosphere. UV fluorescence light from excited nitrogen molecules in the shower path is collected in mirrors on the ground and projected. Surface detectors collect information on the lateral shower profile at a certain point in the shower development, whereas fluorescence detectors observe the whole development of the shower in the air. The atmosphere is used as a calorimeter in which about 90% of the CR energy is deposited. The measured flux of fluorescence photons is directly proportional to this energy deposit. Observing the longitudinal shower profile also has the advantage that one can determine X_{max} of the shower directly and infer the CR composition.

A Cornell experiment was the first to use this new technique in 1964. However, this attempt to measure fluorescence light from EAS was unsuccessful. The first detection was achieved in 1968 in an experiment near Tokyo, and it could be verified in 1976 with optical detectors in coincidence with the Volcano Ranch array. Fly's Eye experiment (Bird et al., 1994), the predecessor of HiRes, successfully employed the air fluorescence technique to measure the CR flux. Fly's Eye started taking data in 1982. Like HiRes, this experiment already consisted of two fluorescence detectors that allowed stereoscopic observation of EAS.

5.2.3 Other techniques

Scattering of the Cherenkov photons by the atmosphere allows light detection at large angles. The total Cherenkov light flux at the surface is proportional to the track length of shower electrons above threshold energy and can thus be used to estimate the total shower energy. Cherenkov telescopes like H.E.S.S., HERAS, VERITAS and MAGIC are used to observe air showers generated by gamma rays in the TeV range.

Radio emission from EAS was predicted already in the 1960s and tested by several experiments. The favored theory behind this phenomenon is coherent synchrotron emission from highly relativistic electron positron pairs, which are part of the air shower and gyrate in the earth's magnetic field. The radio signal can be picked up with arrays of antennas. This should in principle allow the detection of air showers of energies starting at about 1 PeV. Real interest in the application of this technique to detect CRs is emerging only now. Some of the first few experiments that investigate this detection method are radio stations as part of the KASCADE ground array, the demonstrative CODALEMA experiment and LOPES, the prototype for the planned LOFAR array.

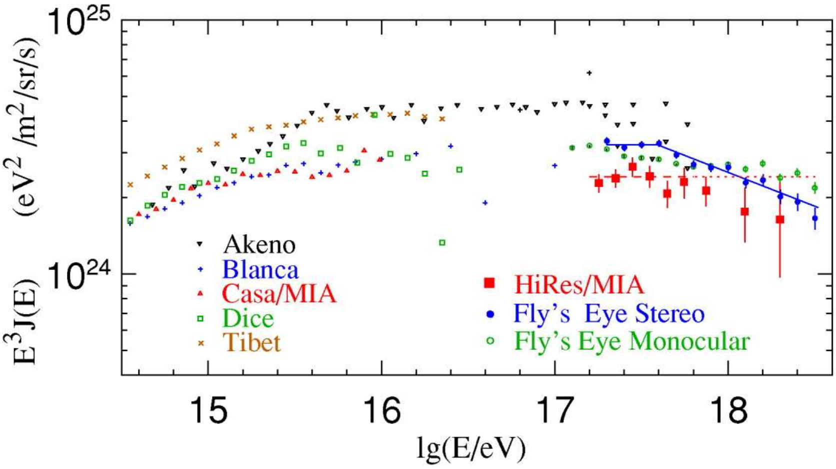

Figure 5.2: CR spectrum from the "knee" to the "second knee".The solid line is a fit to the Fly's Eye stereo spectrum, the dashed and dotted line is a fit to the six lowest energy points of the HiRes/MIA spectrum (Abu-Zayyad et al., 2001).

The combination of different techniques in a single experiment allows for tests of new techniques, but also for complementary measurements of EAS characteristics, such as shower geometry, profile and energy. Simultaneous observation of CR events with ground arrays and Cherenkov detectors, radio antennae or fluorescence detectors provide a more complete description than each method on its own. The HiRes/MIA or the PIERRE AUGER, at higher energies, hybrid detector is an example for the successful combination of the two major techniques in UHECR physics, surface and air fluorescence detectors. Its measurement of the energy spectrum is inclued with others of the commented experiments in Fig. 5.2.

5.3 Observatories

In this section we will introduce the experiments and obervatories that have provided data on the TeV CR anisotropy. They span the northern and southern hemispheres, so in combination they provide a composite map of the whole sky.

5.3.1 Milagro and HAWC

Milagro was the first large-area water-Cherenkov detector specifically built to study extensive air showers. It has been operating between February, 1999 and December, 2008. The detector is located in the mountains of northern New Mexico at an altitude of 2650 m. Milagro was built in a man-made pond formerly used as part of a geothermal energy project. The pond is 60×80 m^2 at the surface and has sloping sides that lead to a 30×50 m^2 bottom at a depth of 8 m. It is filled with purified water and covered by a light-tight high-density polypropylene liner. Milagro consists of two layers of upward pointing 20 cm diameter hemispherical Hamamatsu 10-stage photomultiplier tubes (PMTs).

The top (air-shower) layer of 450 PMTs is located 1.4 m below the water's surface. This layer is used to trigger the detector and measure the arrival time of the air-shower wave front. The second (hadron/-muon) layer consists of 273 PMTs located at a depth of approximately 7 m. The hadron layer is used to make a calorimetric measurement of the shower, to differentiate γ-induced air showers from cosmic-ray induced showers and to detect muons. The increased sensitivity to photons in Milagro provides a substantially lower energy threshold than in previous scintillation arrays.

Figure 5.3: Milagro observatory aerial view.

To determine the direction of the primary ray, Milagro employs the standard technique. After the primary cosmic-ray interacts in the atmosphere and creates an air shower, the secondary particles are all highly relativistic and therefore beamed forward in the direction of the primary. The end result (to a first approximation) is a flat pancake, perpendicular to the incident-ray or cosmic-ray, composed of many thousands of photons, electrons, positrons, and hadrons traveling parallel to the direction of the primary particle. By measuring the relative times that PMTs in the air-shower layer are struck by the Cherenkov radiation, the direction of the primary particle is reconstructed.

HAWC (High Altitude Water Cherenkov) is the continuation of the project. The HAWC site is inside the Parque Nacional Pico de Orizaba, a Mexican national park. It has been constructed on a 200 m×450 m plateau near the saddle between two peaks. The geographical coordinates of the site are approximately ($97.3°W$, $19.0°N$), and the altitude of the plateau is 4100 m. The high altitude of the site means that the detector will be sensitive to gamma rays and protons of energy as low as 100 GeV. The HAWC design will use densely-spaced steel water tanks to observe particles from air showers. Each tank will contain four photomultipliers, and the entire detector will comprise 300 tanks in total. This design represents several improvements over Milagro and will make HAWC 15 times more sensitive than its predecessor even with identical photomultipliers and similar electronics. A comparision between them can be seen in Fig. 5.4

5.3.2 Tibet and ARGO-YBJ

Tibet AS-gamma is a Japanese/Chinese experiment, an air shower observation array built at Yangbajing (4300 m above sea level) in Tibet (China) to observe high-energy CRs. It consists of 697 scintillation counters that are placed at a lattice with 7.5 m spacing and 36 scintillation counters which are placed at a lattice with 15 m spacing.

The time and charge information of each PMT hit by an air shower event is recorded to determine its direction and energy. The low-energy

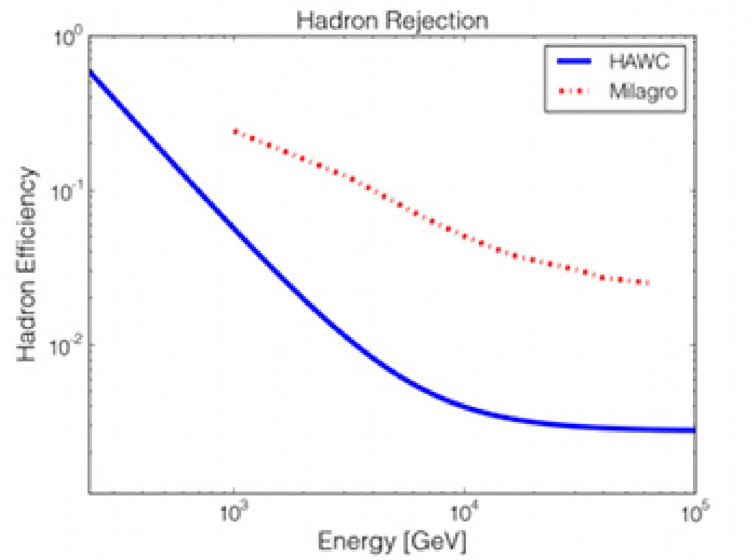

Figure 5.4: Cosmic-ray rejection power of the HAWC detector, with Milagro shown for comparison (Sinnis et al., 2005).

detection threshold is approximately 3 TeV, which is the lowest one achieved by an air shower array in the world. The angular resolution of the air shower array is estimated by the Moon's shadow to be less than 1 degree. At the center of our air shower array, burst detectors and emulsion chambers were set up to closely observe the core region of an air shower event. This total area is 80 m^2. This hybrid experiment enables us to select and measure the proton component in primary CRs in the "knee" region.

Figure 5.5: Argo-YBJ observatory located at Tibet.

In addition, Tibet sets up a solar neutron telescope 9 m^2 in area to detect high energy solar particles accompanied with solar flares at an active phase. The solar activity has an 11-year period, and it was in a very active phase around the year 2000.

Argo-YBJ is a more recent experiment located at the same geographical place. The apparatus consists of a full coverage detector of dimension $(78 \times 74\, m^2)$ realised with a single layer of RPCs (Resistive

Plate Counters). The area surrounding the central detector core, up to $\approx 100 \times 100\mathrm{m}^2$, consists in a guard ring partially ($\approx 30\%$) instrumented with RPCs. Argo-YBJ provides at low cost a large active area and excellent time resolution. It started data taking in 2001.

5.3.3 IceCube and IceTop

IceCube is a neutrino observatory for astrophysics that was installed at the South Pole during Austral Summers between 2004 and 2010. It consists of 5160 optical modules deployed on 86 vertical strings buried 1450 to 2450 meters under the surface of the ice. A surface component called **IceTop** includes an additional 324 DOMs (Digital Optical Modules). Although IceCube was only recently completed, it has been providing data since the completion of the nine string array in 2006. The completed detector will be operated during at least 20 years.

The photomultiplier tubes in IceCube record Cherenkov radiation from charged particle produced by neutrino interactions in the ice. Therefore, IceCube observes the muon and the athmospheric neutrino components in the TeV CR shower. Recent high energy observations can be explined as astrophysical neutrinos that come directly from sources (Collaboration et al., 2013), (Illana et al., 2015). In contrast, the IceTop station, consisting in two ice tanks 10 m apart in the surface, records secondary electrons, photons and muons at see level.

5.3.4 SUPERKAMIOKANDE

The Super-K is located 1,000 m underground in the Mozumi Mine in the Hida's Kamioka area. It consists of a cylindrical stainless steel tank that is 41.4 m tall and 39.3 m in diameter holding 50,000 tons of ultra-pure water. The tank volume is divided by a stainless steelsuper-

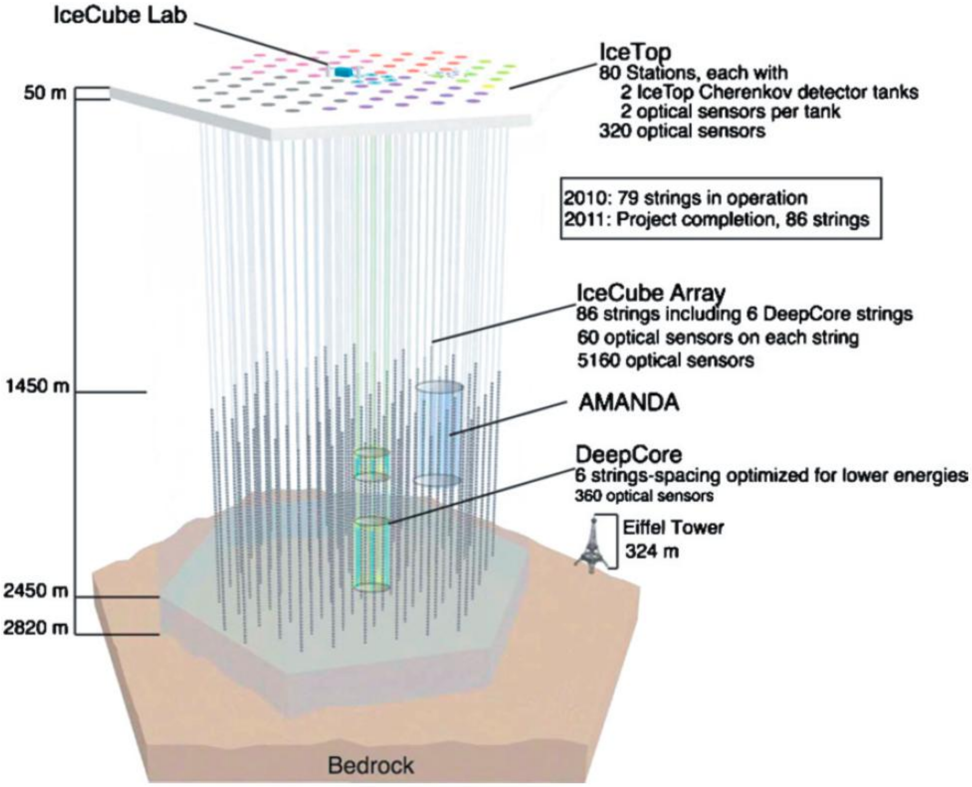

Figure 5.6: IceCube observatory schematic diagram. IceTop is located at the surface (Ahrens et al., 2004).

structure into an inner detector (ID) region that is 33.8 m in diameter and 36.2 m in height and outer detector (OD) which consists of the remaining tank volume. Mounted on the superstructure are 11,146 photomultiplier tubes (PMT) 50 cm in diameter that face the ID and 1,885 20 cm PMTs that face the OD. It started operation in 1996.

The Super-Kamiokande Collaboration announced the first evidence of neutrino oscillations in 1998. This was the first experimental observation supporting the theory that the neutrino has non-zero mass, a possibility that had been speculated about for years. Like IceCube (but targeting lower primary energies), Super-K detects the *invisible* component in the extensive air shower.

Observatory	Years	E. range (GeV)	Ang. res.	Size [m^2]	Height [m]
Milagro	1999/2008	$10^2 - 10^5$	0.5	5000	2630
HAWC	2015/-	$10^3 - 10^5$	0.1	20000	4100
Tibet	1990/-	$5 \cdot 10^1 - 10^3$	0.5	250	4300
Argo-YBJ	2000/-	$10^3 - 5 \cdot 10^5$	0.9	5700	4300
IceCube/Top	2010/-	$10^2 - 10^9$	0.5	50000	-1500
SuperKamiokande	1996/-	$10^3 - 10^5$	0.4	5024	370

5.4 Statistical Analysis

The arrival direction is, together with the energy and the nature of the primary CR, one of the main properties that these experiments try to deduce from the data. The reconstructed direction is affected by several effects. First, there are the experimental circumstances, like the geographical location and the measurement times, that affect the set of recorded CR events: not all the regions in the sky accessible to the experiment are equally exposed to the detector. In addition, CR air showers from different directions (or from the same direction at different times) traverse the Earth's atmosphere with different inclinations.

As a result, showers from certain directions are more likely to remain undetected or be discarded during reconstruction or analysis, which clearly influences the resulting direction distributions. If we discount all these factors, CRs may still reach the Earth with a non-uniform distribution. This is the actual distribution of interest in this Thesis.

5.4.1 Differential flux distributions

In order to describe a differential flux[1] distribution, it is necessary to choose its parametrization as a function of the direction. In this context, directions are specified by equatorial coordinates (dec. δ and r.a. α). The differential flux is generally described by an isotropic component and a direction dependend function representing the anisotropy:

$$F(\delta,\alpha) = F_0(1+\phi(\delta,\alpha)). \tag{5.9}$$

The simplest of such functions is given by the isotropy hypothesis, a constant differential flux from all directions:

$$F_{iso}(\delta,\alpha) = F_0. \tag{5.10}$$

The simplest approach to a large scale variation of the CR differential flux is the assumption of a dipole:

$$F_{dip}(\delta,\alpha) = F_0 \cdot (1+\vec{e_u}(\delta,\alpha)\cdot\vec{d}), \qquad \vec{d} = d\cdot\vec{e_u}(\delta_{dip},\alpha_{dip}), \tag{5.11}$$

with $\vec{d}$ being the dipole vector, defined by its magnitude d and its orientation $(\delta_{dip},\alpha_{dip})$. The right hand side of this equation ranges from $F_0(1-d)$ to $F_0(1+d)$. This dipole description is *assumed* in

---

[1] We recall that by differential flux or intensity we denote the number of particles collected by unit of area, time and solid angle.

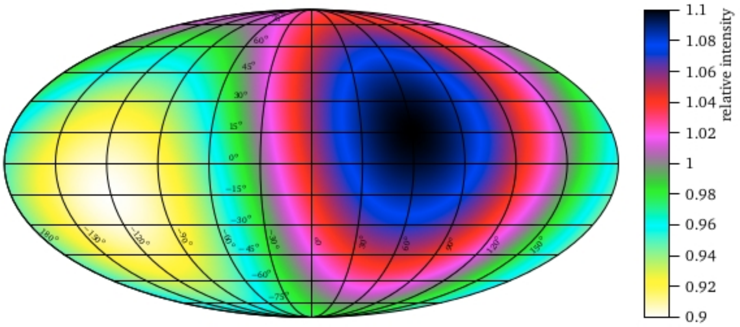

Figure 5.7: Representation of a dipole-like anisotropy using a Mollweide projection in equatorial coordinates. Latitudes are straight horizontal parallel lines, and equal solid angles are represented by equal areas.

diffusion models, and we have obtained it in Chapter 4 using Boltzmann equation. An example dipole distribution is shown in Fig. 5.7, where we have used a Mollweide projection. This is a pseudocylindrical projection in which here the equator is represented by a straight horizontal line perpendicular to a central meridian one-half its length. The other parallels compress near the poles, while the other meridians are equally spaced at the equator. The meridians at 90 degrees east and west form a perfect circle, and the whole earth is depicted in a proportional 2:1 ellipse. The proportion of the area of the ellipse between any given parallel and the equator is the same as the proportion of the area on the globe between that parallel and the equator, but at the expense of shape distortion, which is significant at the perimeter of the ellipse. It is clear that a Mollweide projection can be adapted for any other system of angular coordinates. In particular, it is widely used in galactic and supergalactic coordinates. The projection transforms from latitude and longitude to map coordinates (x, y) via the following equations:

$$\begin{aligned} x &= R\frac{2\sqrt{2}}{\pi}(\lambda - \lambda_0)\cos\theta \\ y &= R\sqrt{2}\sin\theta \end{aligned} \tag{5.12}$$

where R is de the radius of the globe to be projected.

A possible next step towards a more precise description of the differential flux map is to introduce a quadrupole moment, then a sextupole, and so on. By including terms of higher order the number of free parameters increases and the model resembles the recorded data set better and better, eventually leading to a full expansion in spherical harmonics. However, while it is mathematically possible to reproduce the data set precisely with such an expansion, it is questionable whether it yields valuable information on the nature of the anisotropy. The data set itself suffers from experimental inaccuracies and statistical fluctuations, rendering the higher order terms of the expansion meaningless.

5.4.2 Transformation between equatorial and galactic coordinates

The galactic latitude (b) and longitude (l) of a direction can be obatained from its equatorial coordinates (α, δ) using

$$\sin b = \sin\delta \cos i_g - \cos\delta \, \sin(\alpha - \alpha_N) \sin i_g \tag{5.13}$$

$$\cos b \, \cos(l - l_0) = \cos\delta \, \cos(\alpha - \alpha_N) \tag{5.14}$$

$$\cos b \sin(l - l_0) = \sin\delta \sin i_g + \cos(\alpha - \alpha_N) \cos i_g \, , \tag{5.15}$$

where i_g is the angle of the velestial equator from the galactic plane, equal to 62.6°. α_N is the right ascension of the ascending node of the galactic plane (i.e. the line where the galactic plane crosses the celestial equator, heading northwards in the direction of increasing galactic longitude), equal to 282.25°. l_0 is the longitude of the ascending node of the galactic plane, equal to 33°. In Fig. 5.8 we give a plot that can be used to convert one coordinate system into the other.

5.5 Large scale anisotropy at the TeV scale

Let us present the results obtained by the different experiments on the large scale anisotropy at TeV energies. First, we must stress that each obervatory covers either the North or the South sky (HAWC will cover a central zone). Second, not all observatories provide data in separate energy bins, but all of them cover part (or all) of the 1-20 TeV band. At these CR energies we have data from the two galactic hemispheres. From the North we have Milagro, Tibet and SuperKamiokande:

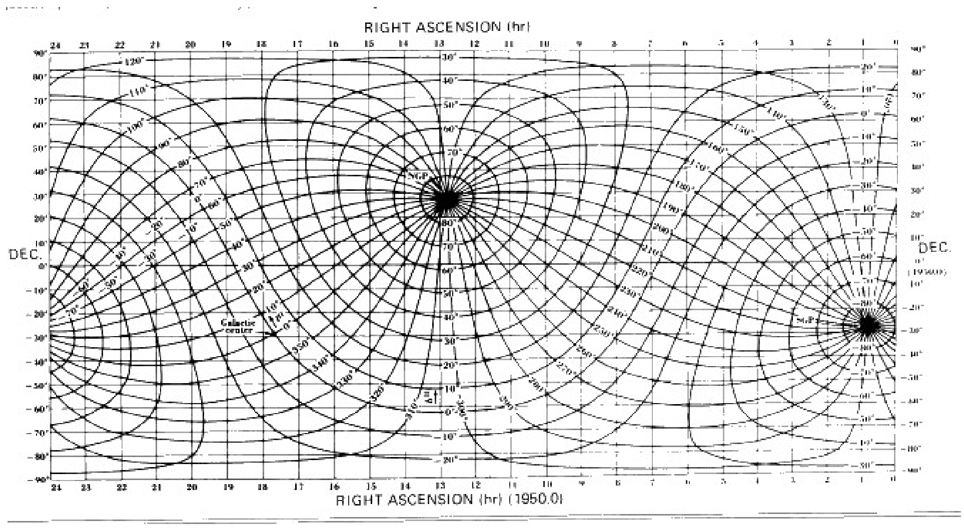

Figure 5.8: Graphic used to convert between galactic and equatorial coordinate systems (Leinert et al., 1997).

- **Argo-Tibet** observatory obtained the skymap of CRs in equatorial coordinates in Fig. 5.9, with data first published them in January 2006 (Amenomori et al., 2006). A 'tail-in' and 'loss-cone' anisotropy components, in their own words (the term dipole-like was first introduced in our study (Battaner et al., 2009)), are seen in their 2D plots in fine detail and with a high accuracy. The excess is located at ≈ 75° r.a. and the deficit at ≈ 200° r.a.

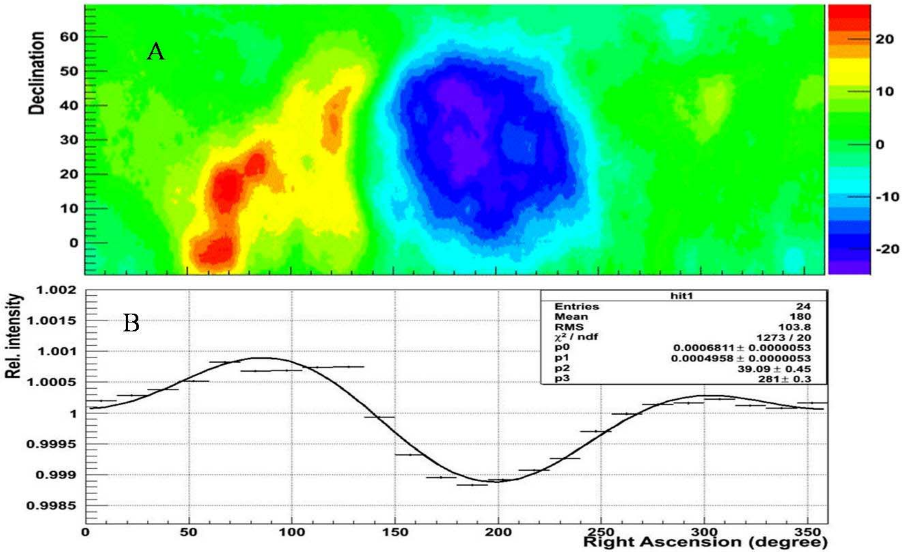

Figure 5.9: Significance representation of the large-scale anisotropy and projection over r.a. obtained by Argo observatory (Cui, 2011).

- **Milagro**: the two regions of interest detected by Tibet-Argo are consistent with Milagro's observations. Milagro saw an anisotropy with a magnitude around 0.1% for CRs with a median energy of 6 TeV. The dominant feature is a deficit region of depth

$(2.49 \pm 0.02\, stat. \pm 0.09\, sys.) \times 10^{-3}$ in the direction of the Galactic North Pole centered at 189^o degrees r.a. (Abdo et al., 2009) (see Fig. 5.10).

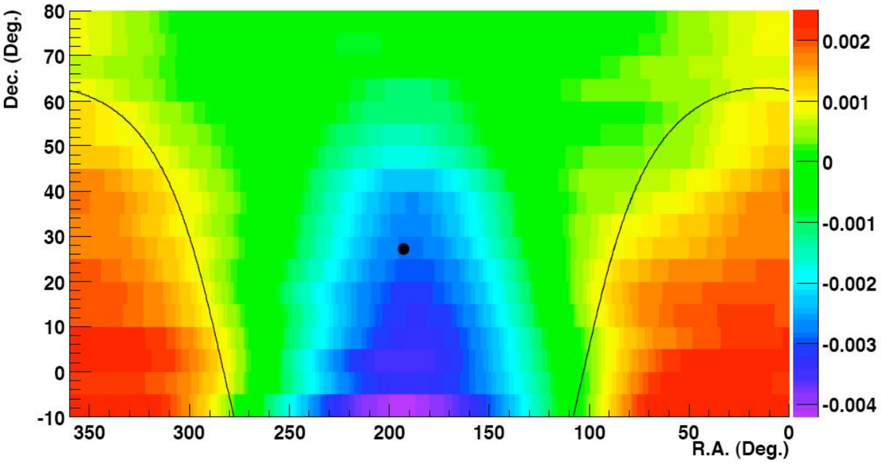

Figure 5.10: Fractional difference of the CR rates from isotropic in equatorial coordinates as viewed by Milagro for the years 2000-2006. The color bin width is $1.0 \cdot 10^{-4}$ reflecting the average measurement error. The median energy is 3 TeV (Abdo et al., 2009)

- **SuperKamiokande** in 2006 provided a Northern hemisphere map where one can also distinguish an anisotropy. They measured the relative variation in the arrival direction of primary CRs of median energy 10 TeV using downward, through-going muons. The projection of the anisotropy map onto the right ascension axis has a first harmonic amplitude of $(6.64 \pm 0.98) \cdot 10^{-4}$ and the maximum has a phase at $(33.2° \pm 8.2°)$ r.a. A sky map indicates (Guillian et al., 2007) an excess of order $(0.104 \pm 0.020)\%$

centered at $(\alpha_T, \delta_T) = (75° \pm 7°, -5° \pm 9°)$ (near the constellation of Taurus) and a deficit region at $(\alpha_V, \delta_V) = (205° \pm 7°, 5° \pm 10°)$, and $(-0.094 \pm 0.014)\%$ (towards Virgo).

While at the South hemisphere we have:

- **IceCube** at the South Pole has also provided data at those energies that seems compatible with the data from north observatories, see Fig. 5.11. The first observation was made with data from 2007 and 2008 that included 4.3 billion muons produced by downward-going CR interactions in the atmosphere. These events were reconstructed with an angular resolution of 3° and a median energy of 20 TeV. The arrival direction distribution exhibits an anisotropy in r.a. with a first-harmonic amplitude of $(6.4 \pm 0.2\,\text{stat.} \pm 0.8\,\text{syst.}) \times 10^{-4}$ (Abbasi et al., 2010). **IceTop** data at 20 TeV, in Fig. 5.12, is compatible with IceCube.

The data is summarized in table 5.1.

5.6 Fitting Milagro's observations

As described before, Milagro published the observation of a TeV large-scale anisotropy in the northern hemisphere (see Fig. 5.13) in 2008. Their data reveals a clear dipole, with a deficit that peaks at $\delta_0 \approx 10^o$ and $AR_0 \approx 190^o$ (*i.e.*, $b_0 \approx 72^o$ and $l_0 \approx 293^o$).

We have shown in the previous chapter that our framework can adjust any anisotropy with axial simmetry around $\vec{B}_{IS}$, in particular, a dipole pointing in the direction of the IS magnetic field. In addition, we have also shown that the global CR flow (see Fig. 4.2) is naturally defined by a direction orthogonal to the large-scale regular field $\vec{B}_R$. This direction depends on a correlation of turbulent quantities that

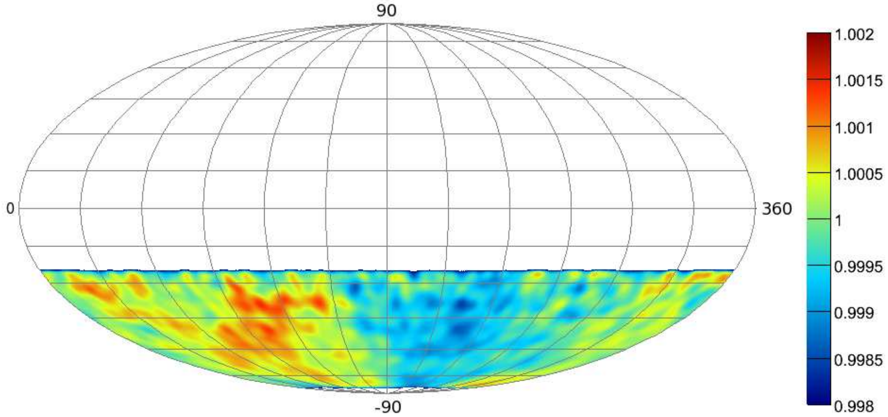

Figure 5.11: The IceCube skymap in equatorial coordinates (Declination (dec) vs. Right Ascension (r.a.)). The color scale is the relative intensity (Abbasi et al., 2010)

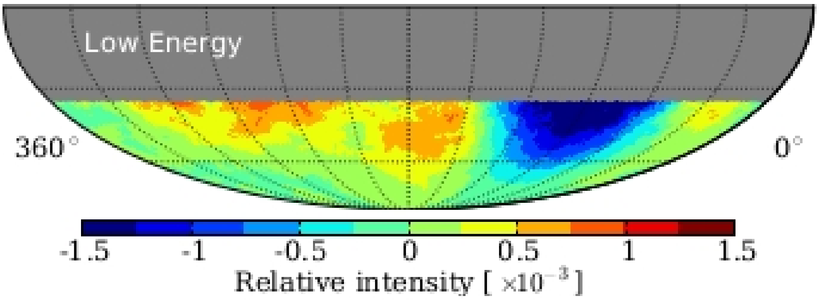

Figure 5.12: The IceTop skymap in equatorial coordinates. The color scale is the relative intensity (Aartsen et al., 2013)

Hemisphere	Experiment	$\langle E \rangle$ [TeV]	Deficit Position		Amplitude
			r.a. [deg]	decl. [deg]	
North	ARGO	3.6	170 to 210	-10 to 30	$3 \cdot 10^{-3}$
	MILAGRO	6	180 to 220	-10 to 0	$3 \cdot 10^{-3}$
	TIBET	6.2	170 to 210	-10 to 20	$3 \cdot 10^{-3}$
	ARGO	24	150 to 190	-10 to 30	$1 \cdot 10^{-3}$
	TIBET	300	-	-	$< 1 \cdot 10^{-3}$
South	ICECUBE	20	190 to 240	-30 to -60	$8 \cdot 10^{-4}$
	ICECUBE	400	40 to 100	-15 to -45	$7 \cdot 10^{-4}$
	ICETOP	400	70 to 110	-15 to -45	$1.6 \cdot 10^{-3}$
	ICETOP	2000	50 to 125	-25 to -55	$3 \cdot 10^{-3}$

Table 5.1: Summary of data on the large scale anisotropy obtained by several observatories: ARGO (Di Sciascio, 2012); MILAGRO (Abdo, 2009); TIBET (Amenomori, 2006); ICECUBE (Abbasi, 2012); ICETOP (Aarsten, 2013).

may change with the energy, but always within a plane orthogonal to $\vec{B}_R$.

Therefore, we would expect a maximum anisotropy if the global CR wind were aligned with $\vec{B}_{IS}$, as it is observed at energies $E \approx 10$ TeV. The dipole anisotropy would indicate in that case simultaneously the axis of $\vec{B}_{IS}$ and a direction in the plane orthogonal to $\vec{B}_R$.

In Fig. 5.14 and Fig. 5.15 we plot our fit of the data for an anisotropy of order 0.3% restricted to a region in the sky accesible to Milagro and for the whole sky, respectively. Our fit provides a good description of Milagro's anisotropy. It implies that CRs move near the Earth with a mean velocity

$$\vec{v}_0/c = -\frac{1}{N}\int \mathrm{d}\Omega\; F(\vec{u})\;\vec{u} = -0.00059\;\vec{u}_\phi - 0.00028\;\vec{u}_r + 0.00157\;\vec{u}_z \tag{5.16}$$

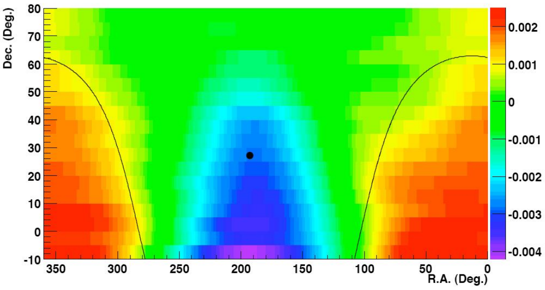

Figure 5.13: Milagro's data (Abdo et al., 2009).

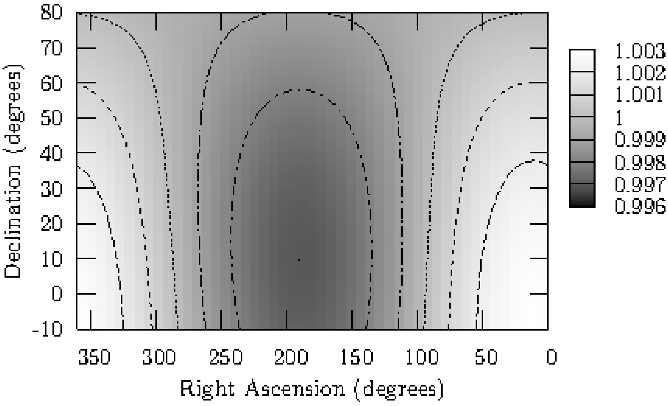

Figure 5.14: Milagro's data fit (Battaner et al., 2009).

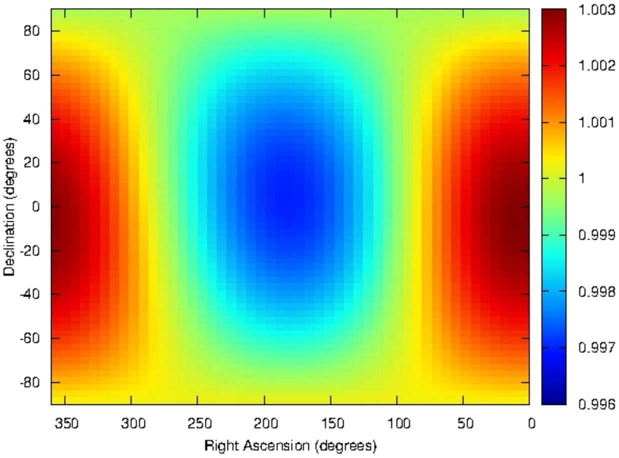

Figure 5.15: Milagro's data fit with our model for the complete sky (Battaner et al., 2009).

where $N = \int \mathrm{d}\Omega\, F(\vec{u})$ and the basis is pictured in Fig. 4.3. Eq. (5.16) expressed the diffusion velocity of the fluid (the transport flux $\vec{J}$ is proportional to $N\vec{v}_0$).

The dipole at Milagro seems to point towards

$$\vec{u}_d = -0.35\,\vec{u}_\phi - 0.16\,\vec{u}_r + 0.92\,\vec{u}_z\ . \tag{5.17}$$

We can check whether this dipole and the local $\vec{B}_R$ are perpendicular. We will consider the values of $\vec{u}_B$ obtained in (Han et al, 1999; Han, 2009): $\vec{B}_R$ basically azimuthal clockwise (a *pitch* of either 0^o or 180^o depending on the definition, which changes for different authors) with also a non null *tilt* angle of 6^o (a vertical component of order 0.3 μG) taking the magnetic field out of the plane. We obtain an unitary vector

$$\vec{u}_B = 0.99\,\vec{u}_\phi + 0.00\,\vec{u}_r + 0.10\,\vec{u}_z\ , \tag{5.18}$$

which implies a remarkable

$$\vec{u}_d \cdot \vec{u}_B = -0.18\ . \tag{5.19}$$

5.7 All-sky compositions. Energy dependence of the anisotropy.

During the past few years new data have been published and a whole sky picture has emerged. Most notably, IceCube/IceTop have provided observations of the Southern sky allowing a composition including the two hemispheres. As can be seen in figure 5.16, this composition seems consistent, defining an anisotropy of the similar intensity and connected deficit and exccess regions. Our framework is consistent with this new picture, and also with the evolution of the anisotropy with the energy suggested by the new observations. Although the higher energies (in the PeV scale) seen by IceTop have not been accessible to the northern hemisphere experiments nor to HAWC yet, the data and our interpretation can be summarized in the following way.

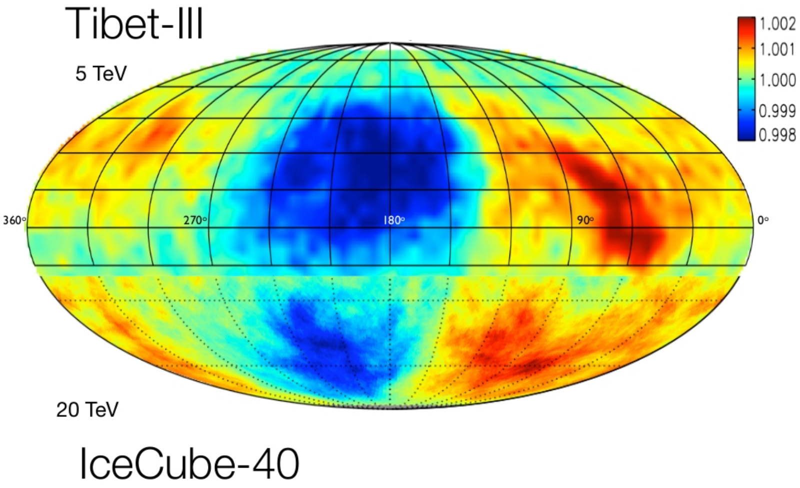

Figure 5.16: All-sky map composition adapted from TIBET and IceCube data.

At 1-20 TeV there is a mostly dipolar anisotropy (see Fig. 5.17) that goes along $\vec{B}_{IS}$. Our best fit is

$$l_B = 180^o\,; \quad b_B = -60^o\,, \tag{5.20}$$

which is consistent with recent data on the local IS magnetic field $\vec{B}_{IS}$. In particular, the spacecraft Voyager (Ratkiewicz and Grygorczuk, 2008) has crossed the heliospheric boundary and provided an "in situ" estimate for the direction of $\vec{B}_{IS}$:

$$l_B = 217^o \pm 14^o\,; \quad b_B = -49^o \pm 8^o\,. \tag{5.21}$$

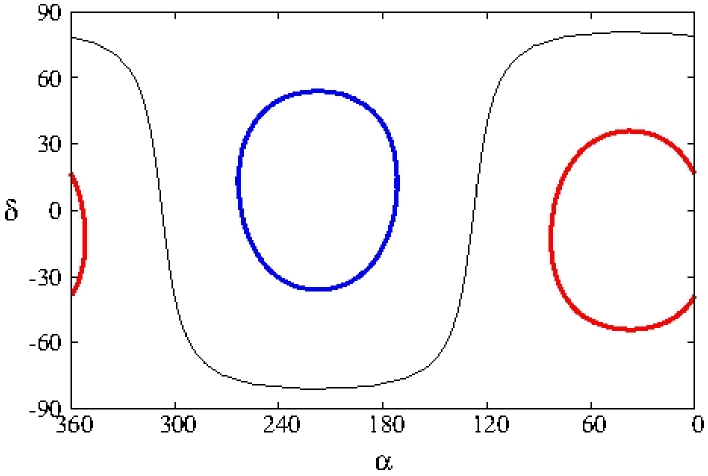

Figure 5.17: Dipole anisotropy along $\vec{B}_{IS}$ for $l_B = 180^o$ and $b_B = -60^o$ in equatorial coordinates (r.a. and dec.). The thin line indicates the magnetic equator, whereas thick lines define cones of angle $\pi/4$ along the magnetic axis.

Additionally, interestellar atom measurements with IBEX (Frisch et al., 2010) imply

$$l_B = 210.5^o \pm 2.6^o\,; \quad b_B = -57.1^o \pm 1.0^o\,. \tag{5.22}$$

Although the region of coherence of such field is unknown (it could vary from 0.01 to 10 pc), it is much larger than the gyroradius of a TeV CR (in Eq. (4.18))

At higher energies the observations from the South Pole indicate that the anisotropy weakens (see Fig. 5.18, becoming of order 10^{-4} at ≈ 100 TeV. Since effects like the movement of the Earth around the Sun or the shadow of the Sun introduce irregularities of the same order, the direction of such small anisotropy is non significant.

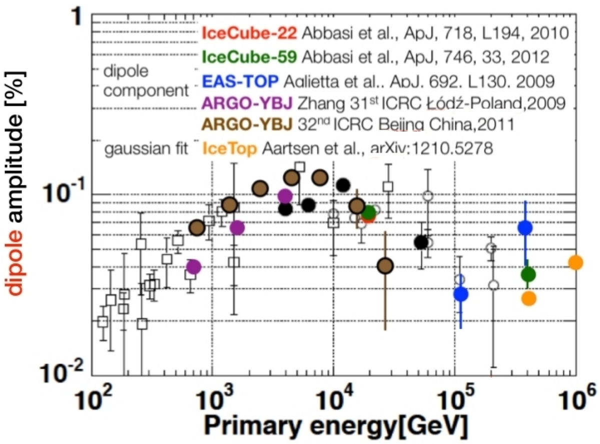

Figure 5.18: Large scale anisotropy amplitude of the dipole fit evolution from TeV to PeV scale with data from severals observatories.

At even higher energies the anisotropy grows again, suggesting a dipole almost opposite to the initial one. Finally, at 2 PeV (Santander et al., 2013) the direction of the dipole may have changed slightly towards the galactic center (see Fig. 5.20). Our simultaneous fit of Milagro and IceCube is given in Fig. 5.17.

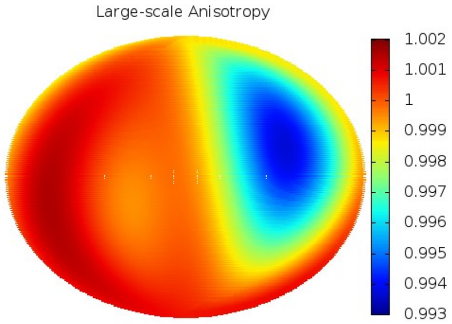

Figure 5.19: Large scale anisotropy for the whole sky using depicted using our model to fit anisotropy at PeV scale.

Our framework provides an interpretation of these observations. Above 1 TeV the effect of the heliosphere on CR trajectories is subleading, and the dominant factor defining the direction of the anisotropy is the local magnetic field $\vec{B}_{IS}$ in Eq. (5.20). At 5–10 TeV the anisotropy is maximal because global wind and $\vec{B}_{IS}$ are approximately aligned. The modulation above 10 TeV can then be explained if the global CR wind varies its direction with the energy, going almost orthogonal to $\vec{B}_{IS}$ at $\approx$ 100 TeV. If the projection of this global wind along $\vec{B}_{IS}$ changes sign, the dipolar anisotropy will be inverted. Finally, the possible missalignment of the dipolar anisotropy with $\vec{B}_{IS}$ at the highest energies would indicate that $r_L \approx R_{IS}$, where R_{IS} is the radius of coherence of the IS magnetic field.

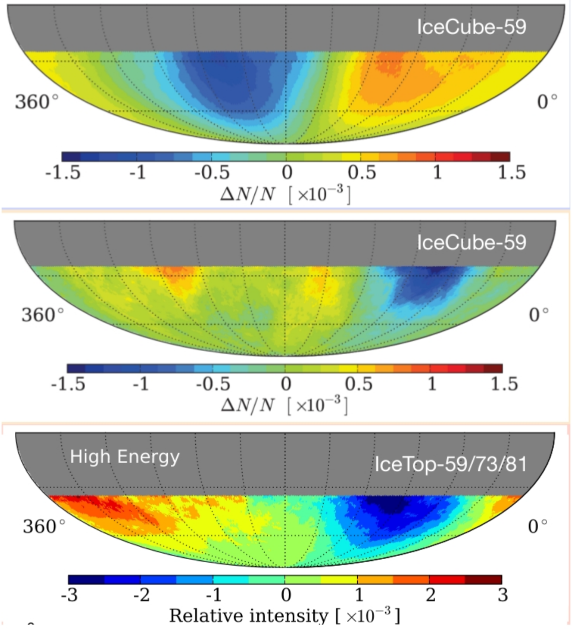

Figure 5.20: Large scale anisotropy evolution from TeV to PeV scale observed by IceCube (Abbasi et al., 2012)

For $B_{IS} \approx 3\ \mu$G we obtain $R_{IS} \approx 0.3$ pc. The propagation becomes then isotropic (see Eq. (4.16)) and the dipole anisotropy should follow the direction of the global wind, not of $\vec{B}_{IS}$.

An important aspect in our description is the change in the phase of the global CR wind with the energy. Buoyance could provide a qualitative explanation for such changes. Turbulent convective cells of magnetic plasma produce a rising motion from the galactic plane. For lower CR energies (i.e., lower Larmor radii) the correlation vector $\vec{T} = \langle \delta\vec{B} \times \delta\nabla_u f \rangle$ would be dominated by eddies that moderately rise over the plane. For larger CR energies, however, the rising eddies reach higher distances from the plane, so that Corioli's forces rotate the direction of the fluctuating magnetic field frozen-in into the interstellar media. A rotation of $\delta\vec{B}$ and of the correlation $\vec{T}$ could then be expected as the CR energy grows.

5.8 Medium and small scale anisotropies

In addition to the large scale anisotropy that we have fitted by a modulated dipole, several observatories have provided skymaps that reveal medium and small scale features in the CR flux. These structures have an approximate angular size that go from ≈ 20° to a few degrees. Observatories that have published this type of anisotropies are **Milagro** (in Fig. 5.21), **Argo** (in Fig. 5.22) and **IceCube** (see Fig. 5.23).

We have argued in Chapter 3 that a possible explanation for these small scale anisotropies is the presence of a CML close to us. In particular, the large scale anisotropy could be focused by a magnetic lense and produce irregularities with similar features. For CMLs inside our galaxy one should in general *subtract* the effect due to the local field at the relevant scale, *i.e.*, the excess does not point directly to the lens. Suppose, for example, that we have a small lens ($D \approx 10^{-3}$

pc) with a strong magnetic field ($B \approx 1$ mG) at a distance below 10 pc from the Earth. If the magnetic field along the trajectory from the lens to the Earth is of order μG (with weaker turbulences at smaller scales) then the effects of the lens on 10^6 GeV CRs can be observed, but from a displaced direction. In any case, the identification of a CML would require a detailed simulation including a full spectrum of magnetic turbulences. For alternative explanations see (Pérez-García et al., 2014) and (Lazarian and Desiati, 2010).

New experiments like the observatory SKA will provide in a few years sufficent angular resolution to identify the inner magnetic field structure of many astrophysical objects. With this new results it will be possible to estimate, for example, the number of low scale irregularities that can be expected.

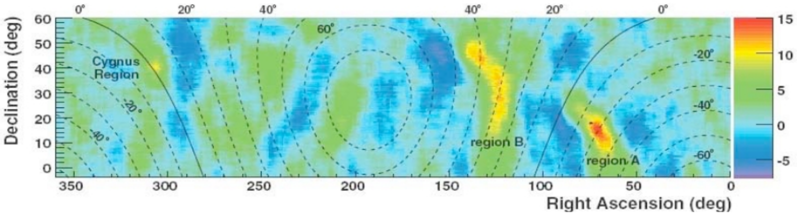

Figure 5.21: Medium scale features after substracting a dipole in Milagro's data (Desiati and Lazarian, 2013).

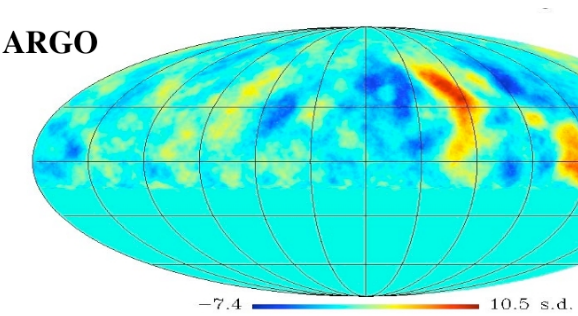

Figure 5.22: Medium scale features after substracting a dipole in Argo's data (Bartoli et al., 2012).

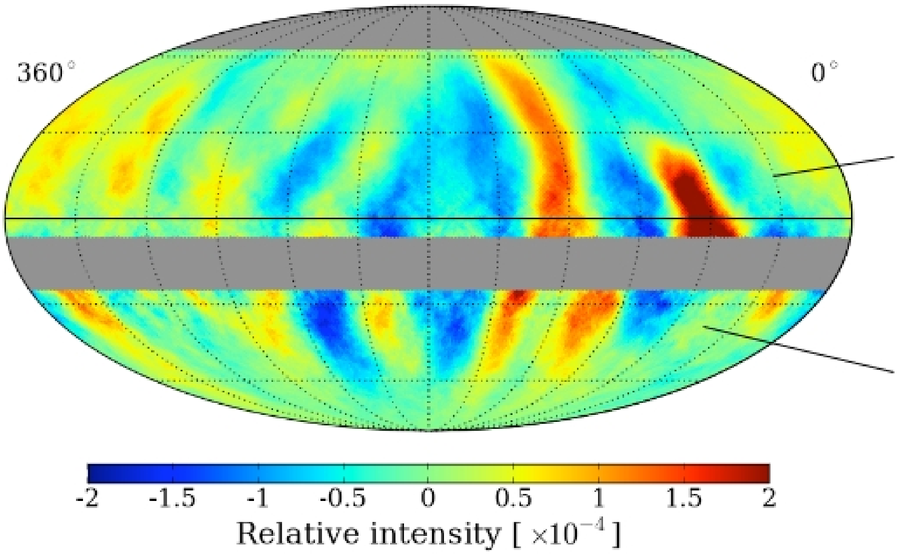

Figure 5.23: Medium scale features after substracting a dipole in IceCube's data (Abbasi et al., 2011).

Conclusions

CR physics is an interdisciplinary field that involves particle physics and astrophysics. In this thesis we have studied the propagation of CRs and the appearence of anisotropies in the differential flux. In particular, we have searched for an explanation of the $O(10^{-3})$ deficit from North galactic directions observed by several experiments (Milagro, TIBET, IceCube). Our approach has been based on Boltzmann equation. We have analized the consistency of this equation with the presence of anisotropies, exploring the possibility that it captures non-diffusive effects. We have obtained a good fit to all the observed data.

We have separated the scales involved in the problem by *averaging* the perturbed Boltzmann equation over different scales. At distances smaller than $R_{IS} \approx 0.3$ pc the insterstellar magnetic field $\vec{B}_{IS}$ is the main force driving the CR wind flow, whereas at galactic scales an interplay between the average field $\vec{B}_R$ and the turbulent fluctuations define a global CR flow orthogonal to $\vec{B}_R$. In our framework this global flow changes with the energy, and its component along $\vec{B}_{IS}$ defines the CR anisotropy that we observe. At energies around 10 TeV both flows are approximately aligned and the anisotropy reaches its maximum value, while at 100 TeV they are almost orthogonal to each other, implying a much weaker anisotropy, and then it grows again but opposite to the initial direction.

Although current data are insuficient to clearly charaterize the anisotropy at higher energies, they suggest a new direction not alligned to $\vec{B}_{IS}$, which would indicate that the Larmor radius of the CRs becomes similar to the region of coherence of the the IS magnetic field, *i.e.*, $R_{IS} \approx r_L \approx 0.3$ pc. Therefore, our results provide both a direction for $\vec{B}_{IS}$ (that agrees with recent observations from Voyager) and an estimate for the size of the local interstellar magnetic plasma (nowadays unknown). These are the two main predictions that result from our model.

We have also argued that this framework has the potential to explain the low-scale anisotropies detected by some observatories (Argo, TIBET, Milagro). These irregularities could appear as the image of the global dipole provided by nearby cosmic magnetic lenses (discussed in Chapter 3), that would focus the CR flow. Notice that the lens acts as a CR source, but that the real source would be the large scale-anisotropy. In particular, if this is $O(0.1\%)$, then the low-scale anisotropy will be of the same order. If the lens is seen from the Earth under a sizeable solid angle, the magnetic field $\vec{B}_{IS}$ can define linear structures similar to the ones described in these experiments. New experiments (such as SKA) may provide enough resolution to clearly identify astrophysical objects with the configuration of a CML.

The simplified scheme proposed here uses a number of approximations: all CRs are protons (heavier nuclei of the same energy would have smaller r_L), all cosmic rays in the same data set have equal energy, or the effect of the heliosphere is negligible. We think, however, that it provides an acceptable qualitative description of the data. In the near future HAWC observations from the northern hemisphere could confirm that the TIBET/Milagro dipole is modulated and changes sign at energies above 100 TeV.

Our results have been published in three articles that we include in the Appendix. As a future work, we would like to use the results in new experiments to identify more clearly the effects of CMLs. In addition, the Sun's magnetic field influence on TeV CRs is a topic that in our opinion deserves a more dedicated study. Given the intense activity in the field of CRs, the future will for sure bring exciting results.

Conclusiones

Los rayos cósmicos constituyen un campo que requiere un enfoque interdisciplinar, con desarrollos de astrofísica y física de partículas. En esta tesis hemos estudiado el efecto de los campos magnéticos en su propagación y en la aparición de anisotropías. En particular, hemos analizado la anisotropia de orden $O(10^{-3})$ en el flujo de rayos cósmicos de energías TeV-PeV observada por varios experimentos (Milagro, TIBET, IceCube). Nuestra metodología está basada en la ecuación de Bolztmann. Hemos investigado la consistencia de esta ecuación con la presencia de anisotropías, explorando la posibilidad de que recoja efectos no difusivos.

Hemos separado las escalas involucradas en el problema promediando la ecuacion de Boltzmann a distintas distancias. A pequeña escala, distancias menores que $R_{IS} \approx 0.3$ pc, la fuerza principal que dirige el viento de rayos cósmicos es el campo magnético interestelar $\vec{B}_{IS}$, mientras que a escala galáctica el efecto combinado del campo regular y sus fluctuaciones turbulentas define una anisotropía ortogonal al campo regular $\vec{B}_R$. En este contexto la intensidad y la dirección del viento cambia con la energía, y su componente a lo largo de $\vec{B}_{IS}$ define la anisotropía que observamos. A energías de 10 TeV ambos efectos estan casi alineados y la anisotropía alcanza su máximo valor, mientras que a una escala de 100 TeV son casi ortogonales, implicando un valor mucho menor. A mayores energías la anisotropía vuelve a crecer, pero en sentido casi opuesto al inicial.

Aunque los datos actuales son insuficientes para caracterizar la anisotropía a energías en torno al PeV, los datos sugieren una nueva dirección no alineada con $\vec{B}_{IS}$. Ello indicaría que el radio de Larmor de los rayos cósmicos alcanza un valor similar a la región de coherencia del campo interestelar, es decir, $R_{IS} \approx r_L \approx 0.3$ pc. En consecuencia, nuestros resultados ofrecen tanto la dirección del campo $\vec{B}_{IS}$ (que está de acuerdo con las recientes observaciones proporcionadas por las sondas Voyager) y una estimación de la escala del tamaño plasma interestelar magnético (desconocido a día de hoy). Estas constituyen las dos predicciones principales que se derivan de nuestro modelo.

También argumentamos que este contexto puede acomodar anisotropías de pequeña y mediana escala similares a las detectadas por Argo, TIBET, Milagro y IceCube. Estas irregularidades podrían aparecer como la imagen del dipolo global deformado por lentes cósmicas mágneticas (discutidas en el capitulo 3), que focalizarían el flujo de rayos cósmicos. Conviene reseñar que las lentes actuarian como fuentes de rayos cósmicos pero la fuente última del efecto será la anistropía de gran escala. En particular si el efecto de la de gran escala es de $O(0.1\%)$, las de pequeña y mediana escala serían del mismo orden. Nuevos experimentos (como SKA) quizás puedan identificar con suficiente claridad objetos astrofísicos con la estructura de una lente magnética.

En el futuro nos gustaría incorporar nuevos datos a nuestro esquema. También consideramos que el efecto del campo magnetico muy próximo al sol merece un un estudio más detallado. Dada la gran actividad en el campo de los rayos cósmicos y la física de astropartículas, parece claro que nos aguardan tiempos interesantes.

Bibliography

Aartsen, M. G., Abbasi, R., Abdou, Y., Ackermann, M., Adams, J., Aguilar, J., Ahlers, M., Altmann, D., Andeen, K., Auffenberg, J. et al. Observation of cosmic-ray anisotropy with the icetop air shower array. *The Astrophysical Journal*, vol. 765(1), page 55, 2013.

Abbasi, R., Abdou, Y., Abu-Zayyad, T., Ackermann, M., Adams, J., Aguilar, J., Ahlers, M., Allen, M., Altmann, D., Andeen, K. et al. Observation of anisotropy in the galactic cosmic-ray arrival directions at 400 tev with icecube. *The Astrophysical Journal*, vol. 746(1), page 33, 2012.

Abbasi, R., Abdou, Y., Abu-Zayyad, T., Adams, J., Aguilar, J., Ahlers, M., Altmann, D., Andeen, K., Auffenberg, J., Bai, X. et al. Observation of anisotropy in the arrival directions of galactic cosmic rays at multiple angular scales with icecube. *The Astrophysical Journal*, vol. 740(1), page 16, 2011.

Abbasi, R., Abdou, Y., Abu-Zayyad, T., Adams, J., Aguilar, J., Ahlers, M., Andeen, K., Auffenberg, J., Bai, X., Baker, M. et al. Measurement of the anisotropy of cosmic-ray arrival directions with icecube. *The Astrophysical Journal Letters*, vol. 718(2), page L194, 2010.

ABDO, A., ALLEN, B., AUNE, T., BERLEY, D., CASANOVA, S., CHEN, C., DINGUS, B., ELLSWORTH, R., FLEYSHER, L., FLEYSHER, R. ET AL. The large-scale cosmic-ray anisotropy as observed with milagro. *The Astrophysical Journal*, vol. 698(2), page 2121, 2009.

ABU-ZAYYAD, T., BELOV, K., BIRD, D. J., BOYER, J., CAO, Z., CATANESE, M., CHEN, G., CLAY, R. W., COVAULT, C., DAI, H. ET AL. Measurement of the cosmic-ray energy spectrum and composition from 1017 to 1018.3 ev using a hybrid technique. *The Astrophysical Journal*, vol. 557(2), page 686, 2001.

ADRIANI, O., BARBARINO, G., BAZILEVSKAYA, G., BELLOTTI, R., BOEZIO, M., BOGOMOLOV, E., BONECHI, L., BONGI, M., BONVICINI, V., BORISOV, S. ET AL. Pamela measurements of cosmic-ray proton and helium spectra. *arXiv preprint arXiv:1103.4055*, 2011.

ADRIANI, O., BARBARINO, G. C., BAZILEVSKAYA, G. A., BELLOTTI, R., BOEZIO, M., BOGOMOLOV, E. A., BONECHI, L., BONGI, M., BONVICINI, V., BORISOV, S., BOTTAI, S., BRUNO, A., CAFAGNA, F., CAMPANA, D., CARBONE, R., CARLSON, P., CASOLINO, M., CASTELLINI, G., CONSIGLIO, L., DE PASCALE, M. P., DE SANTIS, C., DE SIMONE, N., DI FELICE, V., GALPER, A. M., GILLARD, W., GRISHANTSEVA, L., HOFVERBERG, P., JERSE, G., KARELIN, A. V., KOLDASHOV, S. V., KRUTKOV, S. Y., KVASHNIN, A. N., LEONOV, A., MALVEZZI, V., MARCELLI, L., MAYOROV, A. G., MENN, W., MIKHAILOV, V. V., MOCCHIUTTI, E., MONACO, A., MORI, N., NIKONOV, N., OSTERIA, G., PAPINI, P., PEARCE, M., PICOZZA, P., PIZZOLOTTO, C., RICCI, M., RICCIARINI, S. B., ROSSETTO, L., SIMON, M., SPARVOLI, R., SPILLANTINI, P., STOZHKOV, Y. I., VACCHI, A., VANNUCCINI, E., VASILYEV, G., VORONOV, S. A., WU, J., YURKIN, Y. T., ZAMPA, G., ZAMPA, N. and ZVEREV, V. G. Pamela results on the cosmic-ray antiproton flux from 60 mev to 180 gev in kinetic energy. *Phys. Rev. Lett.*, vol. 105, page 121101, 2010.

AGUILAR, M., ALBERTI, G., ALPAT, B., ALVINO, A., AMBROSI, G., ANDEEN, K., ANDERHUB, H., ARRUDA, L., AZZARELLO, P., BACHLECHNER, A., BARAO, F., BARET, B., BARRAU, A., BARRIN, L., BARTOLONI, A., BASARA, L., BASILI, A., BATALHA, L., BATES, J., BATTISTON, R., BAZO, J., BECKER, R., BECKER, U., BEHLMANN, M., BEISCHER, B., BERDUGO, J., BERGES, P., BERTUCCI, B., BIGONGIARI, G., BILAND, A., BINDI, V., BIZZAGLIA, S., BOELLA, G., DE BOER, W., BOLLWEG, K., BOLMONT, J., BORGIA, B., BORSINI, S., BOSCHINI, M. J., BOUDOUL, G., BOURQUIN, M., BRUN, P., BUÉNERD, M., BURGER, J., BURGER, W., CADOUX, F., CAI, X. D., CAPELL, M., CASADEI, D., CASAUS, J., CASCIOLI, V., CASTELLINI, G., CERNUDA, I., CERVELLI, F., CHAE, M. J., CHANG, Y. H., CHEN, A. I., CHEN, C. R., CHEN, H., CHENG, G. M., CHEN, H. S., CHENG, L., CHERNOPLYIOKOV, N., CHIKANIAN, A., CHOUMILOV, E., CHOUTKO, V., CHUNG, C. H., CLARK, C., CLAVERO, R., COIGNET, G., COMMICHAU, V., CONSOLANDI, C., CONTIN, A., CORTI, C., COSTADO DIOS, M. T., COSTE, B., CRESPO, D., CUI, Z., DAI, M., DELGADO, C. and TORRE, D. First result from the alpha magnetic spectrometer on the international space station: Precision measurement of the positron fraction in primary cosmic rays. *Phys. Rev. Lett.*, vol. 110, page 141102, 2013.

AHRENS, J., BAHCALL, J. N., BAI, X., BAY, R., BECKA, T., BECKER, K.-H., BERLEY, D., BERNARDINI, E., BERTRAND, D., BESSON, D. ET AL. Sensitivity of the icecube detector to astrophysical sources of high energy muon neutrinos. *Astroparticle Physics*, vol. 20(5), pages 507–532, 2004.

ALFVÉN, H. and HERLOFSON, N. Cosmic radiation and radio stars. *Phys. Rev.*, vol. 78, pages 616–616, 1950.

ALTSCHULER, M. D. and NEWKIRK JR, G. Magnetic fields and the structure of the solar corona. *Solar Physics*, vol. 9(1), pages 131–149, 1969.

AMENOMORI, M., AYABE, S., BI, X., CHEN, D., CUI, S., DING, L., DING, X., FENG, C., FENG, Z., FENG, Z. ET AL. Anisotropy and corotation of galactic cosmic rays. *Science*, vol. 314(5798), pages 439–443, 2006.

ANDERSON, C. . *Physical Review*, vol. 491(43), 1932.

ANDERSON, C. . *Physical Review*, vol. 263(50), 1936.

AUGER, P. . *Review of Modern Physics*, vol. 288(11), 1939.

AUGER, P. and MAZE, R. . *Comt. Rend. Acad. Sci.*, vol. 228(207), 1938.

BALOGH, A. and ERDÕS, G. The heliospheric magnetic field. *Space Science Reviews*, vol. 176(1-4), pages 177–215, 2013.

BALOGH, A. and JOKIPII, J. The heliospheric magnetic field and its extension to the inner heliosheath. En *From the Outer Heliosphere to the Local Bubble*, pages 85–110. Springer, 2009.

BARTOLI, B., BERNARDINI, P., BI, X., BLEVE, C., BOLOGNINO, I., BRANCHINI, P., BUDANO, A., MELCARNE, A. C., CAMARRI, P., CAO, Z. ET AL. Observation of tev gamma rays from the cygnus region with the argo-ybj experiment. *The Astrophysical Journal Letters*, vol. 745(2), page L22, 2012.

BATTANER, E., CASTELLANO, J. and MASIP, M. Galactic magnetic fields and the large-scale anisotropy at milagro. *The Astrophysical Journal Letters*, vol. 703(1), page L90, 2009.

BATTANER, E., CASTELLANO, J. and MASIP, M. Cosmic magnetic lenses. *arXiv preprint arXiv:1006.2346*, 2010.

BATTANER, E., GARRIDO, J., MEMBRADO, M. and FLORIDO, E. Magnetic fields as an alternative explanation for the rotation curves of spiral galaxies. *Nature*, vol. 360(6405), pages 652–653, 1992.

BECK, R. Galactic and extragalactic magnetic fields. pages 243–260, 2001.

BECK, R. Magnetism in the spiral galaxy NGC 6946: magnetic arms, depolarization rings, dynamo modes and helical fields. 2007.

BECK, R. and KRAUSE, M. Revised equipartition and minimum energy formula for magnetic field strength estimates from radio synchrotron observations. *Astron.Nachr.*, vol. 326, pages 414–427, 2005.

BECK, R. and WIELEBINSKY, R. *Cosmic Magnetic Fields*. Springer, New York, 1st edition, 2005. ISBN 978-3-540-24175-1.

BHABHA, H. J. and HEITLER, W. The passage of fast electrons and the theory of cosmic showers. *Proceedings of the Royal Society of London Series A: Mathematical, Physical & Engineering Sciences*, vol. 159(898), pages 432–458, 1937.

BIERMANN, P. L., TJUS, J. B., SEO, E.-S. and MANDELARTZ, M. Cosmic-ray transport and anisotropies. *The Astrophysical Journal*, vol. 768(2), page 124, 2013.

BIRD, D., CORBATO, S., DAI, H., DAWSON, B., ELBERT, J., EMERSON, B., GREEN, K., HUANG, M., KIEDA, D., LUO, M. ET AL.

The cosmic-ray energy spectrum observed by the fly's eye. *The Astrophysical Journal*, vol. 424, pages 491–502, 1994.

BLASI, P. and AMATO, E. Diffusive propagation of cosmic rays from supernova remnants in the galaxy. ii: anisotropy. *Journal of Cosmology and Astroparticle Physics*, vol. 2012(01), page 011, 2012.

BOLTON, J. and WILD, J. On the Possibility of Measuring Interstellar Magnetic Fields by 21-CM Zeeman Splitting. *Apj*, vol. 125, page 296, 1957.

BONAFEDE, A., FERETTI, L., GIOVANNINI, G., GOVONI, F., MURGIA, M., TAYLOR, G., EBELING, H., ALLEN, S., GENTILE, G. and PIHLSTRÖM, Y. Revealing the magnetic field in a distant galaxy cluster: discovery of the complex radio emission from macs j0717. 5+ 3745. *Astronomy & astrophysics*, vol. 503(3), pages 707–720, 2009.

BOTHE, W. and KOLHORSTER, W. . *Die Natur der Hohenstrahlung*, vol. 17(271), 1929.

BRANDENBURG, A. and REKOWSKI, B. V. Astrophysical significance of the anisotropic kinetic alpha effect. *Astronomy & Astrophysics*, vol. 379(3), pages 1153–1160, 2001.

CASSE, F., LEMOINE, M. and PELLETIER, G. Transport of cosmic rays in chaotic magnetic fields. *Physical Review D*, vol. 65(2), page 023002, 2001.

CLEMENS, M. and BRESSAN, A. The history of star formation and mass assembly in early galaxies. *Monthly Notices of the Royal Astronomical Society: Letters*, vol. 392(1), pages 35–39, 2009.

COLLABORATION, I. ET AL. Evidence for high-energy extraterrestrial neutrinos at the icecube detector. *Science*, vol. 342(6161), page 1242856, 2013.

COMPTON, A. . *Physical Review*, vol. 111(41), 1932.

COMPTON, A. H. and GETTING, I. A. An Apparent Effect of Galactic Rotation on the Intensity of Cosmic Rays. *Physical Review*, vol. 47, pages 817–821, 1935.

COUTU, S. Positrons galore. *Physics*, vol. 6, page 40, 2013.

CRUTCHER, M. and THOMAS, H. Oh zeeman measurement of the magnetic field in the l1544 core. *The Astrophysical Journal Letters*, vol. 537(2), page L139, 2000.

CRUTCHER, R. M. Magnetic fields in molecular clouds. *Annual Review of Astronomy and Astrophysics*, vol. 50, pages 29–63, 2012.

CUI, S. Study on large-scale cr anisotropy with argo-ybj experiment. En *International Cosmic Ray Conference*, vol. 1, page 6. 2011.

DAVIES, R. and WILSON, A. Interstellar magnetic fields determined from zeeman effect measurements. 1968.

DAVIS, L. and GREENSTEIN, J. The polarization of starlight by aligned dust grains. *Astrophysical Journal*, vol. 114(1), 1951.

DELGADO, R. M. G., PÉREZ, E., TADHUNTER, C., VILCHEZ, J. M. and RODRIGUEZ-ESPINOSA, J. M. H ii region population in a sample of nearby galaxies with nuclear activity. i. data and general results. *The Astrophysical Journal Supplement Series*, vol. 108(1), page 155, 1997.

DESIATI, P. and LAZARIAN, A. Anisotropy of tev cosmic rays and outer heliospheric boundaries. *The Astrophysical Journal*, vol. 762(1), page 44, 2013.

DETTMAR, R.-J. and SOIDA, M. Magnetic fields in halos of spiral galaxies. *Astronomische Nachrichten*, vol. 327(5-6), pages 495–498, 2006.

DOLAG, K. and BARTELMANN, M. Qso-galaxy correlations induced by weak lensing in arbitrary friedmann-lemaitre cosmologies. *Monthly Notices of the Royal Astronomical Society*, vol. 291(3), pages 446–454, 1997.

DRAINE, B. Interstellar dust grains. *arXiv preprint astro-ph/0304489*, 2003.

FERMI, E. On the Origin of the Cosmic Radiation. *Phys.Rev.*, vol. 75, pages 1169–1174, 1949.

FERRIERE, K. Interstellar magnetic fields in the Galactic center region. 2009.

FRISCH, P. C., ANDERSSON, B., BERDYUGIN, A., FUNSTEN, H. O., MAGALHAES, A. M., MCCOMAS, D. J., PIIROLA, V., SCHWADRON, N. A., SLAVIN, J. D. and WIKTOROWICZ, S. J. Comparisons of the interstellar magnetic field directions obtained from the ibex ribbon and interstellar polarizations. *The Astrophysical Journal*, vol. 724(2), page 1473, 2010.

FRISCH, P. C., BZOWSKI, M., GRUN, E., IZMODENOV, V., KRKRUGER, H., LINSKY, J., MCCOMAS, D., MOBIUS, E., REDFIELD, S., SCHWADRON, N. ET AL. The galactic environment of the sun: interstellar material inside and outside of the heliosphere. *Space science reviews*, vol. 146(1-4), pages 235–273, 2009.

Gaisser, T. K. *Cosmic rays and particle physics*. Cambridge University Press, 1990.

Giacalone, J. and Jokipii, J. The transport of cosmic rays across a turbulent magnetic field. *The Astrophysical Journal*, vol. 520(1), page 204, 1999.

Gonçalves, J., Galli, D. and Girart, J. M. Modeling the magnetic field in the protostellar source ngc 1333 iras 4a. *Astronomy & Astrophysics*, vol. 490(3), pages L39–L42, 2008.

Guillian, G., Hosaka, J., Ishihara, K., Kameda, J., Koshio, Y., Minamino, A., Mitsuda, C., Miura, M., Moriyama, S., Nakahata, M. et al. Observation of the anisotropy of 10 tev primary cosmic ray nuclei flux with the super-kamiokande-i detector. *Physical Review D*, vol. 75(6), page 062003, 2007.

Gurnett, D., Kurth, W., Burlaga, L. and Ness, N. In situ observations of interstellar plasma with voyager 1. *Science*, vol. 341(6153), pages 1489–1492, 2013.

Han, J. The magnetic structure of our galaxy: a review of observations. *Proceedings of the International Astronomical Union*, vol. 4(S259), pages 455–466, 2008.

Han, J. Cosmic magnetic fields: From planets, to stars and galaxies (iau symp. 259), ed. 2009.

Han, J., Ferriere, K. and Manchester, R. The spatial energy spectrum of magnetic fields in our galaxy. *The Astrophysical Journal*, vol. 610(2), page 820, 2004.

Han, J., Manchester, R., Lyne, A., Qiao, G. and Van Straten, W. Pulsar rotation measures and the large-scale structure of the galactic magnetic field. *The Astrophysical Journal*, vol. 642(2), page 868, 2006.

HAN, J., MANCHESTER, R. and QIAO, G. Pulsar rotation measures and the magnetic structure of our galaxy. *Monthly Notices of the Royal Astronomical Society*, vol. 306(2), pages 371–380, 1999.

HARARI, D., MOLLERACH, S., ROULET, E. and SANCHEZ, F. Lensing of ultra-high energy cosmic rays in turbulent magnetic fields. *Journal of High Energy Physics*, vol. 2002(03), page 045, 2002.

HARWIT, M. *Astrophysical concepts*. Springer, New York, 4th edition, 2006. ISBN 978-0-387-32943-7.

HESS, V. . *Physilalische Zeitschrift*, vol. 13(1084), 1912.

HILLAS, A. Can diffusive shock acceleration in supernova remnants account for high-energy galactic cosmic rays? *J.Phys.*, vol. G31, pages R95–R131, 2005.

HILLAS, A. M. Cosmic rays: Recent progress and some current questions. *arXiv preprint astro-ph/0607109*, 2006.

HILTNER, W. . *Astrophysical Journal*, vol. 471(109), 1949.

ILLANA, J. I., MASIP, M. and MELONI, D. A new physics interpretation of the icecube data. *Astroparticle Physics*, vol. 65, pages 64–68, 2015.

KOLMOGOROV, A. N. Dissipation of energy in locally isotropic turbulence. En *Dokl. Akad. Nauk SSSR*, vol. 32, pages 16–18. 1941.

KRIMIGIS, S. M., ROELOF, E. C., DECKER, R. B. and HILL, M. E. Zero outward flow velocity for plasma in a heliosheath transition layer. *Nature*, vol. 474(7351), pages 359–361, 2011.

KROEGER, R. . *Astrophysical Journal*, vol. 816(303), 1986.

LAZARIAN, A. and DESIATI, P. Magnetic reconnection as the cause of cosmic ray excess from the heliospheric tail. *The Astrophysical Journal*, vol. 722(1), page 188, 2010.

LEINERT, C., BOWYER, S., HAIKALA, L., HANNER, M., HAUSER, M., LEVASSEUR-REGOURD, A.-C., MANN, I., MATTILA, K., REACH, W., SCHLOSSER, W. ET AL. The 1997 reference of diffuse night sky brightness. 1997.

LEMAITRE, G. and VALLARTA, M. S. On compton's latitude effect of cosmic radiation. *Physical Review*, vol. 43(2), page 87, 1933.

LINSKY, J. L. Deuterium abundance in the local ism and possible spatial variations. En *Primordial Nuclei and their Galactic evolution*, pages 285–296. Springer, 1998.

LISENFELD, U. and VOELK, H. J. Shock acceleration of relativistic particles in galaxy-galaxy collisions. *Astronomy & Astrophysics*, vol. 524, page A27, 2010.

LONGAIR, M. S. *High energy astrophysics*. cambridge university Press, 2011.

LYNE, A. and RICKETT, B. Radio observations of five pulsars. 1968.

LYNE, A. and SMITH, F. Linear Polarization in Pulsating Radio Sources. *Nature*, vol. 218, page 124, 1968.

MANCUSO, S. and SPANGLER, S. R. Faraday rotation and models for the plasma structure of the solar corona. *The Astrophysical Journal*, vol. 539(1), page 480, 2000.

MATTHEWS, J. A heitler model of extensive air showers. *Astroparticle Physics*, vol. 22(5), pages 387–397, 2005.

MCCOMAS, D., ALEXASHOV, D., BZOWSKI, M., FAHR, H., HEERIKHUISEN, J., IZMODENOV, V., LEE, M., MÖBIUS, E., POGORELOV, N., SCHWADRON, N. ET AL. The heliosphereâs interstellar interaction: No bow shock. *Science*, vol. 336(6086), pages 1291–1293, 2012.

MCCOMAS, D., ALLEGRINI, F., BOCHSLER, P., BZOWSKI, M., CHRISTIAN, E., CREW, G., DEMAJISTRE, R., FAHR, H., FICHTNER, H., FRISCH, P. ET AL. Global observations of the interstellar interaction from the interstellar boundary explorer (ibex). *Science*, vol. 326(5955), pages 959–962, 2009.

MCCOMAS, D., FUNSTEN, H., FUSELIER, S., LEWIS, W., MÖBIUS, E. and SCHWADRON, N. Ibex observations of heliospheric energetic neutral atoms: Current understanding and future directions. *Geophysical Research Letters*, vol. 38(18), 2011.

MCLENNAN, J. . *Physical Review*, vol. 16(184), 1903.

MICHEL, R., BODEMANN, R., BUSEMANN, H., DAUNKE, R., GLORIS, M., LANGE, H.-J., KLUG, B., KRINS, A., LEYA, I., LÜPKE, M. ET AL. Cross sections for the production of residual nuclides by low-and medium-energy protons from the target elements c, n, o, mg, al, si, ca, ti, v, mn, fe, co, ni, cu, sr, y, zr, nb, ba and au. *Nuclear Instruments and Methods in Physics Research Section B: Beam Interactions with Materials and Atoms*, vol. 129(2), pages 153–193, 1997.

MILLIKAN, R. . *Proceedings of the National Academy of Sciences*, vol. 1(12), 1926.

MITRA, D., WIELEBINSKI, R., KRAMER, M. and JESSNER, A. The effect of hii regions on rotation measure of pulsars. *Astronomy & Astrophysics*, vol. 398(3), pages 993–1005, 2003.

MUNOZ, C. Dark matter detection in the light of recent experimental results. *International Journal of Modern Physics A*, vol. 19(19), pages 3093–3169, 2004.

NAGANO, M., HARA, T., HATANO, Y., HAYASHIDA, N., KAWAGUCHI, S., KAMATA, K., KIFUNE, T. and MIZUMOTO, Y. Energy spectrum of primary cosmic rays between 1014.5 and 1018 ev. *Journal of Physics G: Nuclear Physics*, vol. 10(9), page 1295, 1984.

NAKAMURA, K. . *Review of Particle Physics*, vol. 1(37), 2010.

OPPERMANN, N., JUNKLEWITZ, H., GREINER, M., ENSSLIN, T. A., AKAHORI, T., CARRETTI, E., GAENSLER, B. M., GOOBAR, A., HARVEY-SMITH, L., JOHNSTON-HOLLITT, M. ET AL. Estimating extragalactic faraday rotation. *A&A*, 2014.

PAPITASHVILI, V., PAPITASHVILI, N. and KING, J. Solar cycle effects in planetary geomagnetic activity: Analysis of 36-year long omni dataset. *Geophysical research letters*, vol. 27(17), pages 2797–2800, 2000.

PARKER, E. The generation of magnetic fields in astrophysical bodies. iii. turbulent diffusion of fields and efficient dynamos. *The Astrophysical Journal*, vol. 163, page 279, 1971.

PARKER, E. N. Dynamics of the interplanetary gas and magnetic fields. *The Astrophysical Journal*, vol. 128, page 664, 1958.

PARKER, E. N. Dynamics of the Interplanetary Gas and Magnetic Fields. *ApJ*, vol. 128, page 664, 1958.

PÉREZ-GARCÍA, M. Á., KOTERA, K. and SILK, J. Anisotropy in cosmic rays from internal transitions in neutron stars. *Nuclear Instruments and Methods in Physics Research Section A: Accelerators, Spectrometers, Detectors and Associated Equipment*, vol. 742, pages 237–240, 2014.

POGORELOV, N. V., HEERIKHUISEN, J. and ZANK, G. P. Probing Heliospheric Asymmetries with an MHD-kinetic Model. 2008.

POHL, M. and EICHLER, D. Understanding tev-band cosmic-ray anisotropy. *The Astrophysical Journal*, vol. 766(1), page 4, 2013.

PTUSKIN, V., JONES, F., SEO, E. and SINA, R. Effect of random nature of cosmic ray sources–supernova remnants–on cosmic ray intensity fluctuations, anisotropy, and electron energy spectrum. *Advances in Space Research*, vol. 37(10), pages 1909–1912, 2006.

PTUSKIN, V., ZIRAKASHVILI, V. and SEO, E. Spectrum of Galactic Cosmic Rays Accelerated in Supernova Remnants. *Astrophys.J.*, vol. 718, pages 31–36, 2010.

RATKIEWICZ, R. and GRYGORCZUK, J. Orientation of the local interstellar magnetic field inferred from voyagers' positions. *Geophysical Research Letters*, vol. 35(23), 2008.

RIEGER, F. M., BOSCH-RAMON, V. and DUFFY, P. Fermi acceleration in astrophysical jets. *Astrophys.Space Sci.*, vol. 309, pages 119–125, 2007.

RUBIÑO-MARTIN, J., REBOLO, R., AGUIAR, M., GÉNOVA-SANTOS, R., GÓMEZ-REÑASCO, F., HERREROS, J., HOYLAND, R., LÓPEZ-CARABALLO, C., SANTOS, A. P., DE LA ROSA, V. S. ET AL. The quijote-cmb experiment: studying the polarisation of the galactic and cosmological microwave emissions. En *SPIE Astronomical*

Telescopes+ Instrumentation, pages 84442Y–84442Y. International Society for Optics and Photonics, 2012.

RUIZ-GRANADOS, B., BATTANER, E., CALVO, J., FLORIDO, E. and RUBIÑO-MARTÍN, J. Dark matter, magnetic fields, and the rotation curve of the milky way. *The Astrophysical Journal Letters*, vol. 755(2), page L23, 2012.

RUIZ-GRANADOS, B., RUBIÑO-MARTÍN, J. and BATTANER, E. A study of the regular structure of the galactic magnetic field using wmap5 polarization data at 22 ghz. *Proceedings of the International Astronomical Union*, vol. 4(S259), pages 573–576, 2008.

RUIZ-GRANADOS, B., RUBIÑO-MARTÍN, J. and BATTANER, E. Constraining the regular galactic magnetic field with the 5-year wmap polarization measurements at 22 ghz. *Astronomy & Astrophysics*, vol. 522, page A73, 2010.

RUTHERFORD, E. . *Ibid*, vol. 16(183), 1903.

RYBICKI, G. B. and LIGHTMAN, A. P. *Radiative Processes in Astrophysics*. Wiley, New York, 2th edition, 1986. ISBN 978-0-387-32943-8.

SANTANDER, M., COLLABORATION, I. ET AL. Anisotropy of tev and pev cosmic rays with icecube and icetop. *Nuclear Instruments and Methods in Physics Research Section A: Accelerators, Spectrometers, Detectors and Associated Equipment*, vol. 725, pages 85–88, 2013.

SCHWINGER, J. On the classical radiation of accelerated electrons. *Phys. Rev.*, vol. 75, pages 1912–1925, 1949.

SHAVIV, N. J., HEYL, J. S. and LITHWICK, Y. Magnetic lensing near ultramagnetized neutron stars. *Monthly Notices of the Royal Astronomical Society*, vol. 306(2), pages 333–347, 1999.

SINNIS, G., COLLABORATION, H. ET AL. Hawc: A next generation vhe all-sky telescope. En *HIGH ENERGY GAMMA-RAY ASTRONOMY: 2nd International Symposium on High Energy Gamma-Ray Astronomy*, vol. 745, pages 234–245. AIP Publishing, 2005.

SLANE, P., CHEN, Y., SCHULZ, N. S., SEWARD, F. D., HUGHES, J. P. and GAENSLER, B. M. Chandra observations of the crab-like supernova remnant g21. 5–0.9. *The Astrophysical Journal Letters*, vol. 533(1), page L29, 2000.

SOFUE, Y., FUJIMOTO, M. and WIELEBINSKI, R. Global structure of magnetic fields in spiral galaxies. *Annual review of astronomy and astrophysics*, vol. 24, pages 459–497, 1986.

SREEKUMAR, P., BERTSCH, D., DINGUS, B., ESPOSITO, J., FICHTEL, C., HARTMAN, R., HUNTER, S., KANBACH, G., KNIFFEN, D., LIN, Y. ET AL. Egret observations of the extragalactic gamma-ray emission. *The Astrophysical Journal*, vol. 494(2), page 523, 1998.

STANEV, T. Ultrahigh-energy cosmic rays and the large scale structure of the galactic magnetic field. *Astrophys.J.*, vol. 479, page 290, 1997.

STANEV, T. *High energy cosmic rays*. Springer Science & Business Media, 2010.

STEPINSKI, T. F. Character of dynamo-generated magnetic fields in viscous protostellar disks. En *Revista Mexicana de Astronomia y Astrofisica Conference Series*, vol. 1, page 267. 1995.

Stomer, C. . *Terrestial Magnetism and Atmospheric Electricity*, vol. 139(35), 1930.

Stone, E., Cummings, A., McDonald, F., Heikkila, B., Lal, N. and Webber, W. Voyager 1 explores the termination shock region and the heliosheath beyond. *Science*, vol. 309(5743), pages 2017–2020, 2005.

Stone, E. C., Cummings, A. C., McDonald, F. B., Heikkila, B. C., Lal, N. and Webber, W. R. An asymmetric solar wind termination shock. *Nature*, vol. 454(7200), pages 71–74, 2008.

Strassmeier, K., Kosovichev, A. and Beckman, J. Magnetic structure of our galaxy: A review of observations. *arXiv preprint arXiv:0901.1165*, 2009.

Strong, A. W., Moskalenko, I. V. and Ptuskin, V. S. Cosmic-ray propagation and interactions in the galaxy. *arXiv preprint astro-ph/0701517*, 2007.

Takeda, M. a., Hayashida, N., Honda, K., Inoue, N., Kadota, K., Kakimoto, F., Kamata, K., Kawaguchi, S., Kawasaki, Y., Kawasumi, N. et al. Extension of the cosmic-ray energy spectrum beyond the predicted greisen-zatsepin-kuzmin cutoff. *Physical Review Letters*, vol. 81(6), page 1163, 1998.

Thimann, K. V. and Bonner Jr, W. D. Experiments on the growth and inhibition of isolated plant parts. i. the action of iodoacetate and organic acids on the avena coleoptile. *American Journal of Botany*, pages 271–281, 1948.

Vallée, J. P. Cosmic magnetic fields as observed in the universe, in galactic dynamos, and in the milky way. *New Astronomy Reviews*, vol. 48(10), pages 763–841, 2004.

WIELEBINSKI, R. and BECK, R. *Cosmic magnetic fields*, vol. 664. Springer Science & Business Media, 2005.

WIELEBINSKI, R. and MITRA, D. Galactic magnetic fields and foreground effects. En *Radio Pulsars*, vol. 302, page 257. 2003.

WULF, T. . *Physikalische Zeitscrift*, vol. 10(152), 1909.

YANASAK, N., WIEDENBECK, M., BINNS, W., CHRISTIAN, E., CUMMINGS, A., DAVIS, A., GEORGE, J., HINK, P., ISRAEL, M., LESKE, R. ET AL. Cosmic-ray time scales using radioactive clocks. *Advances in Space Research*, vol. 27(4), pages 727–736, 2001.

ZANK, G. Interaction of the solar wind with the local interstellar medium: A theoretical perspective. *Space Science Reviews*, vol. 89(3-4), pages 413–688, 1999.

ZATSEPIN, G. and KUZMIN, V. Upper limit of the spectrum of cosmic rays. *JETP Lett.*, vol. 4, pages 78–80, 1966.

Appendix

The Astrophysical Journal, 799:157 (7pp), 2015 February 1 doi:10.1088/0004-637X/799/2/157

MAGNETIC FIELDS AND COSMIC-RAY ANISOTROPIES AT TeV ENERGIES

Eduardo Battaner, Joaquín Castellano, and Manuel Masip
Departamento de Física Teórica y del Cosmos, Universidad de Granada, E-18071 Granada, Spain; battaner@ugr.es, jcastellano@correo.ugr.es, masip@ugr.es

Received 2014 August 26; accepted 2014 November 14; published 2015 January 27

ABSTRACT

Several cosmic-ray (CR) observatories have provided high-accuracy maps of the sky at TeV–PeV energies. The data reveal an $O(0.1\%)$ deficit from north galactic directions that peaks at 10 TeV and then evolves with the energy, together with other anisotropies at smaller angular scales. Using the Boltzmann equation, we derive expressions for the CR flux that fit these features. The anisotropies depend on the local interstellar magnetic field $\boldsymbol{B}_{\mathrm{IS}}$, on the average galactic field $\boldsymbol{B}_R$ in our vicinity, and on correlations between fluctuating quantities. We show that the initial dipole anisotropy along $\boldsymbol{B}_{\mathrm{IS}}$ can be modulated by changes in the global CR *flow*, and that a variation in the dipole direction would imply a given radius of coherence for the local $\boldsymbol{B}_{\mathrm{IS}}$. We also show that small- and medium-scale anisotropies may appear when the full-sky anisotropy finds a field configuration acting as a magnetic lens.

Key words: cosmic rays – ISM: magnetic fields

1. INTRODUCTION

We observe charged cosmic rays (CRs; protons and atomic nuclei) with energies of up to 10^{11} GeV. Although in their way to the Earth these particles lose directionality, they carry important information about their sources and about the environment where they have propagated. For example, the observation that boron is more frequent in CRs than in the solar system suggests that it is produced when heavier nuclei *break* on their way to the Earth, implying that they cross an average depth of 10 g cm^{-2} of interstellar (IS) baryonic matter in their trajectory from the dominant sources (Reeves et al. 1970).

At TeV energies magnetic fields trap charged CRs in the IS medium, and their transport is usually modeled by a diffusion equation (Shalchi 2009). One expects that the CR gas propagates along the parallel and the perpendicular directions to the background field $\boldsymbol{B}$ with different diffusion coefficients, scattering with the magnetic turbulences $\delta \boldsymbol{B}$ in the plasma. In particular, if we define the Larmor radius as

$$r_L = \frac{E}{QBc} = \left(\frac{E}{1\ \mathrm{TeV}}\right)\left(\frac{1\ \mu\mathrm{G}}{B}\right)\left(\frac{e}{Q}\right) 1.1 \times 10^{-3}\ \mathrm{pc}, \quad (1)$$

a CR will predominantly be diffused by magnetic irregularities of wavenumber $k \approx 1/r_L$. In a first approximation, one may picture its trajectory as a helix along $\boldsymbol{B}$ of radius $r_L\sqrt{1-\mu^2}$ and velocity

$$v_\parallel = c\mu, \quad v_\perp = c\sqrt{1-\mu^2}, \quad (2)$$

with random changes in $v_\parallel$ after a parallel mean free path $\lambda_\parallel$. Such change will also imply a variation in the field line trapping the CR, i.e., $\lambda_\perp \approx r_L$.

A diffusion equation admits a multipole expansion (Jones 1990) with isotropy at order zero and a dipole along the gradient direction at first order. However, this information is deduced a posteriori, as in a diffusion equation the momenta of the gas particles have been averaged. The Boltzmann equation, instead, gives the evolution in phase space of the statistical distribution function $f(\boldsymbol{r}, \boldsymbol{p}; t)$ (density of particles at $\boldsymbol{r}$ with momentum $\boldsymbol{p}$), providing a microscopic description of the fluid (Battaner 2009; Ahlers 2014). It is easy to see that when we measure the CR differential flux $F(\boldsymbol{u}, E; t)$ (number of particles crossing the unit area from a given direction $\boldsymbol{u}$ per unit solid angle, energy, and time), we can directly *read* the distribution function:

$$f\left(\boldsymbol{r}_{\mathrm{Earth}}, -\frac{E}{c}\boldsymbol{u}; t\right) = \frac{c^2}{E^2} F(\boldsymbol{u}, E; t), \quad (3)$$

where we have taken the relativistic limit with $E = cp$. Therefore, it is interesting to explore how the appearance of anisotropies may be explained with the Boltzmann equation, especially in an environment with regular magnetic fields at different scales (see below).

In this article we will attempt a description of several large- and medium-scale anisotropies observed in the CR flux by several experiments. The combined results from TIBET (Amenomori et al. 2006), MILAGRO (Abdo et al. 2008), ARGO-YBF (Di Sciascio et al. 2012), SuperKamiokande (Guillian et al. 2007), ANTARES (Mangano 2009), IceCube (Aartsen et al. 2013; Santander 2013), and HAWC (Abeysekara et al. 2013) provide a picture of the whole sky at different energies. The data reveal that the almost perfect isotropy is broken by a $O(10^{-3})$ dipole-like feature that appears at 1 TeV and evolves with the energy, together with other irregularities at lower angular scales (Zotov & Kulikov 2012; Iuppa 2012).

It seems clear that the direction of the local IS magnetic field $\boldsymbol{B}_{\mathrm{IS}}$ should be a key ingredient in the explanation of these anisotropies (Schwadron et al. 2014). *Voyager* data (Ratkiewicz et al. 2008) on the heliospheric boundary provide an estimate for the direction of $\boldsymbol{B}_{\mathrm{IS}}$:

$$\ell_B = 217^\circ \pm 14^\circ; \quad b_B = -49^\circ \pm 8^\circ \quad (4)$$

(in galactic coordinates), whereas IS atom measurements with the *Interstellar Boundary Explorer* (*IBEX*) (Frisch et al. 2012) imply

$$\ell_B = 210\overset{\circ}{.}5 \pm 2\overset{\circ}{.}6; \quad b_B = -57\overset{\circ}{.}1 \pm 1\overset{\circ}{.}0. \quad (5)$$

Although the region of coherence of such a field is unknown (it could vary from 0.01 to 10 pc), it is much larger than the gyroradius of a TeV CR (in Equation (1)). At even larger distances (above 10 pc) the average magnetic field $\boldsymbol{B}_R$ can be measured using a variety of methods (Beck 2005; Wielebinski 2005; Han 2009; Battaner 2009; Ruiz-Granados et al. 2010): polarized thermal dust emission from clouds, Zeeman splitting of lines, or Faraday rotation of polarized galactic and extragalactic sources, among others. The data seem to reveal a $B_R \approx 3\,\mu$G field pointing clockwise ($\ell_B \approx 90^\circ$) in the galactic plane ($b_B \approx 0^\circ$) (Han 2009). We will also study the role that this global magnetic field plays in the explanation of the CR anisotropy.

In Section 2 we start by discussing the anisotropy that would be expected for a single CR source and an isotropic propagation. We then use the Boltzmann equation to analyze how the anisotropy is deformed by the presence of a magnetic field $\boldsymbol{B}_{\rm IS}$. We will assume that the dominant CR sources are beyond the region of coherence of $\boldsymbol{B}_{\rm IS}$ and that their effect is captured by boundary conditions. In Section 3 we review the trajectory of CRs in the absence of turbulences. In particular, we study the *image* of a point-like source and show that there are many trajectories connecting the source with a given observer. Such a study will be necessary to understand the appearance of small- and medium-scale anisotropies. In Sections 4 and 5, respectively, we analyze the data and summarize our results.

2. LARGE-SCALE ANISOTROPIES

Let us first consider the simplest flux: a CR gas from a point-like source S propagating through a turbulent but homogeneous and isotropic medium. Such a medium would correspond to the absence of a regular magnetic field $\boldsymbol{B}_{\rm IS}$ (or to the presence of a field weaker than the fluctuations $\delta\boldsymbol{B}$ of wavenumber $k \approx 1/r_L$), and it implies the same diffusion coefficient κ in all directions. The trajectories will define in this case a three-dimensional random walk of step $\lambda = 3\kappa/c$. The mean displacement D from the source that a particle reaches after a (large) time t is then (Shalchi 2009)

$$D = \sqrt{2\kappa t}. \tag{6}$$

The expression above implies that the radial velocity of the gas (we call it the *CR flow*, since an observer moving at that velocity would observe an isotropic flux) will decrease like $1/\sqrt{t}$ with the distance D from S:

$$v_{\rm gas} \approx \sqrt{\frac{2\kappa}{t + 2\kappa/c^2}} = c\left(\frac{c^2 D^2}{4\kappa^2} + 1\right)^{-1/2}. \tag{7}$$

The relative difference between the CR flux going away and toward the source (the forward-backward asymmetry A^{FB}) can then be estimated as the ratio

$$A^{FB} \approx \frac{v_{\rm gas}}{c} \approx \frac{2\kappa}{cD}. \tag{8}$$

This means that the point-like source will introduce an anisotropy in the CR flux proportional to $1/D$ and to λ. Basically, it is a dipole anisotropy with the excess pointing toward S:

$$F(\boldsymbol{u}) = F_0\,(1 + \boldsymbol{u}\cdot\boldsymbol{d}), \tag{9}$$

where

$$\boldsymbol{d} = \frac{A^{FB}}{2\pi}\,\boldsymbol{u}_S. \tag{10}$$

When there are several sources S_i, it is straightforward to show that the addition of the corresponding dipole anisotropies $\boldsymbol{d}_i$ gives *another* dipole $\boldsymbol{d}$ (Giacinti et al. 2012)

$$\boldsymbol{d} = \frac{\sum_i F_0^{(i)}\,\boldsymbol{d}_i}{\sum_j F_0^{(j)}}. \tag{11}$$

In summary, for an isotropic CR propagation we may expect a dipole anisotropy pointing toward the average CR source (Pohl & Eichler 2013), with its intensity inversely proportional to the distance to these sources and proportional to the mean free path between collisions. Notice, however, that the presence of a regular magnetic field $\boldsymbol{B}_{\rm IS}$ will introduce an asymmetry between the parallel and the perpendicular diffusion coefficients ($\kappa_\parallel$ and $\kappa_\perp$) that will change this result.

To find out how, let us assume a local $\boldsymbol{B}_{\rm IS}$ coherent over distances $R_{\rm IS} \gg r_L, \lambda_\parallel$, with $\lambda_\parallel = 3\kappa_\parallel/c$. We will treat the CRs (protons of energy between 1 and 1000 TeV) as a fluid that only interacts with the magnetic fields. To obtain the average CR anisotropy in our vicinity, we will separate the magnetic field and the distribution function into a regular plus a turbulent component,

$$\begin{aligned} f &\to \bar{f} + \delta f, \\ \boldsymbol{B} &\to \boldsymbol{B}_{\rm IS} + \delta\boldsymbol{B}, \end{aligned} \tag{12}$$

with

$$\langle\,\delta\boldsymbol{B}\,\rangle = \langle\,\delta f\,\rangle = 0, \tag{13}$$

and we will *average* the Boltzmann equation over nearby points. Given the relatively small distance and timescales, we will take stationary and homogeneous magnetic field $\boldsymbol{B}_{\rm IS}$ and distribution function $\bar{f}$. We are then assuming that the CR sources are far enough so that the spatial gradient $\nabla_r \bar{f}$ is negligible (i.e., smaller than $\delta f/R_{\rm IS}$), and that the changes in f occur on timescales much larger than the period of data taking (the movement of the Earth around the Sun introduces irregularities of order 10^{-4}, i.e., a 10% correction to the large-scale anisotropy under consideration), and we ignore energy loss or collisions with IS matter. For a fixed CR energy, $\bar{f}$ must satisfy the Boltzmann equation:

$$\boldsymbol{F}\cdot\nabla_u\,\bar{f}(\boldsymbol{u}) = e\,(\boldsymbol{u}\times\boldsymbol{B})\cdot\nabla_u\,\bar{f}(\boldsymbol{u}) = 0, \tag{14}$$

where $\boldsymbol{u} = \boldsymbol{p}/p$ and $\boldsymbol{p}$ is the momentum of the CR. The equation above can also be written as

$$\boldsymbol{u}\cdot(\boldsymbol{B}\times\nabla_u\,\bar{f}) = 0, \tag{15}$$

which admits the generic solution

$$\bar{f}(\boldsymbol{u}) = \bar{f}(\boldsymbol{u}\cdot\boldsymbol{u}_B). \tag{16}$$

Any stationary and homogeneous solution must then be a function with symmetry around the axis of the magnetic field: $\boldsymbol{B}_{\rm IS}$ will *isotropize* the flux in the directions orthogonal to its axis. In particular, these solutions may accommodate a dipole along $\boldsymbol{u}_B$,

$$\bar{f}(\boldsymbol{u}) = f_0\,(1 - \boldsymbol{u}\cdot\boldsymbol{d}), \tag{17}$$

with

$$\boldsymbol{d} = \frac{A^{FB}}{2\pi}\,\boldsymbol{u}_B. \tag{18}$$

This distribution function will define (see Equation (3)) the dipolar flux in (9) with $\boldsymbol{u}_S \to \boldsymbol{u}_B$ and $F_0 = f_0(E/c)^2$, i.e., it is $\boldsymbol{B}_{\rm IS}$ (and not the position of the sources) that fixes the direction of the CR *flow* in our frame, defined[1] as

$$\boldsymbol{v}_0/c = \frac{1}{N}\int d\Omega\; f(\boldsymbol{u})\,\boldsymbol{u}, \tag{19}$$

with $N = \int d\Omega\; f(\boldsymbol{u})$.

---

[1] Notice that an observer moving at $\boldsymbol{v}_0$ will see no net flux and complete isotropy. This velocity may coincide or not (for example, owing to an asymmetry in the location of CR sources) with the velocity of the local plasma *wind*.

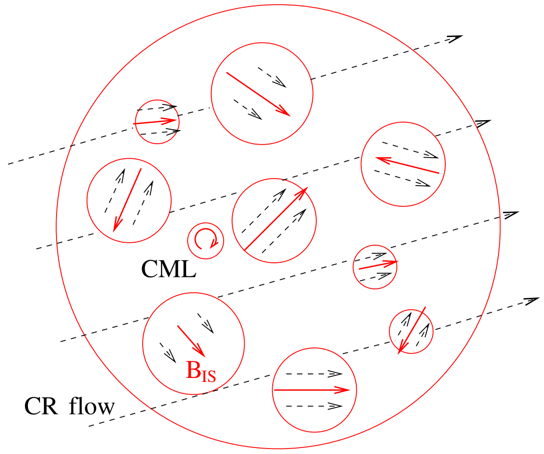

Figure 1. $\boldsymbol{B}_{\rm IS}$ (within coherence cells of 0.1–10 pc) and CR *flow*. CML indicates a cosmic magnetic lens (Battaner et al. 2011).

The (forward or backward) direction along $\boldsymbol{B}_{\rm IS}$ and the intensity of this dipole anisotropy will depend on boundary conditions that, in turn, will reflect the average direction of the CR *flow* (Biermann et al. 2013; Qu et al. 2012) at larger scales.

In Figure 1 we plot a scheme of the CR flow within different cells that contain a regular $\boldsymbol{B}_{\rm IS}$. This field may change randomly from cell to cell, although it has an average value $\boldsymbol{B}_R$ at kiloparsec scales (Han 2009). Our result above has been obtained for an observer at rest within our local IS medium. The CR anisotropy in each cell (which may have a velocity relative to us) will then follow the $\boldsymbol{B}_{\rm IS}$ magnetic lines, with a forward or backward direction depending on the projection of the global (average) flow $\boldsymbol{d}_R$ along $\boldsymbol{B}_{\rm IS}$. In particular, notice that $\boldsymbol{d} \approx 0$ for a $\boldsymbol{B}_{\rm IS}$ orthogonal to $\boldsymbol{d}_R$. Notice also that we are neglecting the velocity $v \approx 23\,{\rm km\,s^{-1}}$ (McComas et al. 2012) of the Sun relative to our cell of local IS medium and the velocity $v' \approx 30\,{\rm km\,s^{-1}}$ of the Earth around the Sun. These movements imply Compton–Getting (Compton & Getting 1935) irregularities—in the sense that they are caused by the velocity of the observer—of order $v/c = O(10^{-4})$, introducing 10% corrections to the dominant anisotropy along $\boldsymbol{B}_{\rm IS}$.

An important question would then be what to expect for the average CR *flow*. Is it $\boldsymbol{d}_R = \langle \boldsymbol{d} \rangle$, a dipole along the direction of the average magnetic field $\boldsymbol{B}_R = \langle \boldsymbol{B}_{\rm IS} \rangle$? To answer this question, we again separate the magnetic field and the distribution function into a regular plus a fluctuating component, but now we average the Boltzmann equation over larger distances, which will include different (nearby) cells:

$$\begin{aligned} f &\rightarrow f_R + \delta f, \\ \boldsymbol{B} &\rightarrow \boldsymbol{B}_R + \delta \boldsymbol{B}. \end{aligned} \tag{20}$$

Although $\delta\boldsymbol{B}$ and δf vary randomly from one cell to another, there may be correlations between both turbulent components (i.e., their relative value in each cell is not random). We will assume

$$\begin{aligned} \langle\, e\, (\boldsymbol{u} \times \delta\boldsymbol{B}) \cdot \nabla_u\, \delta f\, \rangle &= e\, \boldsymbol{u} \cdot \langle\, \delta\boldsymbol{B} \times \nabla_u\, \delta f\, \rangle \\ &= e\, \boldsymbol{u} \cdot \boldsymbol{T}. \end{aligned} \tag{21}$$

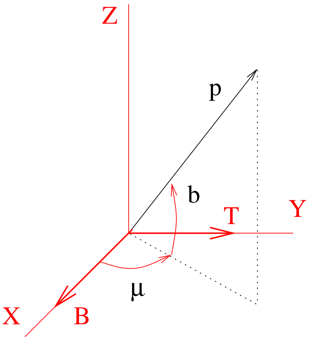

Figure 2. Coordinate system.

The Boltzmann equation for the regular components is then

$$\boldsymbol{u} \cdot (\boldsymbol{B_R} \times \nabla_u\, f_R) + \boldsymbol{u} \cdot \boldsymbol{T} = 0. \tag{22}$$

We can find consistent solutions when the correlation $\boldsymbol{T}$ is constant and orthogonal to $\boldsymbol{B}_R$. We place the axes (see Figure 2) so that $\boldsymbol{B}_R$ and $\boldsymbol{T}$ go along the x- and the y-axis, respectively, and we use the latitude b and the longitude μ to label the direction $\boldsymbol{u}$ of a CR. Taking $f_R(\boldsymbol{u}) = f_R(b, \mu)$ and

$$\nabla_u\, f_R = \frac{\partial f_R}{\partial b}\, \boldsymbol{u}_b + \frac{1}{\cos b}\, \frac{\partial f_R}{\partial \mu}\, \boldsymbol{u}_\mu, \tag{23}$$

with

$$\begin{aligned} \boldsymbol{u}_b &= -\sin b\, \cos\mu\, \boldsymbol{u}_\phi - \sin b\, \sin\mu\, \boldsymbol{u}_r + \cos b\, \boldsymbol{u}_z; \\ \boldsymbol{u}_\mu &= -\sin\mu\, \boldsymbol{u}_\phi + \cos\mu\, \boldsymbol{u}_r, \end{aligned} \tag{24}$$

the Boltzmann equation becomes

$$-\sin\mu\, \frac{\partial f_R}{\partial b} + \tan b\, \cos\mu\, \frac{\partial f_R}{\partial \mu} + \frac{T}{B_R}\, \cos b\, \sin\mu = 0. \tag{25}$$

This equation can be solved analytically:

$$f_R(b, \mu) = f_0 \left(1 + \frac{T}{f_0 B_R}\, \sin b\right) + \tilde{f}(\cos b\, \cos\mu), \tag{26}$$

with f_0 a constant and $\tilde{f}$ an arbitrary function of $\cos b\, \cos\mu$. We see that the first term is just a dipole orthogonal to the plane defined by $\boldsymbol{B}_R$ and $\boldsymbol{T}$, whereas the second term may include a dipole along $\boldsymbol{B}_R$:

$$f_R(b, \mu) = f_0(1 + t\, \sin b + s\, \cos b\, \cos\mu), \tag{27}$$

with $t = T/(f_0 B_R)$ and s a constant depending on boundary conditions. The CR flux that corresponds to this distribution function (see Equation (3)) would be

$$F_R(\boldsymbol{u}) = F_0\, (1 + (\boldsymbol{d}_t + \boldsymbol{d}_s) \cdot \boldsymbol{u}), \tag{28}$$

where $F_0 = f_0(E/c)^2$, $\boldsymbol{d}_t = -t\, \boldsymbol{u}_B \times \boldsymbol{u}_T$ and $\boldsymbol{d}_s = -s\, \boldsymbol{u}_B$. Equation (28) expresses a key result: the global CR *flow* $\boldsymbol{d}_R$ does not necessarily flow along the average magnetic field $\boldsymbol{B}_R$. There may appear a second dipole anisotropy orthogonal to $\boldsymbol{B}_R$ that, added to the first dipole, could favor any direction: $\boldsymbol{d}_R = \boldsymbol{d}_t + \boldsymbol{d}_s$. Moreover, the turbulent correlation $\boldsymbol{T}$ defining this second dipole may evolve with the energy and vary its direction, which would translate into a change in the global CR *flow* and then in the boundary conditions that determine the dipole anisotropy along $\boldsymbol{B}_{\rm IS}$ described above.

We would like to make some final observations concerning the evolution of the anisotropy with the energy. For a standard Kolmogorov spectrum of magnetic turbulences $\lambda_\parallel$ grows with the energy like $\approx E^{0.6}$ (Swordy 2001), whereas $\lambda_\perp \approx r_L$ increases linearly with the CR energy. When the parallel and the transverse mean free paths become similar, the propagation becomes isotropic and we should see the global CR *flow* (see Figure 2). This *flow*, in turn, should reflect the velocity of our local IS plasma and the position and the intensity of the average CR source. Moreover, the isotropic propagation would also be a sign that r_L has reached a size similar to the region of coherence of $\boldsymbol{B}_{\rm IS}$, since the fluctuations δB of wavenumber $k \approx 1/r_L$ should be $\delta B \approx B_{\rm IS}$.

3. SMALL- AND MEDIUM-SCALE ANISOTROPIES

A small-scale anisotropy in the CR flux must be generated closer to the Earth (Salvati 2010; Giacinti & Sigl 2012), at distances where the diffusive regime has not been fully established yet. It is then necessary to study the image of a point-like CR source after crossing a constant magnetic field, without the magnetic turbulences that cause the diffusion.

A particle of charge Q and energy $E \gg mc^2$ in a constant field $\boldsymbol{B}_{\rm IS} = B_{\rm IS}\,\boldsymbol{k}$ will describe a helix of angular frequency $\omega = B_{\rm IS} c Q/E$ and radius $r(\mu) = c\sqrt{1-\mu^2}/\omega$. Choosing the coordinates such that at $t = 0$ the particle is at $S = (0, 0, 0)$, the trajectory reads

$$
\begin{aligned}
x &= -r(\mu)\,\sin\phi_0 + r(\mu)\,\sin(\phi_0 + \omega\,t)\\
y &= r(\mu)\,\cos\phi_0 - r(\mu)\,\cos(\phi_0 + \omega\,t)\\
z &= c\,\mu\,t, \qquad (29)
\end{aligned}
$$

where $\mu = v_\parallel/c$ and ϕ_0 is the initial angle of $v_\perp$ with the x-axis:

$$
\begin{aligned}
\dot{x} &= c\,\sqrt{1-\mu^2}\,\cos(\phi_0 + \omega\,t)\\
\dot{y} &= c\,\sqrt{1-\mu^2}\,\sin(\phi_0 + \omega\,t)\\
\dot{z} &= c\,\mu. \qquad (30)
\end{aligned}
$$

Let us consider all the trajectories connecting the source S with an observer R located at a transverse distance $d_\perp \leqslant c/\omega = r_L$ and a paralel distance $d_\parallel \geqslant 0$. We can always rotate the axes so that R is at $(0, d_\perp, d_\parallel)$ and use the variables (μ, ϕ_0, t) to solve $(x, y, z) = (0, d_\perp, d_\parallel)$. It turns out that there are an infinite number of such trajectories, each one characterized by an integer *winding* number $n \geqslant n_{\rm min}$, with

$$
n_{\rm min} = \text{Integer}\left[\frac{d_\parallel}{\pi\sqrt{4r_L^2 - d_\perp^2}}\right], \qquad (31)
$$

and a (positive or negative) ϕ_0 with $|\phi_0| \leqslant \pi/2$. To see this, it is instructive to first consider the case with $d_\parallel = 0$ (in Figure 3), i.e., with S and R in a plane orthogonal to $\boldsymbol{B}_{\rm IS}$. The trajectories in this case have $\mu = 0$, $\phi_0^- = -\phi_0^+$ and will reach R after an arbitrary number n of turns around the left or the right circles in Figure 3. Notice that higher values of n correspond to longer trajectories, which will provide fainter images of S (the flux scales like $1/L^2$). Adding a distance $d_\parallel$ along the $\boldsymbol{B}_{\rm IS}$ direction, the trajectories will require a nonzero value of μ to reach R, with $L = d_\parallel/\mu$ their total length. Trajectories with larger values of μ will be brighter, although this parameter is bounded by the condition $r_L\sqrt{1-\mu^2} \geqslant d_\perp/2$.

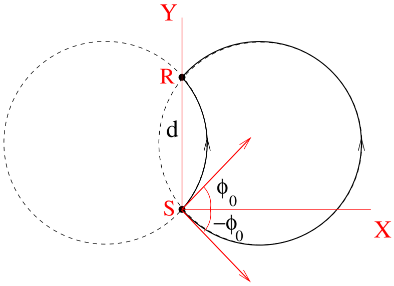

Figure 3. Trajectories between $S = (0, 0, 0)$ and $R = (0, d_\perp, 0)$ for $\boldsymbol{B}_{\rm IS} = (0, 0, B_{\rm IS})$.

In Figure 4 we plot several trajectories connecting S with R for a large ($d_\parallel = 35 r_L$) longitudinal distance. In the limit of very large $d_\parallel$ the trajectories arrive at R defining a semi-conus of directions of angle $\theta = \arccos d_\perp/(2r_L)$, with $-\pi/2 < \varphi < \pi/2$, and the limiting directions ($\varphi = \pm\pi/2$) defining the plane orthogonal to $\boldsymbol{B}_{\rm IS}$. It is easy to see that the trajectories with direction $\varphi = 0$ and maximum μ are shorter but less dense than the ones in the extremes. As a consequence, the brightness (number of trajectories per unit length times their flux) along the semicircle scales like

$$
\mathcal{B} = \mathcal{B}_0 \cos(\varphi + \pi/2)\,. \qquad (32)
$$

Notice also that each trajectory reaching R corresponds to a CR that left the source S at a different time, so the image at R would be the whole semicircle only for a constant and isotropic source.

Although from the previous analysis it is apparent that a nearby source could introduce small- and medium-scale anisotropies in the CR flux, we do not expect any sources at distances below 1 pc, which would probably introduce too large anisotropies. We find, however, another plausible mechanism for the generation of this type of anisotropy.

In Battaner et al. (2011) we have described the possible effects of a *cosmic magnetic lens*: a predominantly toroidal field configuration that may appear with a variety of sizes and magnetic strength. As deduced from Liouvilles theorem,[2] an isotropic and homogeneous flux will never become anisotropic due to the action of a magnetic field. However, the large-scale dipole anisotropy discussed in the previous section could cross a nearby field configuration acting as a magnetic lens and imply point-like anisotropies of the same order. The lens would then become equivalent to a faint source of CRs but be otherwise invisible, since it does not produce or deflect the light.

4. COMPARISON WITH THE DATA

SuperKamiokande, TIBET, ARGO-YBF, ANTARES, MILAGRO, and, more recently, HAWC have been able to distinguish from the northern sky an $O(0.1\%)$ large-scale anisotropy in the flux of 1–10 TeV CRs. IceTop and IceCube have observed

---

[2] This theorem, first applied to CRs moving inside a magnetic field in (Lemaître & Vallarta 1933), implies that an observer following a trajectory will always observe the same differential flux (or intensity, particles per unit area and solid angle) along the direction defined by that trajectory.

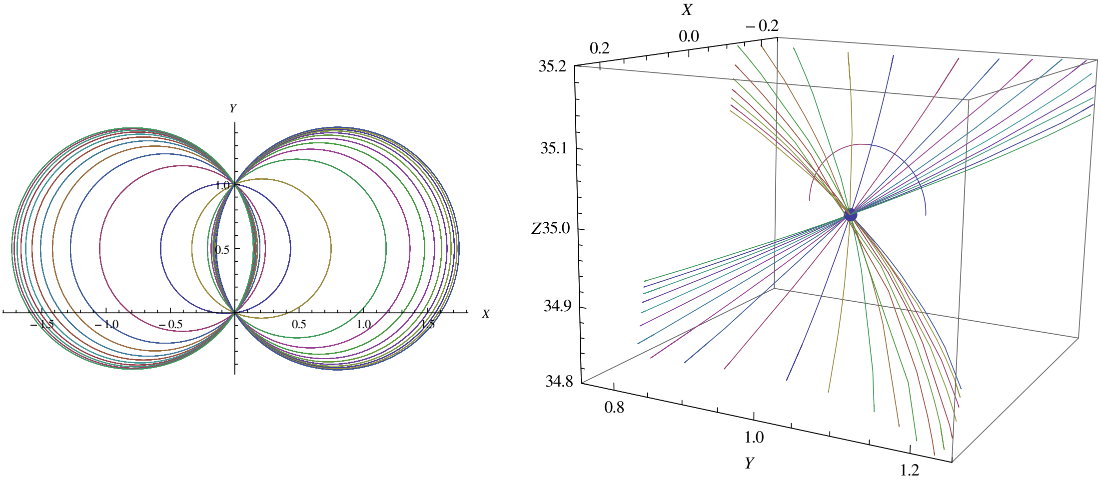

Figure 4. Twenty shortest trajectories between $S = (0, 0, 0)$ and $R = (0, 1, 35)$ for $\boldsymbol{B}_{\text{IS}} = (0, 0, B_{\text{IS}})$ and $r_L = 1$: projection on the x–y plane (left) and trajectories at R (right). In the limit $d_\parallel \gg d_\perp$ the source is *seen* at R as a semi-conus of angle $\theta = \arccos d_\perp/(2r_L)$ with its axis along x and the limiting directions ($\varphi = \pm\pi/2$) defining the x–y plane.

Table 1
Summary of Data on the Large-scale Anisotropy Obtained by Several Observatories: ARGO (Di Sciascio 2012), MILAGRO (Abdo 2009), TIBET (Amenomori et al. 2006), ICECUBE (Abbasi et al. 2012), ICETOP (Aartsen et al. 2013)

Hemisphere	Experiment	$\langle E \rangle$	Deficit Position		Amplitude
		[TeV]	R.A. [deg]	Decl. [deg]	
North	ARGO	3.6	170 to 210	−10 to 30	3×10^{-3}
	MILAGRO	6	180 to 220	−10 to 0	3×10^{-3}
	TIBET	6.2	170 to 210	−10 to 20	3×10^{-3}
	ARGO	24	150 to 190	−10 to 30	1×10^{-3}
	TIBET	300	···	···	$< 1 \times 10^{-3}$
South	ICECUBE	20	190 to 240	−30 to −60	8×10^{-4}
	ICECUBE	400	40 to 100	−15 to −45	7×10^{-4}
	ICETOP	400	70 to 110	−15 to −45	1.6×10^{-3}
	ICETOP	2000	50 to 125	−25 to −55	3×10^{-3}

with also very high statistics up to the PeV scale from the South Pole. In Table 1, we give an estimate of the results obtained in these experiments. It is remarkable that all the observations seem consistent with each other, although the higher energies seen at IceTop have not been accessible to the previous experiments or to HAWC yet. One should notice that each experiment can access all the right ascensions (α) but only a limited region of declinations (e.g., $-90^\circ < \delta < -25^\circ$ in IceCube). It becomes then difficult to estimate whether the excess and the defect in the flux are opposite to each other ($\alpha \to \alpha \pm 180^\circ$, $\delta \to -\delta$) and define a dipole. Actually, in most experiments the region of maximum excess or maximum defect is found at the limiting declinations that are accessible, suggesting that the *real* maximum is out of reach. If that is the case, the nonaccessible pole will introduce a relatively less intense and broader anisotropy than the pole that can be seen by the experiment.

The data can be summarized as follows. At 1–20 TeV it reveals a dipole anisotropy that goes along $\boldsymbol{B}_{\text{IS}}$. Taking all the data from the northern observatories and the low-energy IceCube results (based on the observation of atmospheric muons), we estimate

$$\ell_B = 180^\circ; \quad b_B = -60^\circ, \tag{33}$$

which is consistent with the values in Equations (4–5). In Figure 5 we plot in equatorial coordinates two cones of angle 30° with the axis along and opposite to the direction of this $\boldsymbol{B}_{\text{IS}}$. At higher energies the observations from the South Pole indicate that the anisotropy weakens, becoming of order 10^{-4}. This result is supported by TIBET (see Table 1) and, especially, by EAS-TOP (Aglietta et al. 2009), which at $E \approx 100$ TeV is able to *see* the movement of the Earth around the Sun (an anisotropy of amplitude 2×10^{-4}). At even higher energies (around 400 TeV) both EAS-TOP and IceCube detect an increase in the amplitude of the anisotropy and also a large change of phase, suggesting a dipole almost opposite to the initial one. Finally, at 2 PeV (Aartsen et al. 2013) the direction of the excess may have changed slightly toward the galactic center.

Our results in Section 2 provide a framework with which to interpret these observations. Above 1 TeV the effect of the heliosphere on the CR trajectories is subleading, and the dominant magnetic field is the $\boldsymbol{B}_{\text{IS}}$ in Equation (33). The modulation above 10 TeV can then be explained if the global CR flow varies its direction with the energy, in particular, if its component along $\boldsymbol{B}_{\text{IS}}$ changes sign at ≈100 TeV. At these energies other effects, like the Compton–Getting irregularities of order 10^{-4} due to the velocity of the Earth, become relatively important. As the CR energy grows, the possible misalignment of the anisotropy with $\boldsymbol{B}_{\text{IS}}$ would indicate that $r_L \approx R_{\text{IS}}$, where R_{IS} is the radius of coherence of the local IS magnetic field (see Figure 2). For $B_{\text{IS}} \approx 3\,\mu$G (Schwadron et al. 2014) and $E \approx 1$ PeV we obtain $R_{\text{IS}} \approx 0.3$ pc. The propagation then becomes isotropic (Casse et al. 2002), and the dipole anisotropy should follow the direction of the global CR *flow*, which is driven

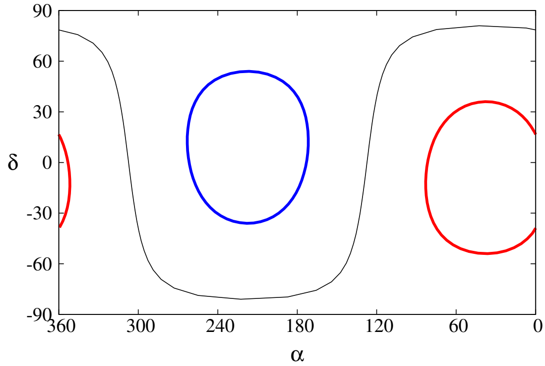

Figure 5. Dipole anisotropy along $\boldsymbol{B}_{\rm IS}$ for $\ell_B = 180^\circ$ and $b_B = -60^\circ$ in equatorial coordinates (right ascension and declination). The thin line indicates the magnetic equator, whereas thick lines define cones of angle $\pi/4$ along the magnetic axis.

by a correlation of turbulent quantities (at this scale, $\delta B = B_{\rm IS}$ and the fluctuation δf generated by the movement of our local IS cell relative to our neighbors) and by the average magnetic field B_R. The radius $R_{\rm IS} \approx 0.3$ pc of our local IS plasma could also be related to the appearance of the *knee* in the CR spectrum, as CRs of energy above 1 PeV could not be trapped by $B_{\rm IS}$ in our vicinity.

As for the low-scale anisotropies, we have described in Section 3 how the image of the dipole through a cosmic magnetic lens may introduce irregularities. These could consist of pointlike and/or longitudinal structures similar to the ones discovered by some experiments: the two regions observed by TIBET (Amenomori et al. 2006) and MILAGRO (Abdo et al. 2008) or the four regions (which include the two former regions) found by ARGO (Bartoli 2013). The lens could *focus* the CR wind (see Figure 1) and define anisotropies of order 5×10^{-4}, the amplitude that has been observed. Notice also that, since the effect of the magnetic lens on a more energetic CR will be smaller (Battaner et al. 2011), the irregularities will slightly change their position and finally disappear when the energy grows. We think that region 2 in Bartoli (2013)—region *B* in (Abdo et al. 2008)—could be related to the effect that we described (region 1, the most intense, seems linked to an effect of the heliotail; Lazarian & Desiati 2010).

5. SUMMARY AND DISCUSSION

The appearance of anisotropies in the flux of charged CRs provides information about the distribution of sources and about the magnetic plasma where they have propagated on their way to the Earth. The $O(10^{-3})$ deficit from north galactic regions discovered by TIBET and MILAGRO seems to follow the direction of $\boldsymbol{B}_{\rm IS}$. Using the Boltzmann equation, we have justified this observation and have shown that the CR *flow* at more global scales may modulate this anisotropy, reducing its intensity and even inverting its direction at higher energies. These features seem consistent with IceCube observations in the Southern Hemisphere. We have argued that a misalignment of the dipole anisotropy with $\boldsymbol{B}_{\rm IS}$ could be used to estimate the region of coherence of the local IS plasma. Although the appearance of anisotropies can also be understood using a diffusion equation, we think that our approach provides an alternative (and simpler) framework. In particular, the Boltzmann equation averaged over different scales provides a useful picture able to describe the changes in the anisotropy with the energy.

We have also suggested a mechanism that would relate the large- and the small-scale anisotropies: these would appear as the image of the global dipole provided by nearby cosmic magnetic lenses (Battaner et al. 2011), which would *focus* the CR flow. Notice that the lens acts as a CR source, but that the *real* source would be the large-scale anisotropy. In particular, if this is $O(0.1\%)$, then the low-scale anisotropy will be of the same order. If the lens is seen from the Earth under a sizable solid angle, the magnetic field $B_{\rm IS}$ can define linear structures like the ones described in (Bartoli 2013).

The simplified scheme proposed here uses a number of approximations: all CRs are protons (heavier nuclei of the same energy would have smaller r_L), all CRs in the same data set have equal energy, or the effect of the heliosphere (Lazarian & Desiati 2010) is negligible. We think, however, that it provides an acceptable qualitative description of the data. In the near future HAWC observations from the Northern Hemisphere could confirm that the TIBET/MILAGRO dipole is modulated and changes sign at energies above 100 TeV.

This work has been supported by MICINN of Spain (AYA2011-24728, FPA2010-16802, FPA2013-47836, Consolider-Ingenio *Multidark* CSD2009-00064, *EPI* CSD2010-00064) and by Junta de Andalucía (FQM101, FQM108, FQM3048).

REFERENCES

Aartsen, M. G., Abbasi, R., Abdou, Y., et al. 2013, ApJ, 765, 55
Abbasi, R., Abdou, Y., Abu-Zayyad, T., et al. 2012, ApJ, 746, 33
Abdo, A. A., Allen, B., Aune, T., et al. 2008, PhRvL, 101, 221101
Abdo, A. A., Allen, B. T., Aune, T., et al. 2009, ApJ, 698, 2121
Abeysekara, A. U., Alfaro, R., Alvarez, C., et al. 2013, in Proc. 33rd Int. Cosmic Ray Conf.
Aglietta, M., Alekseenko, V. V., Alessandro, B., et al. 2009, ApJL, 692, L130
Ahlers, M. 2014, PhRvL, 112, 021101
Amenomori, M., Ayabe, S., Bi, X. J., et al. 2006, Sci, 314, 439
Bartoli, B. 2013, , PhRvD, 88, 082001
Battaner, E. 2009, in Lecture Notes and Essays in Astrophysics III, ed. A. Ulla & M. Manteiga (Torculo: La Coruña)
Battaner, E., Castellano, J., & Masip, M. 2009, ApJL, 703, L90
Battaner, E., Castellano, J., & Masip, M. 2011, A&A, 527, 5
Beck, R. 2005, in Cosmic Magnetic Fields, ed. R. Wielebinski & R. Beck (Berlin: Springer), 41
Biermann, P. L., Becker, J. K., Seo, E.-S., & Mandelartz, M. 2013, ApJ, 768, 124
Casse, F., Lemoine, M., & Pelletier, G. 2002, PhRvD, 65, 023002
Compton, A. H., & Getting, I. A. 1935, PhRv, 47, 817
Di Sciascio, G., & Iuppa, R. Argo-Ybj Collaboration 2012, JPhCS, 375, 052008
Frisch, P. C., Andersson, B.-G., Berdyugin, A., et al. 2012, ApJ, 760, 106
Giacinti, G., Kachelriess, M., Semikoz, D. V., & Sigl, G. 2012, JCAP, 1207, 031
Giacinti, G., & Sigl, G. 2012, PhRvL, 109, 071101
Guillian, G., Hosaka, J., & Ishihara, K. 2007, PhRvD, 75, 062003
Han, J. L. 2009, in IAU Symp. 259, Cosmic Magnetic Fields: From Planets to Stars and Galaxies, ed. K. G. Strassmeier, A. G. Kosovichev, & J. E. Beckman (Cambridge: Cambridge Univ. Press), 455
Iuppa, R. 2012, Frascati Phys. Ser., 55, 61
Jones, F. C. 1990, ApJ, 361, 162
Lazarian, A., & Desiati, P. 2010, ApJ, 722, 188
Lemaître, G., & Vallarta, M. 1933, PhRv, 43, 89
Mangano, S. 2009, in Proc. 31st Int. Cosmic Ray Conf.
McComas, D., Alexashov, G., Bzowski, D. J., et al. 2012, Sci, 336, 1221054
Pohl, M., & Eichler, D. 2013, ApJ, 766, 4
Qu, X.-B., Zhang, Y., Xue, L., Liu, C., & Hu, H.-B. 2012, ApJL, 750, L17
Ratkiewicz, R., Ben-Jaffel, L., & Grygorczuk, J. 2008, GeoRL, 35, L23105
Reeves, H., Fowler, W. A., & Hoyle, F. 1970, Natur, 226, 727

Ruiz-Granados, B., Rubino-Martin, J. A., & Battaner, E. 2010, A&A, 522, A73
Salvati, M. 2010, A&A, 513, A28
Santander, M. 2013, Nucl. Instrum. Meth. A, 725, 85
Schwadron, N. A., Adams, F. C., Christian, E. R., et al. 2014, Sci, 343, 988
Shalchi, A. 2009, Nonliner Cosmic Ray Diffusion Theories (Berlin: Springer)
Swordy, S. P. 2001, SSRv, 99, 85
Wielebinski, R. 2005, in Cosmic Magnetic Fields ed. R. Wielebinski & R. Beck (Berlin: Springer)
Zotov, M. Y., & Kulikov, G. V. 2012, AstL, 38, 731

Astronomy & Astrophysics manuscript no. aa3
November 26, 2010

Cosmic Magnetic Lenses

Eduardo Battaner, Joaquín Castellano, Manuel Masip

Departamento de Física Teórica y del Cosmos Universidad de Granada, E-18071 Granada, Spain
e-mail: `battaner@ugr.es, jcastellano@ugr.es, masip@ugr.es`

Received

ABSTRACT

Context. Magnetic fields play a critical role in the propagation of charged cosmic rays. Particular field configurations supported by different astrophysical objects may produce images on cosmic ray maps.
Aims. We consider a simple configuration, a constant azimuthal field in a disk-like object, that we identify as a *cosmic magnetic lens*. Such configuration is typical in most spiral galaxies, and we assume that it can also appear at smaller or larger scales.
Methods. We show that the magnetic lens deflects cosmic rays in a regular geometrical pattern, very much like a gravitational lens deflects light but with some interesting differences. In particular, the lens acts effectively only in a definite region of the cosmic-ray spectrum, and it can be convergent or divergent depending on the (clockwise or counterclockwise) direction of the magnetic field and the (positive or negative) electric charge of the cosmic ray.
Results. We find that the image of a point-like monochromatic source may be one, two or four points depending on the relative position of source, observer and center of the lens. For a perfect alignment and a lens in the orthogonal plane the image becomes a ring. We also show that the presence of a lens could introduce low-scale fluctuations and matter-antimatter asymmetries in the fluxes from distant sources.
Conclusions. The concept of cosmic magnetic lens that we introduce here may be useful in the interpretation of possible patterns observed in the cosmic ray flux at different energies.

Key words. Galactic magnetic fields, cosmic rays

1. Introduction

High-energy cosmic rays carry information from their source and from the medium where they have propagated in their way to the Earth. They may be charged particles (protons, nuclei or electrons) or neutral (photons and neutrinos). The main difference between these two types of astroparticles is that the first one loses directionality through interactions with galactic and intergalactic magnetic fields. In particular, random background fields of order $B \approx 1\,\mu$G in our galaxy will uncorrelate a particle from its source after a distance larger than

$$r_g = \frac{E}{ecB} \approx \frac{E}{1\text{ TeV}} \times 10^{-3}\text{ pc}\,, \tag{1}$$

where e is the unit charge and E the energy of the particle. As E grows the reach of charged particles increases, extending the distance where they may be used as astrophysical probes. At $E \approx 10^9$ GeV this distance becomes 1 Mpc, and cosmic rays may bring information from an extragalactic source. Of course, it seems difficult to imagine a situation where charged cosmic rays may be used to *reveal* or characterize an object. In this letter we propose that they can detect the presence of an astophysical object, *invisible* to high-energy photons and neutrinos, that we name as *cosmic magnetic lens* (CML).

The term *magnetic lensing* has already been used in the astrophysical literature to describe, generically, the curved path of charged cosmic rays through a magnetized medium. Harari et al. 2001, 2005, 2010 studied the effect of galactic fields, showing that they may produce magnification, angular clustering and caustics. Dolag et al. 2009 considered lensing by the tangled field of the Virgo cluster, assuming that the galaxy M87 was the single source of ultrahigh energy cosmic rays. Shaviv et al. 1999 studied the lensing near ultramagnetized neutron stars. Our point of view, however, is different. The CML will be defined by a basic magnetic-field configuration with axial symmetry that could appear in astrophysical objects at any scale: from clusters of galaxies to planetary systems. The effect of the CML on galactic cosmic rays (*i.e.*, charged particles of energy $E < 10^9$ GeV) will not be significantly altered by turbulent magnetic fields if the lens is within the distance r_g in Eq. (1) and its magnetic field is substantially stronger than the average background field between its position and the Earth. Since the CML is a definite object, we can separate source, magnetic lens and observer. Although it is not a lens in the geometrical optics sense (the CML does not have a focus), its effects are generic and easy to parametrize, analogous to the ones derived from a gravitational lens (with no focus neither).

2. A magnetic lens

The basic configuration that we will consider is an azimuthal mean field $\boldsymbol{B}$ in a disc of radius R and thickness D. The field lines are then circles of radius $\rho \leq R$ around the disk axis. As a first approximation we will take a constant intensity B, neglecting any dependence on ρ (notice, however, that a more realistic B should vanish smoothly at $\rho = 0$ and be continuous at $\rho = R$). Our assumption will simplify the analysis while providing all the main effects of a magnetic lens. The disk of most spiral galaxies has a large toroidal component of this type (Beck 2005), so they are obvious candidates to CML. The configuration describing the CML would be natural wherever there is ionized gas in a region with turbulence, differential rotation and axial symmetry, since in such environment the magnetic field tends to be ampli-

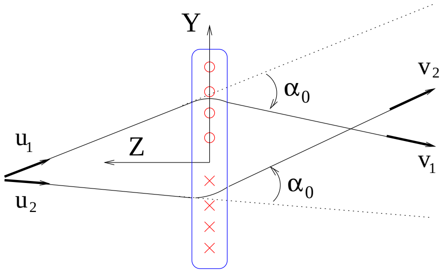

Fig. 1. Trajectories in the $x = 0$ plane. $\boldsymbol{B} \propto (1, 0, 0)$ at $y > 0$ and $\boldsymbol{B} \propto (-1, 0, 0)$ at $y < 0$.

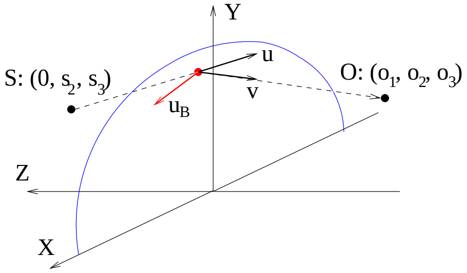

Fig. 2. Trajectory from the source to the observer.

fied by the *dynamo effect* (Parker 1971, Brandenburg et al. 2005). We will then assume that it may appear at any scale R with an arbitrary value of B.

Let us parametrize the magnetic field and its effect on a charged cosmic ray. If the lens lies in the XY plane with the center at the origin (see Fig. 1) $\boldsymbol{B}$ is[1]

$$\boldsymbol{B} = \begin{cases} \dfrac{B}{\rho}\,(y, -x, 0) & \text{if } \rho < R \text{ and } |z| < \dfrac{D}{2}\ ; \\ 0 & \text{otherwise ,} \end{cases} \tag{2}$$

with $\rho \equiv \sqrt{x^2 + y^2}$. To understand its effect, we will first consider a particle moving in the YZ ($x = 0$) plane with direction $\boldsymbol{u}$ (the case depicted in Fig. 1). When it enters the lens the cosmic ray finds an orthogonal magnetic field that curves its trajectory. The particle then rotates clockwise[2] around the axis $\boldsymbol{u}_B = \boldsymbol{B}/B$, describing a circle of gyroradius $r_g = E/(ecB)$. The segment of the trajectory inside the lens has a length $l \approx D$, so the total rotation angle α_0 when it departs is

$$\alpha_0 \approx \frac{ecBD}{E}\ . \tag{3}$$

The direction of the particle after crossing the lens is then $\boldsymbol{v} = R_B(\alpha_0)\ \boldsymbol{u}$. The angle α_0 will be the only parameter required to describe the effect of this basic lens. An important point is that $\boldsymbol{B}$ and the Lorentz force change sign if the trajectory goes through $y < 0$. In that case the deflection is equal in modulus but opposite to the one experience by particles going through $y > 0$ (see Fig. 1). Therefore, the effect of this lens is *convergent*, all trajectories are deflected the same angle α_0 towards the axis of the lens. Notice that the lens changes to *divergent* for particles of opposite electric charge or for particles reaching the lens from the opposite ($z < 0$) side.

The effect on a generic trajectory within a plane not necessarily orthogonal to the lens is a bit more involved. It is convenient to separate

$$\boldsymbol{u} = \boldsymbol{u}_{\parallel} + \boldsymbol{u}_{\perp}\ ; \quad \boldsymbol{v} = \boldsymbol{v}_{\parallel} + \boldsymbol{v}_{\perp}\ , \tag{4}$$

where $\boldsymbol{u}_{\parallel} = (\boldsymbol{u}\cdot\boldsymbol{u}_B)\ \boldsymbol{u}_B$ and $\boldsymbol{u}_{\perp} = \boldsymbol{u} - \boldsymbol{u}_{\parallel}$ are parallel and orthogonal to the magnetic field, respectively (and analogously for $\boldsymbol{v}$). In this case the magnetic field will rotate the initial direction $\boldsymbol{u}$ an angle of $\alpha = u_{\perp}\alpha_0$ around the axis $\boldsymbol{u}_B$: $\boldsymbol{v} = R_B(u_{\perp}\alpha)\ \boldsymbol{u}$. This means that the parallel components of the initial and the final directions coincide,

$$u_{\parallel} = \boldsymbol{u}\cdot\boldsymbol{u}_B = v_{\parallel}\ , \tag{5}$$

whereas the orthogonal component $\boldsymbol{u}_{\perp}$, of modulus $u_{\perp} = \sqrt{1 - (\boldsymbol{u}\cdot\boldsymbol{u}_B)^2}$, rotates into

$$\boldsymbol{v}_{\perp} = \cos(u_{\perp}\alpha_0)\ \boldsymbol{u}_{\perp} - \sin(u_{\perp}\alpha_0)\ \boldsymbol{u}_B \times \boldsymbol{u}_{\perp}\ . \tag{6}$$

An important observation concerns the *chromatic aberration* of the lens. The deviation α_0 caused by a given CML is proportional to the inverse energy of the cosmic ray. If E is small and $\alpha_0 > \pi/2$, then the lens acts *randomly* on charged particles, diffusing them in all directions. On the other hand, if E is large the deviation becomes small and is smeared out as the particle propagates to the Earth. Only a region of the cosmic-ray spectrum can *see* the CML.

3. Image of a point-like source

Let us now study the image of a localized monochromatic source produced by the CML. We will consider a *thin* lens ($R \gg D$) located on the plane $z = 0$ (see Fig. 2). Its effect on a cosmic ray can be parametrized in terms of the angle α_0 given in Eq. (3). The rotation axis is

$$\boldsymbol{u}_B = \frac{1}{\sqrt{x^2 + y^2}}(y, -x, 0)\ , \tag{7}$$

and the coordinates of source and observer are $S = (s_1, s_2, s_3)$ and $O = (o_1, o_2, o_3)$, respectively. We will use the axial symmetry of the lens to set $s_1 = 0$. The trajectory will intersect the CML at $(x, y, 0)$. There the initial direction $\boldsymbol{u}$ will change to $\boldsymbol{v}$, with

$$\boldsymbol{u} = \frac{(x, y - s_2, -s_3)}{\sqrt{x^2 + (y - s_2)^2 + s_3^2}}\ , \quad \boldsymbol{v} = \frac{(o_1 - x, o_2 - y, o_3)}{\sqrt{(o_1 - x)^2 + (o_2 - y)^2 + o_3^2}}\ . \tag{8}$$

Therefore, given a source S, an observer O and a lens producing a deviation α_0, we can determine the coordinates $(x, y, 0)$ where the rotation $R_B(u_{\perp}\alpha)$ described in the previous section exactly transforms $\boldsymbol{u}$ into $\boldsymbol{v}$. The first condition on x and y, given in Eq. (5), is that $\boldsymbol{B}$ does not change the longitudinal component of the velocity,

$$\boldsymbol{u}\cdot\boldsymbol{u}_B = \boldsymbol{v}\cdot\boldsymbol{u}_B\ . \tag{9}$$

---

[1] A continuous field configuration could be modelled just by adding a factor of $(1 - \exp[(\rho/\rho_0)^{n_0}]) \times \exp[(\rho/R)^{n_R}] \times \exp[(2z/D)^{n_D}]$. When the integers n_0, n_R and n_D are chosen very large and ρ_0 very small we recover our disc with a null B at $\rho = 0$.

[2] We define a positive deviation α_0 if the rotation from $\boldsymbol{u}$ to $\boldsymbol{v}$ around the axis $\boldsymbol{u}_B$ is clockwise.

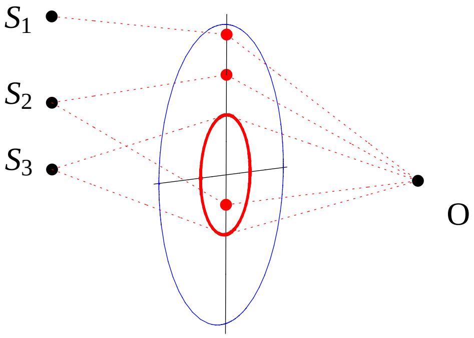

Fig. 3. Trajectories with $\beta > \alpha$ (S_1), $\beta < \alpha$ (S_2) and $\beta = 0$ (S_3) for an observer at the axis.

The second one, derived from Eq. (6), defines the rotation of $\boldsymbol{u}_\perp$ produced by the magnetic field. It can be written ($u_\perp = |\sin\widehat{\boldsymbol{uB}}|$)

$$\frac{\boldsymbol{v}_\perp \cdot \boldsymbol{u}_\perp}{u_\perp^2} = \cos\,(u_\perp \alpha_0)\,,$$
$$\frac{\boldsymbol{v}_\perp \cdot (\boldsymbol{u}_\perp \times \boldsymbol{u}_B)}{u_\perp^2} = \sin\,(u_\perp \alpha_0)\,. \qquad (10)$$

The second equation above is necessary to fully specify the rotation. Notice that $\alpha = u_\perp \alpha_0$ has a definite sign: positive for a convergent CML and negative for a divergent one. In addition, the solution must verify that $x^2 + y^2 < R^2$.

We find that for $R \to \infty$ and a convergent lens there is always at least one solution, whereas for a divergent one there is a region around the axis that my be *hidden* by the CML (this region disappears if B goes smoothly to zero at the center of the lens). To illustrate the different possibilities in Fig. 3–left we have placed the observer in the axis at a distance L from the lens, $O = (0, 0, -L)$, and have parametrized the position of the source (at a distance d from the lens) as $S = (0, d\sin\beta, d\cos\beta)$. In this case $u_\| = 0 = v_\|$ and $u_\perp = 1$. If the lens is convergent ($\alpha_0 > 0$) and $|\beta| > \alpha_0$, then the image of the source is just a single point. For a source at $|\beta| < \alpha_0$ we obtain two solutions, which correspond to trajectories from above or below the center of the lens. For a source in the axis ($\beta = 0$) the solution is a ring of radius

$$r = \frac{d+L}{2\tan\alpha_0}\left(\sqrt{1 + \frac{4dL\tan^2\alpha_0}{(d+L)^2}} - 1\right)\,. \qquad (11)$$

If the observer is located out of the axis but still in the $x = 0$ plane the possibilities are similar, but the ring becomes a *cross* similar to the one obtained through gravitational lensing. Finally, if we take the observer out of the $x = 0$ plane there appears always a single solution.

4. Fluxes from distant sources

Let us finally explore how the presence of a CML changes the flux F of charged particles from a localized source S. It is instructive to consider the case where S is a homogeneous disk of radius R_S placed at a distance d from the lens and the observer O is at a large distance L,

$$R_s < d, R \ll L\,, \qquad (12)$$

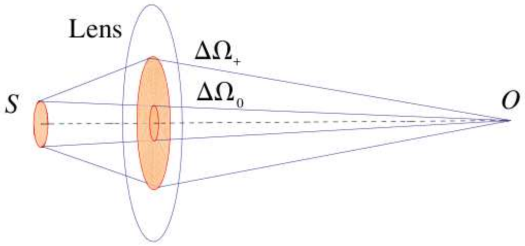

Fig. 4. Cone of trajectories from S to O with and without lens for a homogeneous and monochromatic source.

as shown in Fig. 4. In addition, we will assume that the magnetic field defining the lens goes smoothly to zero near the axis, and that the source is monochromatic.

If there were no lens, O would see S under a solid angle

$$\Delta\Omega_0 \approx \pi\frac{R_S^2}{L^2}\,. \qquad (13)$$

If all the points on S are equally bright and the emission is isotropic, the differential flux $\mathrm{d}F/\mathrm{d}\Omega$ from all the directions inside the cone $\Delta\Omega_0$ will be approximately the same, implying a total flux (number of particles per unit area)

$$F_0 = \int_{\Delta\Omega_0} \mathrm{d}\Omega\,\frac{\mathrm{d}F}{\mathrm{d}\Omega} \approx \pi\frac{R_S^2}{L^2}\frac{\mathrm{d}F}{\mathrm{d}\Omega}\,. \qquad (14)$$

The lens in front of S will deflect an approximate angle α all trajectories crossing far from the axis. In Fig. 4 we have pictured[3] the limiting directions reaching the observer, that define a cone

$$\Delta\Omega_+ \approx \pi\frac{(R_S + d\,\tan\alpha)^2}{L^2}\,. \qquad (15)$$

O sees now cosmic rays from directions inside the larger cone $\Delta\Omega_+$ or, in other words, sees the radius R_S of the source *amplified* to $R_S + d\,\tan\alpha$.

We can then use Liouville's theorem to deduce how the flux observed by O is affected by the presence of the lens. This theorem, first applied to cosmic rays moving inside a magnetic field by Lemaitre and Vallarta 1933, implies that an observer following a trajectory will always observe the same differential flux (or intensity, particles per unit area and solid angle) along the direction defined by that trajectory. For example, in the case with no lens an observer in the axis at a distance $L' \gg L$ will still observe the same differential flux $\mathrm{d}F/\mathrm{d}\Omega$. However, the cone of directions that he sees will be smaller, $\Delta\Omega'_0 \approx \pi R_S^2/L'^2$, and the total flux from that source will scale like $F' \approx F\,L^2/L'^2$. The effect of the lens is then just to change the cone of directions reaching O from S, without changing the differential flux. This implies an integrated flux

$$F_+ \approx F_0\frac{\Delta\Omega_+}{\Delta\Omega_0} \approx F_0\left(1 + \frac{d^2\,\tan^2\alpha}{R_S^2}\right)\,. \qquad (16)$$

---

[3] A pointlike source in the axis is transformed by the lens into a ring, as explained in Section 4. As the source grows, the ring becomes thicker and eventually closes to a circle, which is the case considered in Fig. 4.

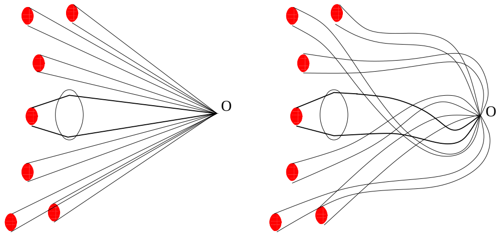

Fig. 5. Trajectories from S to O without (left) and with (right) irregular magnetic fields along the trajectory.

An important point is that the solid angle intervals $\Delta\Omega_{0,+}$ will in general be much smaller than the angular resolution at O. As a consequence, an observer trying to measure a differential flux will always include the whole cone $\Delta\Omega_{0,+}$ within the same solid angle bin: only the integrated fluxes $F_{0,+}$ (averaged over the angular resolution) are observable.

Now let us suppose that there are many similar sources at approximately the same distance from the observer and covering a certain range of directions. Cosmic rays emitted from each source will reach O within a very tiny cone $\Delta\Omega_0$, and will be observed integrated over that cone and averaged over the angular resolution. If one of the sources has in front a CML, its cone $\Delta\Omega_+$ at O and thus its contribution to one of the direction bins will be larger, what would translate in a low-scale anisotropy[4] within the range of directions covered by the sources (see Fig. 5, left).

In principle, this effect would not be erased by irregular magnetic fields from the source to the observer, that deflect the trajectories and tend to *isotropize* the fluxes (in Fig. 5, right). The contribution from the source behind the CML (reaching now O from a different direction) will still tend to be larger. The effect of the lens is to increase the *size* R_S of the source to $R_S + d\tan\alpha$; random magnetic fields will change the direction of arrival and the effective distance between S and O (*i.e.*, the direction and the size of the cone from each source), but not the initial deflection produced by the lens nor (by Liouville's theorem) the differential flux within each tiny cone. Therefore, the cone from the source behind the lens tends to be larger, and when integrated and averaged over the resolution bin may still introduce a low-scale anisotropy. The effect, however, tends to vanish if the cones are so small that the probability to observe two particles from the same cone of directions is smaller than the probability to observe particles from two disconnected cones with origin in the same source (*i.e.*, in the deep diffuse regime where trajectories become random walks).

Finally, note that the effect of a divergent CML would be just the opposite. The presence of a lens could then introduce an excess for positive charged particles and a deffect for the negative ones (or a matter–antimatter asymmetry if both species were equally emitted by S).

5. Summary and discussion

It is known that galactic and intergalactic magnetic fields play a very important role in the propagation of charged cosmic rays. Here we have explored the effect of a very simple configuration, a constant azimuthal field in a thin disk, that we identify as a CML. Such object acts on cosmic rays *like* a gravitational lens on photons, with some very interesting differences. Gravitational lenses are always convergent, whereas if a magnetic lens is convergent for protons and positrons, it changes to divergent for antiprotons and electrons. In addition, the deflection that the CML produces depends on the particle energy, so the lense is only visible in a very definite region (around one decade of energy) of the spectrum.

Our intention has been to introduce the concept of CML and discuss its possible effects leaving the search for possible candidates for future work. Generically, the magnetic-field configuration defining the CML is *natural* and tends to be established by the dynamo effect. For example, in spiral galaxies $\boldsymbol{B}$ can be pure azimuthal (the one we have assumed), axisymmetric spiral or bisymmetric spiral, with or without reversals (Beck 2005, Battaner et al. 2008), but in all cases the azimuthal component dominates. Our galaxy is not an exception (Han 2010, Ruiz et al. 2009), it includes in the disk a spiral magnetic field of $B \approx 4\,\mu$G. This would actually force that any analysis of magnetic lensing by other galaxies must *subtract* the effect produced by our own magnetic field. CMLs could also be present in galactic halos, as there are observations of polarized synchrotron emission suggesting the presence of regular fields (Dettmar et al. 2006). Analogous indications (Bonafede et al. 2009) can be found for larger structures, like clusters and their halos. Inside our galaxy, the antisymmetric tori placed 1.5 kpc away in both hemispheres discovered by Han et al. (1997) would also produce magnetic lensing on ultrahigh energy cosmic rays. At lower scales (20–800 pc) molecular clouds and HII regions (Gonzalez et al. 1997) are also potential candidates. Molecular clouds have strong regular fields in the range of 0.1–3 mG (Crutcher 2005). Moreover, many reversals in the field direction observed in our galaxy seem to coincide with HII regions (Wielebinski 2005), which would indicate that the field follows the rotation velocity in that region. There are also observations of Faraday screens covering angles of a few minutes of unknown origin (Mitra et al. 2003). Finally, nearby protostellar disks may provide a magnetic analogous of the gravitational microlenses, as they define small objects of $\approx 10^3$ AU diameter with azimuthal magnetic fields (Stepinski 1995) of order tens of mG (Goncalves et al. 2008). Therefore, we think it is justified to presume that CMLs may appear at any scales R with different values of B.

The lensing produced by a CML will be affected by the turbulent magnetic fields, but under certain conditions they should remain observable. For example, the typical lensing produced by a galaxy on cosmic rays of energy above 10^9 GeV is caused by a regular magnetic field of order μG, while the distortions will come from fluctuations of the same order. The region of coherence of these magnetic fluctuations, however, is just around 10–100 pc, varying randomly from cell to cell. Since the regular field that define the lens will act along distances 10–100 times larger, its effect on cosmic rays will dominate, and the expected *blurring* due to turbulences will be small. For CMLs inside our galaxy one should in general *subtract* the effect due to the local field at the relevant scale. Suppose, for example, that we have a small lens ($D \approx 10^{-3}$ pc) with a strong magnetic field ($B \approx 1$ mG) at a distance below 10 pc from the Earth. If the magnetic field along the trajectory from the lens to the Earth is of order μG (with weaker turbulences at smaller scales) then the effects of the lens on 10^6 GeV cosmic rays can be observed, but from a displaced direction. In any case, the identification of a CML

---

[4] The direction of the source would be measured with a gaussian distribution that could take it to adjacent bins.

would require a detailed simulation including a full spectrum of magnetic turbulences.

We have studied the image of a point-like source, finding interesting patterns that are the analogous of the gravitational Einstein's ring and Einstein's cross. Here the effect would be combined with a strong *chromatic* dependence, as the deviation is proportional to the inverse energy of the particle. The images would be absent (or placed in a different location) for particles of opposite charge, since they would find a divergent lens. We have also studied the effect of a CML on the flux from a localized source. If the source and the lens are far from the observer (*i.e.*, if it covers a small solid angle) it seems possible to generate small-scale anisotropies.

Acknowledgments

This work has been funded by MICINN of Spain (AYA2007-67625-CO2-02, FPA2006-05294, FPA2010-16802, and Consolider-Ingenio **Multidark** CSD2009-00064) and by Junta de Andalucía (FQM-101/108/437/792).

References

Battaner, E. et al. 2008, in *Lecture Notes and Essays in Astrophysics*, Vol. 3, 83–102.
Beck, R. 2005, in *Cosmic Magnetic Fields*, p. 41. Springer Verlag, Ed. by R. Beck and R. Wielebinski.
Bonafede, A., Feretti, L., Giovannini, G. 2009, Astron. Astrophys. 503, 707.
Brandenburg, A., Subramanian, K. 2005, Phys. Rep. 417, 1.
Crutcher, R. M. 2005, in *Magnetic Fields in the Universe: from Laboratory and Stars to the Primordial Structures*. Ed. by E.M. de Gouveia dal Pino et al. AIP Conf. Proc. 784, 129.
Dettmar, R.J., Soida, M. 2006, Astron. Nachr. 327, 495.
Dolag, K., Kachelriess, M., Semikoz, D.V. 2009, JCAP 0901, 033.
Goncalves, J., Galli, D., Girart, J.M. 2008, Astron. Astrophys. 490, 39.
González-Delgado, R. and Pérez, E. 1997, ApJ SS 108, 1.
Han, J.L., Manchester, R.N., Berkhuijsen, E.M., Beck, R. 1997, Astron. Astrophys. 352, 98.
Han, J.L. 2009, in *Cosmic magnetic fields: from planets to stars and galaxies*, IAU Conf. Proc. 259, 455.
Harari, D., Mollerach, S., Roulet, E. 2005, in *Observing ultrahigh energy cosmic rays from space and Earth*, AIP Conf. Proc. 566, 289.
Harari, D., Mollerach, S., Roulet, E. 2005, in *Magnetic Fields in the Universe: from Laboratory and Stars to Primordial Structures*, AIP Conf. Proc. 784, 763.
Harari, D., Mollerach, S., Roulet, E. 2010, *Effects of the galactic magnetic field upon large scale anisotropies of extragalactic cosmic rays*, arXiv:1009.5891.
Lemaitre, G. and Vallarta, M.S. 1933, Phys. Rev. 43, 87.
Mitra, D., Wielebinski, R., Kramer, M. and Jessner, A. 2003, Astron. Astrophys. 398, 993.
Parker, E. 1971, Astrophys. J. 163, 279.
Ruiz-Granados, B., Rubiño-Martín, J.A., Battaner, E. 2009, in *Cosmic magnetic fields: from planets to stars and galaxies*, IAU Conf. Proc. 259, 573.
Shaviv, N.J., Heyl, J.S., Lithwick, Y. 1999, Mon. Not. Roy. Astron. Soc. 306, 333.
Stepinski, T.F. 1995, Rev. Mex. Astron. Astrophys. 1, 267.
Wielebinski, R. 2005, in *The Magnetized Plasma in Galactic Evolution*. Proc. Conference. Ed. By K Chyzy et al. Jagiellonian Univ. Krakow. p. 125.

The Astrophysical Journal, 703:L90–L93, 2009 September 20 doi:10.1088/0004-637X/703/1/L90

GALACTIC MAGNETIC FIELDS AND THE LARGE-SCALE ANISOTROPY AT MILAGRO

Eduardo Battaner, Joaquín Castellano, and Manuel Masip
Departamento de Física Teórica y del Cosmos, Universidad de Granada, E-18071 Granada, Spain; battaner@ugr.es, jcastellano@correo.ugr.es, masip@ugr.es
Received 2009 July 16; accepted 2009 August 25; published 2009 September 4

ABSTRACT

The air-shower observatory Milagro has detected a large-scale anisotropy of unknown origin in the flux of TeV cosmic rays. We propose that this anisotropy is caused by galactic magnetic fields and, in particular, that it results from the combined effects of the regular and the turbulent (fluctuating) magnetic fields in our vicinity. Instead of a diffusion equation, we integrate Boltzmann's equation to show that the turbulence may define a *preferred* direction in the cosmic ray propagation that is orthogonal to the local regular magnetic field. The approximate dipole anisotropy that we obtain explains Milagro's data well.

Key words: cosmic rays – ISM: magnetic fields – solar neighborhood

1. INTRODUCTION

High-energy cosmic rays are of great interest in astrophysics, as they provide a complementary picture of the sky. When they are neutral particles (photons or neutrinos), they carry direct information from their source (Weekes, 2008; Voelk & Bernloehr 2009; Achterberg et al. 2006). During the past 30 years, gamma rays, in particular, have revealed a large number of astrophysical sources (quasars, pulsars, blazars) in our Galaxy and beyond. In contrast, when they are charged particles (protons, electrons, and atomic nuclei) cosmic rays lose directionality due to interactions with the μG magnetic fields that they face along their trajectory (Strong et al. 2007). In this case, however, they bring important information about the environment where they have propagated. For example, the simple observation that Boron is abundant in cosmic rays while rare in solar system nuclei is a very solid hint that cosmic rays have crossed around 10 g cm^{-2} of interstellar (baryonic) matter before they reach the Earth.

A very remarkable feature in the proton and nuclei fluxes is its isotropy. It is thought that cosmic rays of energy below 10^6 GeV are mainly produced in supernova explosions, which are most frequent in the galactic arms. We observe, however, that they reach us equally from all directions. This can only be explained if their trajectories are close to the random walk typical of a particle in a *gas*, and galactic magnetic fields seem the key ingredient in order to justify this picture.

Galactic magnetic fields have been extensively reviewed in the literature (Beck 2004, 2005; Wielebinski 2005; Han 2009; Battaner 2009). It is known that there is an average magnetic field of order

$$B_{\text{galactic}} \approx 3\ \mu\text{G} \qquad (1)$$

at galactic scales. This component is the background to a second component of strength

$$B_{\text{random}} \approx 3\text{–}5\ \mu\text{G} \qquad (2)$$

that is regular within cells of 10–100 pc but changes randomly from cell to cell. These magnetic fields have frozen-in field lines and are very affected by the compressions and expansions of the interstellar medium produced by the passage of spiral arm waves. A 10 TeV cosmic proton would move inside a 5 μG field with a gyroradius of

$$r_g = \frac{p}{eB} \approx 2 \times 10^{-3}\ \text{pc}\ , \qquad (3)$$

which is much smaller than the typical region of coherence. Therefore, this proton *sees* the superposition of both components as a regular magnetic field:

$$\vec{B}_{\text{galactic}} + \vec{B}_{\text{random}} = \vec{B}_{\text{regular}} \equiv \vec{B}\ . \qquad (4)$$

Note that the determination of the galactic field using *WMAP* data (Page et al. 2007; Jansson et al. 2009; Ruiz-Granados et al. 2009) gives $\vec{B}_{\text{galactic}}$. In contrast, estimates from Faraday rotations of pulsars would be sensitive to the same regular $\vec{B}$ that affects the cosmic proton. According to Han and collaborators (Han et al. 1999; Han 2009), the local $\vec{B}$ should be nearly contained in the galactic plane and clockwise as seen from the north galactic pole (i.e., following the direction of the disk rotation), although with a small vertical component or *tilt* angle.

At these small scales, the 10 TeV proton is *diffused* by scattering on random fluctuations in the magnetic field

$$\delta B \ll B\ . \qquad (5)$$

The interaction is of resonant character, so that the particle is predominantly scattered by those irregularities of the magnetic field of wavenumber $k \approx 1/r_g$. Estimates from the standard theory of plasma turbulence (Casse et al. 2002) that δB falls as a power law for larger wavenumbers (Han 2009), so this component is smaller than the regular B.

In this Letter, we argue that the detailed observation of the TeV cosmic-ray flux obtained by Milagro (Abdo et al. 2008, 2009) also may provide valuable information about $\vec{B}$ and δB. In particular, the analysis of over 10^{11} air showers has produced a map of the sky showing a large-scale anisotropy (a north galactic deficit) of order 10^{-3}. This map, which is consistent with previous observations (Aglietta et al. 1996; Amenomori et al. 2006), remains basically unexplained. Abdo et al. have discussed several possible origins:

(i) The Compton–Getting (CG) effect (Compton & Getting 1935), a dipole anisotropy that arises due to the motion of the solar system around the galactic center and through the cosmic-ray background. The anisotropy observed in Milagro's map, however, cannot be fitted by the predicted CG dipole. In addition, the CG anisotropy should be energy independent, which does not agree with the data either.

(ii) The heliosphere magnetic field could produce anisotropies (Nagashima et al. 1998; Schlickeiser et al. 2007) that can

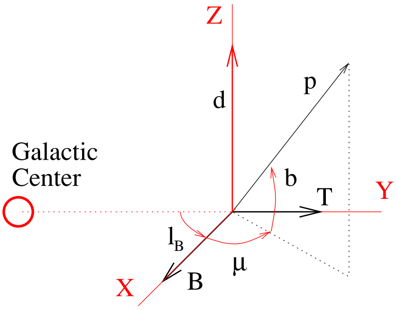

Figure 1. Angles b and μ, and orthogonal vectors $\vec{B}$, $\vec{T}$, and $\vec{d}$ for $l_B = 90°$.

also be ruled out. The Larmor radius r_g sets the size of the coherence cells, and for 10 TeV protons it is around 2×10^{-3} pc, significantly larger than the 5×10^{-4} pc (100 AU) of the heliosphere. Moreover, as pointed out in Abdo et al. (2009), the anisotropies persist at higher energies (i.e., for larger distance scales), supporting the hypothesis that if magnetic fields are involved they are extra-heliospheric.

Here we explore the effect of the local (regular and fluctuating) magnetic fields on the propagation of TeV cosmic rays reaching the Earth. Most analyses model cosmic-ray propagation with a diffusion equation (Ptuskin et al. 2006; Strong et al. 2007; Schlickeiser et al. 2007), assuming a certain spatial distribution of sources and a diffusion tensor often simplified to an isotropic scalar coefficient. This provides the flux over an extended region around the solar neighborhood. Here we intend a different approach. The diffusion equation derives from Boltzmann's equation, which contains *more* information. The solution of Boltzmann's equation in the vicinity of the Earth gives the statistical distribution function $f(\vec{r}, \vec{p}, t)$, a quantity related to the intensity or surface brightness used in astrophysics. f provides the number of cosmic rays per unit solid angle, time, and surface from any given direction, so it can be compared with Milagro's data pixel by pixel.

2. COSMIC-RAY DISTRIBUTION FUNCTION

We will treat TeV cosmic rays as a fluid that microscopically interacts only with the magnetic fields, and our objective is to obtain the distribution function $f(\vec{r}, \vec{p}, t)$ using Boltzmann's equation. We will take a basic *cell* of radius r_g and will assume that the non-turbulent component of the fluid is stationary and homogeneous. At these relatively small distance (and time) scales we also can neglect cosmic-ray sources, energy loss, or collisions with interstellar matter. In addition, we take the cosmic rays as protons (the dominant component in the flux) of $E = 6$ TeV (the average energy in Milagro's analysis). Finally, we will assume that the regular magnetic field $\vec{B}$ is on the galactic plane with a galactic longitude l_B, although we will show that Milagro's data favor a component orthogonal to this plane (as found in other observations, Han et al. 1999). In Figure 1, we have depicted $\vec{B}$ with $l_B = 90°$.

The frequency of the (b, μ) direction in the momentum of cosmic rays reaching the Earth is then proportional to[1]

$$f(\vec{u}) = f(b, \mu), \tag{6}$$

where $\vec{u} = \vec{p}/p$, b is the galactic latitude, and μ is the longitude relative to the direction of the magnetic field $\vec{B}$. Note that the galactic longitude of the direction defined by $\vec{u}$ is just $l = l_B + \mu$.

Boltzmann's equation expresses in differential form how particles move in the six-dimensional phase space (Battaner, 1996). In our case this is just

$$\vec{F} \cdot \nabla_u \; f(\vec{u}) = e \; (\vec{u} \times \vec{B}) \cdot \nabla_u \; f(\vec{u}) = 0 \; . \tag{7}$$

Now, we separate the regular and the turbulent components both in the distribution function and in the magnetic field:

$$\begin{aligned} f &\to f + \delta f, \\ \vec{B} &\to \vec{B} + \delta \vec{B}. \end{aligned} \tag{8}$$

The components $\delta\vec{B}$ and δf vary randomly from one cell to another and have a vanishing average value,

$$[\delta \vec{B}] = [\delta f] = 0. \tag{9}$$

However, there may be correlations between both fluctuating quantities. In particular, we will assume a non-zero value of

$$\begin{aligned} [e \; (\vec{u} \times \delta\vec{B}) \cdot \nabla_u \; \delta f] &= e \; \vec{u} \cdot [\delta \vec{B} \times \nabla_u \; \delta f] \\ &= e \; \vec{u} \cdot \vec{T}. \end{aligned} \tag{10}$$

Boltzmann's equation for the regular component is then

$$(\vec{u} \times \vec{B}) \cdot \nabla_u \; f + \vec{u} \cdot \vec{T} = 0. \tag{11}$$

This equation can also be written as

$$\vec{u} \cdot (\vec{B} \times \nabla_u \; f) + \vec{u} \cdot \vec{T} = 0. \tag{12}$$

As $\vec{u}$ is any direction, this implies $\vec{B} \times \nabla_u \; f = \vec{T}$, i.e., the vector $\vec{T}$ must be orthogonal to $\vec{B}$. Taking $\vec{T}$ in the galactic plane,

$$\vec{u} \cdot \vec{T} = T \; \cos b \; \sin \mu, \tag{13}$$

and expressing

$$\nabla_u \; f = \frac{\partial f}{\partial b} \; \vec{u}_b + \frac{1}{\cos b} \; \frac{\partial f}{\partial \mu} \; \vec{u}_\mu \tag{14}$$

with

$$\begin{aligned} \vec{u}_b &= -\sin b \; \cos \mu \; \vec{u}_\phi - \sin b \; \sin \mu \; \vec{u}_r + \cos b \; \vec{u}_z; \\ \vec{u}_\mu &= -\sin \mu \; \vec{u}_\phi + \cos \mu \; \vec{u}_r, \end{aligned} \tag{15}$$

Equation (11) becomes

$$-\sin \mu \; \frac{\partial f}{\partial b} + \tan b \; \cos \mu \; \frac{\partial f}{\partial \mu} + \frac{T}{B} \; \cos b \; \sin \mu = 0 \; . \tag{16}$$

This equation can be solved analytically:

$$f(b, \mu) = f_0 \left(1 + \frac{T}{f_0 B} \; \sin b \right) + \tilde{f}(\cos b \; \cos \mu) \; , \tag{17}$$

with f_0 being a constant that normalizes f to the number of particles per unit volume and the second term any arbitrary function of the variable $\cos b \; \cos \mu$. From the direction $\vec{u}$ we observe cosmic rays with $\vec{p} = -p \; \vec{u}$; it is straightforward to find the relation between the distribution function and the flux

---

[1] $(E/c)^2 f(\vec{u})$ gives the number of particles with momentum along $\vec{u}$ per unit energy, volume, and solid angle at $E \approx 6$ TeV.

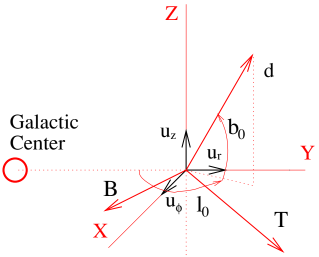

Figure 2. Trihedron defined by $\vec{B}$, $\vec{d}$, and $\vec{T}$, and the coordinate system. $\vec{B}$ is in the galactic plane, whereas $\vec{d}$ and $\vec{T}$ have latitudes b_0 and $90° - b_0$, respectively.

$F(b, \mu)$ of particles observed at Milagro per unit area, time, solid angle, and energy:

$$F(b, \mu) = \frac{E^2}{c^2}\, f(-b, \mu + \pi)\,. \tag{18}$$

This implies that

$$F(b, \mu) = F_0\,(1 - t\ \sin b) + \tilde{F}(\cos b\ \cos\mu)\,, \tag{19}$$

where $t = T/(f_0 B)$ and $F_0 = (E/c)^2 f_0$. Finally, we will expand $\tilde{F}$ to second order:

$$\tilde{F}(\cos b\ \cos\mu) \approx F_1 \cos b\ \cos\mu + F_2\,(\cos b\ \cos\mu)^2\ . \tag{20}$$

The solution in terms of the galactic longitude is obtained just by expressing $\mu = l - l_B$.

Several comments are here in order.

(i) If $F_1 = F_2 = 0$, then the solution is a dipole anisotropy, with the minimum/maximum in the north/south galactic poles. This dipole is then *modulated* by the constants $F_{1,2}$, that introduce an anisotropy proportional to $\cos b \cos\mu$ (i.e., the additional anisotropy coincides along the directions $\vec{u}$ with equal projection on $\vec{B}$).

(ii) The dipole anisotropy would vanish if there were no turbulence ($t = 0$): $\vec{B}$ implies an isotropy broken by the turbulence in the orthogonal plane. In contrast, the equation does not say anything about the direction along $\vec{B}$. For different boundary conditions one can find solutions with a forward–backward asymmetry (implying diffusion along $\vec{B}$) or symmetric solutions. In particular, F_1 creates an asymmetry between the ($b = 0$, $\mu = 0$) and ($b = 0$, $\mu = 180°$) directions, whereas the F_2 contribution is symmetric.

(iii) The dominant magnetic field $\vec{B}$, the turbulence $\vec{T}$, and the dipole $\vec{d}$ are always orthogonal to each other. For $\vec{B} \approx B\vec{u}_\phi$ the symmetry of the galactic disk could favor a radial turbulence, $\vec{T} \approx T\vec{u}_r$, like the one that we have assumed above (see Figure 1).[2] However, one can change the latitude b_0 of the dipole while keeping $\vec{B}$ on the galactic plane just by taking the turbulence $\vec{T}$ out of the plane. In particular, the dipole will point toward the arbitrary direction b_0 (see Figure 2) if

$$\vec{u}\cdot\vec{T} = T\,(\sin b_0\ \cos b\ \sin\mu - \cos b_0\ \sin b)\ . \tag{21}$$

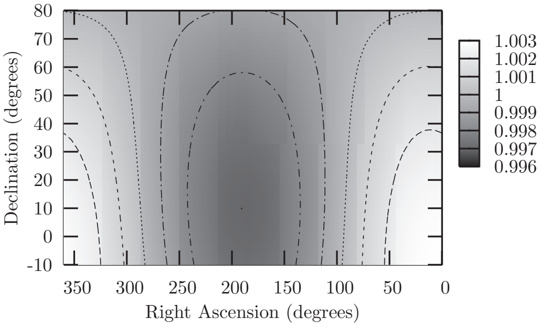

Figure 3. Fit of the Milagro anisotropy.

The dipole solution is in that case

$$F(b, \mu) = F_0\,[1 - t\,(\sin b_0\ \sin b + \cos b_0\ \cos b\ \sin\mu)] + F_1 \cos b\ \cos\mu + F_2\,(\cos b\ \cos\mu)^2\ . \tag{22}$$

The galactic latitude l_0 of the dipole is then fixed by the orientation of $\vec{B}$ in the galactic plane,

$$l_0 = l_B + 90°. \tag{23}$$

The direction of the dipole in the basis pictured in Figure 2 is

$$\vec{u}_d = \cos b_0\ \sin l_0\ \vec{u}_\phi - \cos b_0\ \cos l_0\ \vec{u}_r + \sin b_0\ \vec{u}_z. \tag{24}$$

3. MILAGRO DATA

Milagro data (Abdo et al. 2009) indicate a clear dipole anisotropy, with a deficit in the north galactic hemisphere that peaks at $\delta_0 \approx 10°$ and $AR_0 \approx 190°$ (i.e., $b_0 \approx 72°$ and $l_0 \approx 293°$). In Figure 3, we plot our fit of the data (restricted to a region in the sky), which is obtained for $t = 0.003$ with $F_1/F_0 = 0$, $F_2/F_0 = 0.0003$ and a magnetic field $\vec{B}$ along $l_B = 203°$. Our simple fit, an approximate dipole along the direction of $\nabla_u f$ (from b_0, l_0 to $-b_0$, $l_0 - \pi$) provides a good description of Milagro's anisotropy.

The fit implies that cosmic rays move near the Earth with a mean velocity

$$\vec{v}_0/c = -\frac{1}{N}\int d\Omega\ F(\vec{u})\,\vec{u} = -0.00059\,\vec{u}_\phi - 0.00028\,\vec{u}_r + 0.00157\,\vec{u}_z, \tag{25}$$

where $N = \int d\Omega\ F(\vec{u})$ and the basis is pictured in Figure 2. Equation (25) expresses the diffusion velocity of the fluid (the transport flux $\vec{J}$ is proportional to $N\vec{v}_0$), and we find that it goes exactly in the direction of the dipole (the term F_1 would change its direction but we have set it to zero).

It is important to note that the regular magnetic field $\vec{B}$ does *not* need to be on the galactic plane (our choice above), it can rotate around the dipole axis and still give the same dipole solution as far as the turbulence $\vec{T}$ is rotated as well. Doing that the only changes would appear in the boundary conditions (F_1 and F_2), but the pure dipole would provide the simplest solution in any case. The dipole seems to point toward

$$\vec{u}_d = -0.35\,\vec{u}_\phi - 0.16\,\vec{u}_r + 0.92\,\vec{u}_z. \tag{26}$$

---

[2] Buoyancy will mainly produce ascending turbulent cells; since Coriolis forces are negligible at these small timescales the compression of the (frozen-in) azimuthal field lines may result into a $\delta\vec{B}$ also azimuthal and a vertical $\nabla_u\ \delta f$, which imply a radial $\vec{T}$.

Therefore, we can check if this dipole observed at Milagro and the local regular magnetic field $\vec{B}$ (also an observational output) are perpendicular. We will consider the values of $\vec{u}_B$ given by Han (Han et al. 1999; Han 2009). It is found that $\vec{B}$ is basically azimuthal clockwise (a *pitch* angle of either 0° or 180° depending on the definition, which changes for different authors). However, the observations also indicate the presence of a non-null *tilt* angle of 6° (a vertical component of order 0.3 μG) taking the magnetic field out of the plane. We obtain an unitary vector

$$\vec{u}_B = 0.99\,\vec{u}_\phi + 0.00\,\vec{u}_r + 0.10\,\vec{u}_z\ , \tag{27}$$

which implies a remarkable

$$\vec{u}_d \cdot \vec{u}_B = -0.18. \tag{28}$$

We think that the approximate orthogonality of these two observational vectors (we obtain an angle of 100°) provides support to the model presented here.

Note that our framework could also accommodate other anisotropies in the flux, added to the dipole one, as far as they have the same value in all the points with equal projection ($\cos b \cos \mu$) on $\vec{B}$. To explain a *point-like* anisotropy like the one named as *region A* in Abdo et al. (2008), the anisotropy itself should be along the direction of the dominant magnetic field $\vec{B}$ (orthogonal to $\vec{d}$). *Region A*, however, is at ($b_A \approx$-30°, $l_A \approx 215°$), forming an angle of 58° with the dipole.

4. SUMMARY AND DISCUSSION

Although charged cosmic rays do not reveal their source, the study of their flux from different directions is of interest in astrophysics because it brings valuable information about the interstellar medium. In particular, the *per mille* deficit observed by Milagro could be caused by the local (at distances of order r_g) magnetic fields.

Using Boltzmann's equation we have shown that the interplay between the regular and the turbulent components in these magnetic fields always produces a dipole anisotropy in the cosmic-ray flux. We find that (i) the direction of this anisotropy is orthogonal to the regular $\vec{B}$ and (ii) its intensity is proportional to the fluctuations $\delta B/B$ at the wavenumber $k = 1/r_g$. These two simple results have already non-trivial consequences. In particular, (i) implies that a north–south galactic anisotropy would only be consistent with a dominant $\vec{B}$ laying in the galactic plane, whereas (ii) explains that the anisotropy is *larger* for more energetic cosmic rays: their gyroradius r_g is larger, the resonant wavenumber k smaller, so the expected value of $\delta B/B$ will be larger.

We have argued that Milagro's data can be interpreted as a dipole anisotropy pointing to a well-defined direction in the north galactic hemisphere, namely ($b_0 \approx 72°$, $l_0 \approx 293°$). Our model provides a remarkable fit of the data, so we conclude that it explains satisfactorily the large-scale anisotropy found by Milagro. The model implies that the dominant magnetic field near our position *must* be in the plane orthogonal to the dipole ($\vec{B}$, the turbulence correlation $\vec{T}$ and $\vec{d}$ define a trihedron). This plane forms an angle $\theta = 23°$ with the galactic disk.

The data obtained by Milagro (energy, direction, and nature of over 10^{11} primaries) show that the 10^{-3} deficit in the cosmic-ray flux from the north galactic hemisphere already seen in previous experiments (Aglietta et al. 1996; Amenomori et al. 2006) is actually very close to a dipole anisotropy. We think that the analysis of the flux after subtracting this dipole anisotropy could reveal further correlations.

We thank Brenda Dingus for useful discussions. The work of E.B. has been funded by MEC of Spain (ESP2004-06870-C02). The work of M.M. has been supported by MEC of Spain (FPA2006-05294) and by Junta de Andalucía (FQM-101 and FQM-437).

REFERENCES

Abdo, A. A., et al. 2008, Phys. Rev. Lett., 101, 221101
Abdo, A. A., et al. 2009, ApJ, 698, 2121
Achterberg, A., et al. (IceCube Collaboration) 2006, Astropart. Phys., 26, 155
Aglietta, M., et al. (EAS-TOP Collaboration) 1996, ApJ, 470, 501
Amenomori, M., et al. (Tibet AS-gamma Collaboration) 2006, Science, 314, 439
Battaner, E. 1996, Astrophysical Fluid Dynamics (New York: Cambridge Univ. Press)
Battaner, E. 2009, in Lecture Notes and Essays in Astrophysics III: Third Symposium of the Astrophysics Group of the Spanish Royal Physical Society (RSEF), ed. A. Ulla & M. Manteiga (A Coruna: Tórculo Press)
Beck, R. 2004, Ap&SS, 289, 293
Beck, R. 2005, in Cosmic Magnetic Fields, ed. R. Wielebinski & R. Beck (Heidelberg: Springer)
Casse, F., Lemoine, M., & Pelletier, G. 2002, Phys. Rev. D, 65, 023002
Compton, A. H., & Getting, I. A. 1935, Phys. Rev., 47, 817
Han, J. L., Manchester, R. N., & Qiao, G. J. 1999, MNRAS, 306, 371
Han, J. L. 2009, arXiv:0901.1165
Jansson, R., Farrar, G. R., Waelkens, A. H., & Ensslin, T. A. 2009, J. Cosmol. Astropart. Phys., JCAP07(2009)021
Nagashima, K., Fujimoto, K., & Jacklyn, R. M. 1998, J. Geophys. Res., 103, 17429
Page, L., et al. (*WMAP* Collaboration) 2007, ApJS, 170, 335
Ptuskin, V. S., Jones, F. C., Seo, E. S., & Sina, R. 2006, Adv. Space Res., 37, 1909
Schlickeiser, R., Dohle, U., Tautz, R. C., & Shalchi, A. 2007, ApJ, 661, 185
Strong, A. W., Moskalenko, I. V., & Ptuskin, V. S. 2007, Annu. Rev. Nucl. Part. Sci., 57, 285
Ruiz-Granados, B., Rubiño-Martín, J. A., & Battaner, E. 2009, A&A, submitted
Voelk, H. J., & Bernloehr, K. 2009, Exp. Ast., 25, 173
Weekes, T. C. 2008, arXiv:0811.1197
Wielebinski, R. 2005, in Cosmic Magnetic Fields, ed. R. Wielebinski & R. Beck (Heidelberg: Springer)